

Old Dominion University

ODU Digital Commons

Electrical & Computer Engineering Theses &
Dissertations

Electrical & Computer Engineering

Summer 8-2022

Recrystallization of Cu(In,Ga)Se₂ Semiconductor Thin Films Via Metal Halides Treatment

Deewakar Poudel

Old Dominion University, dpoud001@odu.edu

Follow this and additional works at: https://digitalcommons.odu.edu/ece_etds



Part of the [Electrical and Computer Engineering Commons](#)

Recommended Citation

Poudel, Deewakar. "Recrystallization of Cu(In,Ga)Se₂ Semiconductor Thin Films Via Metal Halides Treatment" (2022). Doctor of Philosophy (PhD), Dissertation, Electrical & Computer Engineering, Old Dominion University, DOI: 10.25777/bm73-9k36
https://digitalcommons.odu.edu/ece_etds/240

This Dissertation is brought to you for free and open access by the Electrical & Computer Engineering at ODU Digital Commons. It has been accepted for inclusion in Electrical & Computer Engineering Theses & Dissertations by an authorized administrator of ODU Digital Commons. For more information, please contact digitalcommons@odu.edu.

**RECRYSTALLIZATION OF Cu(In,Ga)Se₂ SEMICONDUCTOR THIN
FILMS VIA METAL HALIDES TREATMENT**

by

Deewakar Poudel
M.Sc. December 2015, Tribhuvan University, Nepal

A Dissertation Submitted to the Faculty of
Old Dominion University in Partial Fulfillment of the
Requirements for the Degree of

DOCTOR OF PHILOSOPHY

ELECTRICAL AND COMPUTER ENGINEERING

OLD DOMINION UNIVERSITY
August 2022

Approved by

Sylvain Marsillac (Director)

Gon Namkoong (Member)

Orlando Ayala (Member)

Linda Vahala (Member)

ABSTRACT

RECRYSTALLIZATION OF Cu(In,Ga)Se₂ SEMICONDUCTOR THIN FILMS VIA METAL HALIDES TREATMENT

Deewakar Poudel
Old Dominion University, 2022
Director: Dr. Sylvain Marsillac

The advancement of low-cost, highly efficient solar cell devices is a major technological challenge demanding suitable materials and fabrication processes. Polycrystalline Cu(In,Ga)Se₂ (CIGS) appear to be one of the most promising semiconductor in thin film photovoltaic technology due to its bandgap tunability, high absorption coefficient, and tendency to produce high efficiency solar cells. High-quality CIGS materials fabricated via a three-stage co-evaporation process can convert primary materials into devices with power conversion efficiency above 23%. Increasing the deposition rate and decreasing the deposition temperature, while maintaining high efficiency, is the major concern for the CIGS solar cells to compete with silicon-based technology and to allow their application in industrial domain. A post-deposition treatment of the as-deposited films by alkali halides and selenium improve the devices to some extent. To further accelerate the microstructure evolution, the recrystallization of CIGS thin films via metal halides vapor treatment as a fluxing agent was proposed, as one of the possibilities of producing high-quality CIGS thin films. It is of great interest to recrystallize CIGS, potentially decreasing the fabrication cost and improving the economic viability. In this thesis, different metal halides such as indium bromide, indium chloride, copper chloride and silver bromide were used, with and without supplemental selenium. These compounds promote grain growth, resulting in much larger grains and change the crystallographic structure at low temperature deposition. A significant variation in the sodium profile, and gallium depletion were observed in some halide treatments, whereas no changes in composition profile occurred in others. In terms of devices, indium bromide and indium chloride ex-situ treatment did not yield better devices due to lack of optimal composition profile, but showed drastic changes in morphology evolution, whereas copper chloride and silver bromide in-situ recrystallization seemed to be better in terms of device performance, yielding high efficiency devices particularly in case of silver bromide in-situ vapor treatment.

Copyright, 2022, by Deewakar Poudel, All Rights Reserved.

ACKNOWLEDGEMENTS

I would like to express my sincere gratitude and appreciation to my dissertation supervisor Dr. Sylvain Marsillac, whose expertise, understanding, and patience added considerably to my graduate experience. His never-ending support and invaluable guidance throughout my academic career have always inspired me to strive for excellence.

I am very thankful to the dissertation committee: Dr. Gon Namkoong, Dr. Orlando Ayala, and Dr. Linda Vahala for their time, invaluable suggestions, and comments.

I am fortunate to be a part of the Virginia Institute of Photovoltaic (VIPV) at Old Dominion University and grateful to all the present and former research group members for their support in this work. I especially would like to thank Benjamin Belfore for his support in both research and personally.

I would like to acknowledge the support and encouragement I received from Dr. Shankar Karki and Dr. Grace Rajan for their continuous support and advice, which helped me stay motivated during my Ph.D.

I would like to thank Dr. Oscar Gonzalez, chair of the Electrical and Computer Engineering department, and staff Romina Samson and Lori Barrett for their help and support.

I especially would like to thank our collaborators Dr. Angus Rockett at Colorado School of Mines, Dr. Nicolas Barreau, and Dr. Thomas Lepetit at the University of Nantes, France.

I highly appreciate the help from Elizabeth Palmiotti and Sina Soltanmohammad for SIMS and STEM measurements and Dr. Wei Cao at the Applied Research Center for training me on XRD, AFM, and SEM measurements.

Finally, I would like to acknowledge with gratitude my family and friends for their support and encouragement during these years, without which this dissertation would not have been possible.

TABLE OF CONTENTS

	Page
LIST OF TABLES	vii
LIST OF FIGURES	viii
Chapter	
1. INTRODUCTION	1
1.1 PHOTOVOLTAIC TECHNOLOGY	1
1.2 EFFICIENCY OF CIGS SOLAR CELLS	2
1.3 RECRYSTALLIZATION OF CIGS THIN FILMS	4
1.4 SCOPE OF THIS THESIS	6
2. THEORETICAL BACKGROUND	8
2.1 FUNDAMENTAL OF SOLAR CELLS	8
2.2 CURRENT VOLTAGE CHARACTERISTICS OF A SOLAR CELL	12
2.3 QUANTUM EFFICIENCY	16
2.4 CIGS SOLAR CELLS DEVICE STRUCTURE	18
3. EXPERIMENTAL DETAILS AND CHARACTERIZATION TECHNIQUES	26
3.1 SAMPLE PREPARATION	26
3.2 CHARACTERIZATION TECHNIQUES	28
4. EX-SITU RECRYSTALLIZATION OF CIGS THIN FILMS	32
4.1 EXPERIMENTAL DETAILS	33
4.2 RECRYSTALLIZATION BY INDIUM BROMIDE TREATMENT	34
4.3 RECRYSTALLIZATION BY INDIUM CHLORIDE TREATMENT	49
4.4 SUMMARY	67
5. IN-SITU RECRYSTALLIZATION OF CIGS THIN FILMS-I	69
5.1 EXPERIMENTAL DETAILS	70
5.2 RECRYSTALLIZATION BY COPPER CHLORIDE TREATMENT	71
5.3 SOLAR CELLS DEVICE RESULTS	84
5.4 SUMMARY	88

6. IN-SITU RECRYSTALLIZATION OF CIGS THIN FILMS-II	89
6.1 EXPERIMENTAL DETAILS	89
6.2 RECRYSTALLIZATION BY SILVER BROMIDE TREATMENT	91
6.3 SOLAR CELLS DEVICE RESULTS	105
6.4 SUMMARY	110
7. CONCLUSIONS	111
REFERENCES	113
APPENDIX	126
VITA	131

LIST OF TABLES

Table	Page
1. X-ray Diffraction data measurements and analysis of as-deposited and samples annealed by InBr ₃ at 400°C for 30 minutes.....	38
2. X-ray Fluorescence and Hall Effect measurements of as-deposited and samples annealed by InBr ₃ at 400°C for 30 minutes.....	39
3. X-ray Diffraction data measurements and analysis of as-deposited and samples annealed by InBr ₃ at 500°C for 30 minutes.....	42
4. X-ray Fluorescence and Hall Effect measurements of as-deposited and samples annealed by InBr ₃ at 500°C for 30 minutes	43
5. X-ray Diffraction and X-ray Fluorescence data measurements and analysis of as-deposited and InCl ₃ -annealed samples at 450°C for 60 minutes	53
6. X-ray Diffraction and X-ray Fluorescence data measurements and analysis of as-deposited and InCl ₃ -annealed samples at 500°C for 60 minutes	56
7. Substrate temperature for the different stages of the CIGS runs	71
8. X-ray Diffraction and X-ray Fluorescence results of the reference, 2 nd -stage LT and 2 nd -stage HT CIGS samples	75
9. X-ray Diffraction and X-ray Fluorescence results of the reference, 3 rd -stage LT and 3 rd -stage HT CIGS samples	81
10. Photovoltaic characteristics and Diode parameters of the representative cells shown in Figure 36	84
11. Photovoltaic characteristics and Diode parameters of the representative cells shown in Figure 37	86
12. X-ray Diffraction and X-ray Fluorescence results of the reference and low-rate AgBr recrystallized CIGS samples	95
13. X-ray Diffraction and X-ray Fluorescence results of the reference and high-rate AgBr recrystallized CIGS samples	102
14. Photovoltaic characteristics of the reference, low-rate AgBr, high-rate AgBr recrystallized and alkali-treated samples.....	108

LIST OF FIGURES

Figure	Page
1. Solar PV Global Capacity and Annual Additions, 2010-2020 according to Renewable 2021 Global Status Report presented by Renewable Energy Policy Network for 21 st Century (REN21)	2
2. Relationship between the bandgaps and corresponding lattice parameters of Ag- and Cu-based I-III-VI ₂ materials	4
3. Schematic of the energy band diagram as a function of distance (a), electric field as a function of distance (b), and charge density as a function of distance (c) in a p-n junction at thermal equilibrium	9
4. Equivalent circuit diagram of a solar cell with single-diode model	13
5. I-V curve and power output of a typical solar cell	15
6. Spectral irradiance for AM0, AM1.5 Global and AM1.5 Direct solar spectrum	16
7. Quantum efficiency with optical losses in CIGS solar cell	17
8. Schematic diagram of typical CIGS solar cell device (top) and corresponding band diagram (bottom)	19
9. Crystal structure of zincblende (left) and chalcopyrite (right)	22
10. A pseudo-binary Cu ₂ Se-In ₂ Se ₃ equilibrium phase diagram	24
11. Scanning Electron Microscopy micrographs (surface and cross section) of CIGS films: as-deposited (left) and recrystallized (right) in InBr ₃ at 400°C for 30 minutes	35
12. X-ray Diffraction plots of three key CIGS peaks (112), (204) and (312) for as-deposited (black) and InBr ₃ -annealed (red) CIGS films at 400°C for 30 minutes	38
13. Scanning Electron Microscopy micrographs of CIGS films: as-deposited (top), recrystallized in Se (center) and recrystallized in InBr ₃ (bottom) at 500°C for 30 minutes .	40
14. Scanning Electron Microscopy micrographs of CIGS films comparing recrystallization by InBr ₃ at 400°C (left) and 500°C (right) for 30 minutes	41
15. X-ray Diffraction plots of three key CIGS peaks (112), (204) and (312) for as-deposited, Se-annealed and InBr ₃ -annealed CIGS films at 500°C for 30 minutes	44

16. Secondary Ions Mass Spectrometry depth profile (positive ions) for the as-deposited, Se-annealed and InBr ₃ -annealed CIGS films at 500°C for 30 minutes. Cu, In and Se ions (top), Ga and O ions (center), alkali ions (bottom)	47
17. Secondary Ions Mass Spectrometry depth profile (negative ions) for the as-deposited, Se-annealed and InBr ₃ -annealed CIGS films at 500°C	49
18. Scanning Electron Microscopy micrographs (surface and cross-section) of CIGS films: as-deposited (left) and recrystallized in InCl ₃ (right) at 450°C for 60 minutes	50
19. X-ray Diffraction plots of three key CIGS peaks (112), (204) and (312) for as-deposited and InCl ₃ -annealed CIGS films at 450°C for 60 minutes	52
20. Scanning Electron Microscopy micrographs (surface and cross-section) of CIGS films: as-deposited (left) and recrystallized in InCl ₃ (right) at 500°C for 60 minutes	54
21. X-ray Diffraction plots of three key CIGS peaks (112), (204) and (312) for as-deposited and InCl ₃ -annealed CIGS films at 500°C for 60 minutes	56
22. Grazing Incidence X-ray Diffraction plots of three key CIGS peaks (112), (220) and (312) at 0.5°, 1°, 2° and 4° of incidence for CIGS films recrystallized at 500°C for 60 minutes	58
23. Secondary Ions Mass Spectrometry depth profile (positive ions) of the main elements for as-deposited and InCl ₃ -annealed CIGS films at 500°C for 60 minutes	60
24. Spatial Resolution of secondary ion mass spectroscopy for CIGS films recrystallized in InCl ₃ at 500°C for 60 minutes for Indium (left), Gallium (center) and Indium and Gallium (right) superimposed	61
25. Scanning Electron Microscopy micrographs (surface and cross-section) of CGS films: as-deposited (left), recrystallized in InCl ₃ (center) and recrystallized in InCl ₃ +Se at 500°C for 60 minutes	62
26. Scanning Electron Microscopy micrographs (surface and cross-section) of CIGS films: as-deposited (left), recrystallized in InCl ₃ (center) and recrystallized in InCl ₃ +Se at 500°C for 60 minutes	63
27. Scanning Electron Microscopy micrographs (surface and cross-section) of CIS films: as-deposited (left), recrystallized in InCl ₃ (center) and recrystallized in InCl ₃ +Se at 500°C for 60 minutes	64

28. Scanning Electron Microscopy micrographs (surface and cross-section) of CIS films: as-deposited (left), recrystallized for 30 minutes (center) and 60 minutes (right) at 450°C by InCl ₃ vapor treatment for Cu-poor (top two row) and Cu-rich (bottom two row) films	65
29. Scanning Electron Microscopy micrographs (surface and cross-section) of CIS films: as-deposited (left), recrystallized for 30 minutes (center) and 60 minutes (right) at 500°C by InCl ₃ vapor treatment for Cu-poor (top two row) and Cu-rich (bottom two row) films	67
30. Scanning Electron Microscopy micrographs (surface and cross-section) of CIGS films: reference (top), 2 nd -stage LT (center) and 2 nd -stage HT (bottom) recrystallized in CuCl ₂ environment	73
31. X-ray Diffraction plots of three key CIGS peaks (112), (204) and (312) for the reference (black), 2 nd -stage LT (blue) and 2 nd -stage HT (red) CIGS films recrystallized in CuCl ₂ environment	75
32. Secondary Ions Mass Spectroscopy depth profile (positive ions) of the main elements for the reference (top), 2 nd -stage LT (center) and 2 nd -stage HT (bottom) CuCl ₂ -treated CIGS films	77
33. Scanning Electron Microscopy micrographs (surface and cross-section) of CIGS films: reference (top), 3 rd -stage LT (center) and 3 rd -stage HT (bottom) recrystallized in CuCl ₂ environment	79
34. X-ray Diffraction plots of three key CIGS peaks (112), (204) and (312) for the reference (black), 3 rd -stage LT (blue) and 3 rd -stage HT (red) CIGS films recrystallized in CuCl ₂ environment	81
35. Secondary Ions Mass Spectroscopy depth profile (positive ions) of the main elements for the reference (top), 3 rd -stage LT (center) and 3 rd -stage HT (bottom) CuCl ₂ -treated CIGS films	83
36. Representative J-V (top) and QE (bottom) curves for reference (black), 2 nd -stage LT (blue) and 2 nd -stage HT (red) devices	85
37. Representative J-V (top) and QE (bottom) curves for reference (black), 3 rd -stage LT (blue) and 3 rd -stage HT (red) devices	87

38. Scanning Electron Microscopy micrographs (cross-section) of CIGS films: reference (left) and low-rate AgBr-treated (right) samples	92
39. Secondary Ions Mass Spectroscopy depth profiles (positive ions) of the main elements for the reference (solid) and low-rate AgBr-treated (dash) CIGS samples	93
40. X-ray Diffraction plots of three key CIGS peaks (112), (204) and (312) for the reference (black) and low-rate AgBr (red) recrystallized CIGS samples	95
41. Scanning Electron Microscopy micrographs (cross-section) of CIGS films: reference (left) and high-rate AgBr-treated (right) samples	96
42. Transmission Electron Microscopy (TEM) (cross-section) of high-rate AgBr-treated CIGS sample	97
43. Elemental distribution of high-rate AgBr recrystallized CIGS sample measured by EDS in STEM	98
44. Secondary Ions Mass Spectroscopy depth profiles (positive ions) of the main elements for the reference (solid) and high-rate AgBr-treated (dash) CIGS samples	100
45. X-ray Diffraction plots of three key CIGS peaks (112), (204) and (312) for the reference (black) and high-rate AgBr-treated (red) recrystallized CIGS samples	102
46. Grazing Incidence X-ray Diffraction of three key CIGS peaks (112), (204) and (312) at 1° and 3° for the low-rate and high-rate AgBr-treated samples	104
47. Representative J-V (top) and QE (bottom) curves for reference (black) and low-rate AgBr-treated (red) devices	106
48. Representative J-V (top) and QE (bottom) curves for reference (black) and high-rate AgBr-treated (red) devices	107
49. Representative J-V (top) and QE (bottom) curves for three CIGS devices with high-rate AgBr-treated and no post-deposition treatment (red), CsF-Se treatment (orange) and KF-Se treatment (purple)	109

CHAPTER 1

INTRODUCTION

1.1 PHOTOVOLTAIC TECHNOLOGY

Photovoltaic (PV) energy is one of the vast renewable sources of thermal and electrical energy and is eco-friendly, convenient, effective, affordable, and applicable to reach the current global energy demand [1]. PV technology, as an alternative source of green energy, is becoming one of the most promising technologies in the field of renewable sources of energy in terms of low operational cost, good availability, ease of installation, and long term sustainability to alleviate the emission of greenhouse gases [2, 3]. The solar PV market increased extensively as an emerging market, according to Renewable 2021 Global Status Report presented by Renewable Energy Policy Network for 21st Century (REN21); they claim that solar PV installation increased by 139 GW for the first time in 2020, with a year-end total of 760 GW (see Figure 1) [4]. The primary function of solar cells is to receive solar radiation in the form of light and convert it directly into electricity [5]. With various methods of fabrication, PV technology is broadly classified into three main generations. The first generation involves crystalline silicon (c-Si) in basic, mono (c-Si), or multi-crystalline (mc-Si) forms. The second generation operates the thin film technologies with three main categories: the first one is Cadmium Telluride (CdTe), the second consists of amorphous silicon (a-Si), and microcrystalline silicon (μ c-Si), and the third is Copper Indium Gallium Diselenide (Cu(In,Ga)Se₂ or CIGS) and its derivatives. The third generation of PV technology employs perovskites and organic solar cells (OSC), including organic molecules and polymers [6, 7]. Many raw materials, nontoxicity, and the potential to meet high efficiency make crystalline silicon technology one of the most influential commercial integration, with 90% of the global industrial market. However, direct bandgap thin films PV technology are also commercialized, and exciting developments continue to be reported. Besides the absorption coefficient of thin film materials being higher than that of c-Si, thin films also have potential high energy conversion efficiency, low production costs, and minimum material use [8-11].

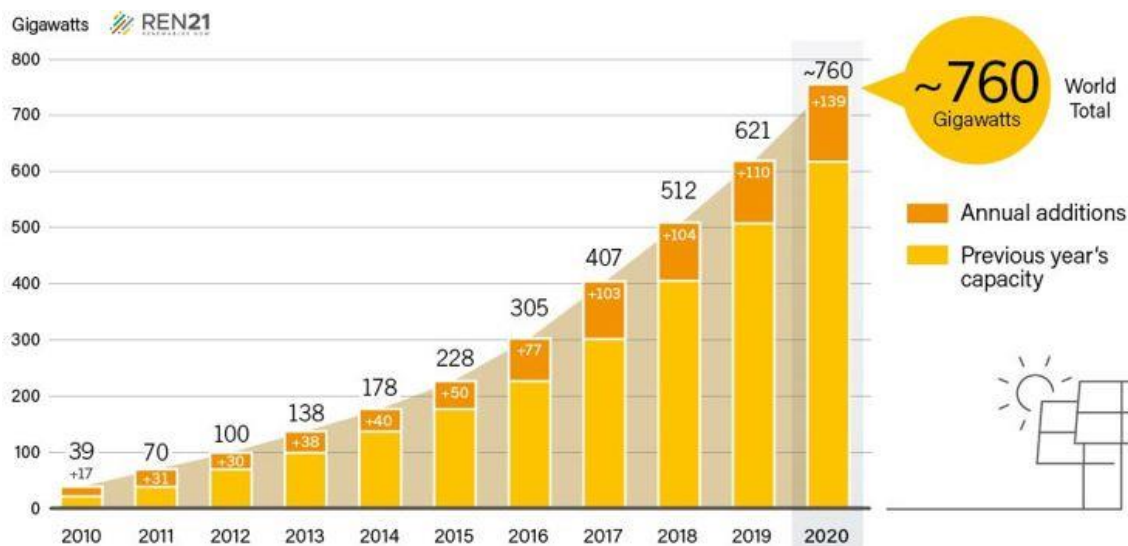


Figure 1. Solar PV Global Capacity and Annual Additions, 2010-2020, according to Renewable 2021 Global Status Report presented by Renewable Energy Policy Network for 21st Century (REN21) [4].

1.2 EFFICIENCY OF CIGS SOLAR CELLS

The I-III-VI₂ group (I = Cu, Ag; III = In, Ga, Al; VI = S, Se) compounds represent an essential class of semiconducting family in various technological applications due to their structural, electrical, and optical properties [12]. Copper-based (Cu-III-VI₂) are considered key in PV markets due to their high absorption coefficient, suitable bandgap, and simplicity of production [13]. Furthermore, potential application in second-order nonlinear optics, thermoelectric, and photocatalytic materials, and suitable absorber materials in thin film solar cells are some other advantages of these chalcopyrite semiconductors [14].

The direct bandgap of I-III-VI₂ chalcopyrite compounds vary from 0.96 eV (CuInTe₂) to 3.49 eV (CuAlS₂) with lattice constant in the range of 5.3 Å – 6.4 Å [15]. Despite many options for bandgap modification, the highest CIGSSe₂ solar cell efficiency has a small bandgap of 1.08 eV [16]. However, the performance of CIGS does not only vary with bandgap but also significantly

depends on the lifetime of the carriers and capacity of active dopant [17]. There is also significant attention for these I-III-VI₂ materials as potential candidates for the top cell of tandem solar cells with CIGS. The absorber material CuGaSe₂ (CGS) is notably a good candidate for tandem solar cells in combination with a CuInSe₂ (CIS) bottom cell [18]. However, the defects and inability to create n-type doping contribute to interface recombination limiting the CGS efficiency at 12% and is the major obstacle for CIGS-related tandem devices [19].

CIGS is a highly effective solar cell technology with record power conversion efficiency above 23% [20]. The excellence of the CIGS absorber layer and the interfacial properties in the multilayer structure of the CIGS solar cell play a significant role in the operation of the solar cells [21, 22]. The appropriate supplement of Ga across the CIGS film thickness is essential to reach high efficiency. Depending on the Ga concentration, the bandgap of CIGS can be modified from 1.04 eV (CIS) to 1.68 eV (CGS). The flexible bandgap of CIGS makes it an appealing contender for tandem devices [23-26]. The ideal bandgap of a single-junction CIGS device for maximum efficiency under the AM 1.5 spectrum is 1.4 eV [27]. However, high Ga content causes fill factor (FF) degradation, and open-circuit voltage does not increase proportionally to increase in bandgap. The performance loss in wide bandgap absorbers is most likely due to recombination losses, increase in defect states, and increase in band offset at the interface [28, 29]. Like bandgap engineering, including alkali species in the CIGS absorber layer is vital for high-performing CIGS solar cells [30]. The diffusion of Na from the typical soda-lime glass (SLG) substrate was found to boost the device performance of the CIGS solar cells. Na was found to impact the structural, optical, and electronic properties of CIGS films [31-33]. Elemental depth profiling has shown higher concentrations of Na in the front and the back interfacial regions of the CIGS films [34, 35], and compositional investigation shows that Na primarily resides at grain boundaries [36, 37]. Na mainly increases the p-type conductivity of the CIGS film and leads to increased open-circuit voltage and fill factor. It is also claimed that Na occupies the Cu vacancies (V_{Cu}), responsible for p-type conductivity, at the grain boundaries preventing the formation of compensating In_{Cu} defects [38, 39], which is validated by the existence of Na primarily at grain boundaries. Figure 2 shows the relationship between the bandgap and the lattice parameters for major I-III-VI₂ compounds, including the effect of main elements like S, Ga, Ag, and Al on widening the bandgap of these materials.

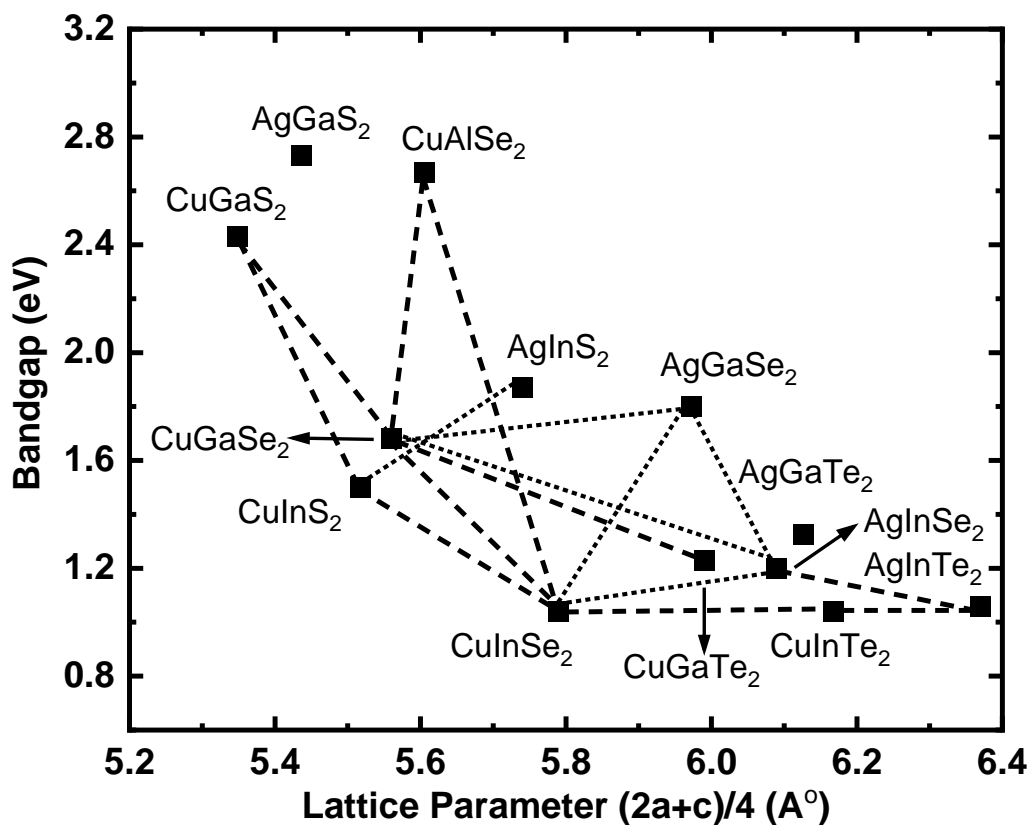


Figure 2. Relationship between the bandgaps and corresponding lattice parameters of Ag- and Cu-based I-III-VI₂ materials [40].

1.3 RECRYSTALLIZATION OF CIGS THIN FILMS

CIGS is a promising absorber layer for high efficiency, low-cost thin film photovoltaics, with a remarkable increase in efficiency in recent years due to groundbreaking alkali post-deposition treatments. It has accomplished high efficiency, easily exceeding polycrystalline silicon [2]. The development of high-rate and low-cost deposition techniques in combination with high efficiency devices is one of the important needs for contemporary photovoltaics (PV). However, most efficient CIGS cells are made using an expensive and relatively slow three-stage co-evaporation

process, typically at a high substrate temperature of 550°C [41, 42]. Flexibility in photovoltaic processes, and device performances, can be significantly improved by post-growth recrystallization [43]. Flexible processes can allow the absorber material to have much lower initial quality and thus be deposited at higher rates and lower temperatures [44]. Post-deposition treatment and recrystallization could produce large crystals of sufficient quality. The high deposition rate and cost-effective method are required to compete with CdTe and silicon PV. This could be attained by developing a method to recrystallize CIGS films deposited by co-evaporation at high-rates and low temperatures. For instance, the recrystallization of CdTe includes the high-rate deposition of the CdTe layer reinforced by annealed in CdCl₂ vapor. The CdCl₂ + O₂ process recrystallizes both the CdTe and the CdS [45]. Therefore, it would be of great interest to recrystallize semiconductors like CdTe, possibly decreasing their production cost and enhancing economic viability. The addition of O₂ to the CdS growth processes on CIGS can affect elemental redistribution. Post-growth annealing of CIGS in the presence of alkali-containing species has also been shown to improve device performance under some conditions [43].

CIGS and CIS films have been recrystallized in previous years. For example, CIGS thin film was fabricated by initially depositing Cu, In, and Ga and then annealing with hydrogen sulfide or hydrogen selenide gases [2, 46]. With deposition temperatures ranging from 350°C to 400°C, the annealing treatments in Se environments or inert controlled atmospheres improved crystallinity and decreased defect concentration in the films [47, 48]. However, the presence of alkali is essential to device performance for these recrystallization processes. The highest efficiency devices were reported after a post-deposition treatment of alkali on a CIGS layer. The devices with the highest efficiencies are typically deposited by co-evaporation on molybdenum-coated soda-lime glass substrates at 550°C [49]. CIGS thin films deposited at low temperature (350°C) and high-rate (10 μm/hr) by single-stage process were recrystallized using various alkali fluoride (NaF, KF, RbF, and CsF). All the annealing showed an increase in device performance with NaF proved to be the best for both recrystallization and electrical properties [50]. The microstructure of the deposited thin films was modified during recrystallization, and it was noticed that grain boundary motion plays a crucial role during recrystallization. Also, Cu-poor CIGS films that were close to the stoichiometric yielded large grain sizes. However, grain growth, and grain boundary motion, are insufficient for better devices as structural defects also contribute an important part [51].

Though multiple attempts have been made for CIGS recrystallization, none were enough to reach a definite conclusion.

1.4 SCOPE OF THIS THESIS

This thesis focuses on the fabrication, post-deposition treatment, and after that recrystallization of CIGS thin films, and multiscale application of optoelectronic, chemical, and physical characterization to understand their properties. The objectives are to understand metal halide-based recrystallization of CIGS quantitatively to permit predictive engineering in process development. The method thoroughly examines the change in crystal structure and device performance associated with post-growth annealing of CIGS in metal-halide environments, promotes vapor phase transport to understand the mechanisms, determine the effect on optoelectronic properties, and quantitatively relate these to changes in device performance through modeling. This work will guide CIGS process development and process options for high-rate, low-cost CIGS growth, analogous to techniques used in CdTe processing. It will explore novel post-growth processing options that will potentially improve the materials analogous or superior to those obtained by the three-stage process. The work is based on the ability of halides to transport all the CIGS components in the vapor phase combined with the ability of metals-halides to enhance device performance. The results of this work will be to demonstrate the effects of recrystallization of CIGS and vapor phase transport of the component elements using halide-containing species, and establish the changes in optoelectronic and structural properties of the CIGS during anneal. It will evaluate higher solar cell efficiency with a 100°C decrease in CIGS deposition temperature and 10 times increase in deposition rate relative to standard processes.

This thesis is designed as follows: In chapter 2, a synopsis of the introductory device physics of a p-n junction diode to describe the working principle of photovoltaic devices is presented. The device structure of the CIGS solar cell is discussed. Chapter 3 consists of experimental details of CIGS thin films and solar cell fabrication procedures, followed by a brief discussion of various characterization techniques used in this study. Chapter 4 describes the ex-situ recrystallization of CIGS thin film by InBr_3 and InCl_3 post-deposition treatment. The different characterization results were discussed on metal halides-treated and as-deposited samples at different temperatures. This

chapter is based on the publications in references [52-56]. In chapter 5, the in-situ recrystallization of CIGS thin film by CuCl_2 vapor treatment was investigated. The substrate temperature of the second and third-stages of the CIGS deposition process was changed, and the effect on compositional, structural, and electrical properties has been analyzed. This chapter is based on the publications in reference [57, 58]. Chapter 6 is related to the in-situ recrystallization of CIGS thin film by AgBr vapor treatment. The recrystallization was performed at a low-rate and high-rate AgBr, and their effect on the crystallographic, depth profiles, and overall photovoltaic performance was studied. This chapter is based on the publication in reference [59]. Finally, chapter 7 summarized the results of the comprehensive study.

CHAPTER 2

THEORETICAL BACKGROUND

This chapter includes some basic principles of the photovoltaic devices based on the p-n junction needed for the physical interpretation of chalcopyrite solar cells [41, 60-64]. Additionally, the basic design of the I-III-VI₂ solar cells structure is reviewed, notably in terms of the function of each multilayer and materials used for the fabrication.

2.1 FUNDAMENTAL OF SOLAR CELLS

The solar cell is simply a semiconductor diode that is structured efficiently to absorb and convert light into electrical energy. The conversion process involves (i) the generation of electron-hole pairs in a semiconductor by absorbing incident light with sufficient photon energy, (ii) the separation of these photo-generated charge carriers to build the photovoltage, and (iii) the collection of these carriers by appropriate electrodes. The incident light energy must exceed the difference between the conduction band minimum and the valence band maximum referred to as bandgap (E_g). This operation can be completed by a p-n junction or diode fabricated by regions of the semiconductor with opposite active doping or by joining a p-type and n-type semiconductor.

When the p-type and n-type semiconductors are brought together, the bending of the energy bands creates a large carrier concentration gradient leading to carrier diffusion. The majority carrier from the n-type semiconductor (electrons) diffuses to the p-side, leaving some of the positive donor ions (N_D) near the junction uncompensated, and the majority carrier (holes) from the p-type semiconductor diffuses to the n-side leaving negative acceptors ions (N_A) uncompensated. As a result, a negative space charge forms near the p-side of the junction, and a positive space charge forms near the n-side of the junction. A schematic of the energy band, charge distribution, and electric field of a p-n junction at equilibrium is shown in Figure 3. The diffusion and drift currents for each carrier type are balanced at thermal equilibrium, so there is no net current

flow. The transition region between n-type and p-type semiconductors is called the space charge region or depletion region [60, 61].

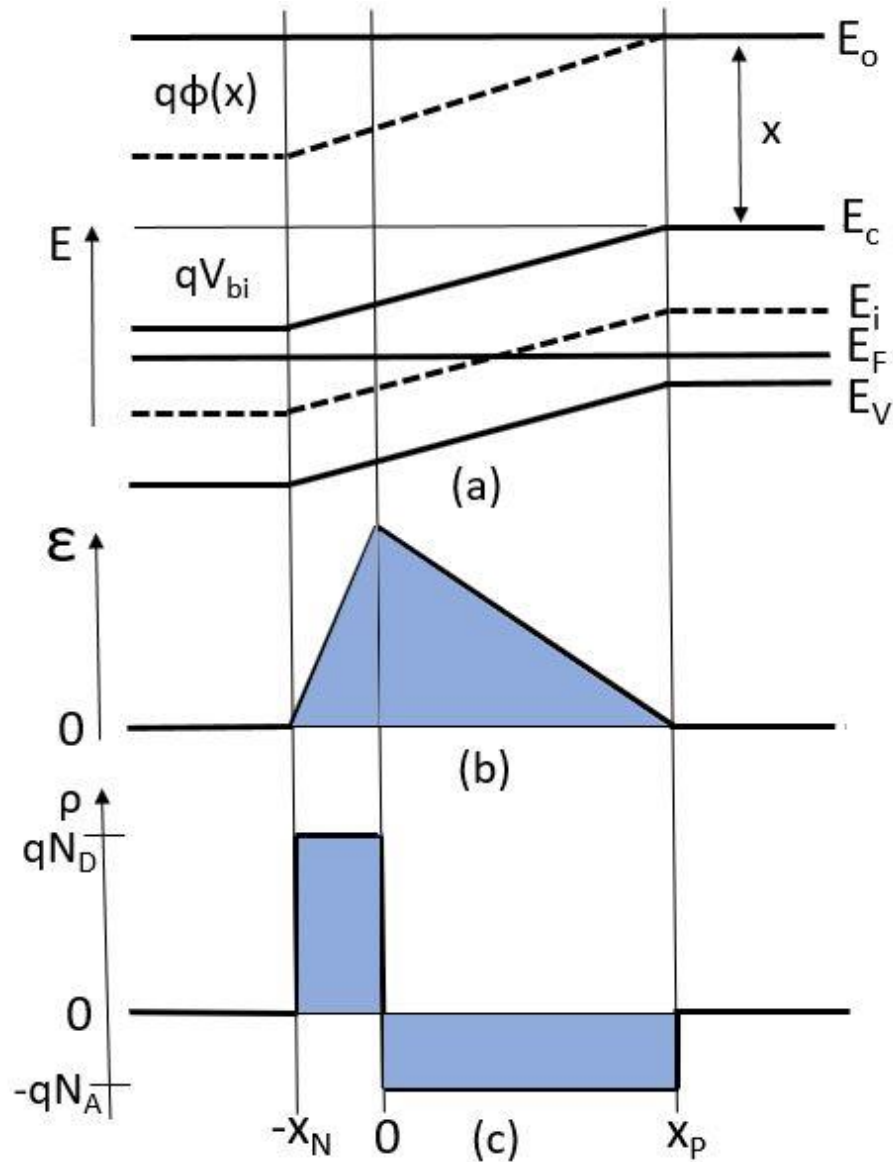


Figure 3: Schematic of the energy band diagram as a function of distance (a), electric field as a function of distance (b), and charge density as a function of distance (c) in a p-n junction at thermal equilibrium [62].

The approximate mathematical solution for the space charge region for an abrupt p-n junction is based on the depletion approximation. The space charge region is assumed to be fully depleted of mobile charges up to the edge of the depletion region. In this case, the n-type side is assumed to be more heavily doped than the p-type side. The space charge distribution and electrostatic potential Ψ are given by Poisson's equation:

$$\frac{d^2\Psi}{dx^2} = -\frac{\rho}{\epsilon_s} = -\frac{q}{\epsilon_s} (N_D - N_A + p - n)$$

where ρ is the space charge density, ϵ_s is the permittivity of the semiconductor material, q is the electronic charge, p is the equilibrium hole concentration, n is the equilibrium electron concentration, and $N_{A,D}$ is the acceptor and donor concentration in p-type and n-type semiconductor, respectively. Since, in the depletion region, free carriers are completely depleted, the solution of Poisson's equation can be simplified and split into two regions:

$$\frac{d^2\Psi}{dx^2} = \frac{qN_A}{\epsilon_s} \text{ for } -x_p < x < 0$$

$$\frac{d^2\Psi}{dx^2} = -\frac{qN_D}{\epsilon_s} \text{ for } 0 < x < x_n$$

Charge neutrality is assumed outside the depletion region, therefore $\Delta\Psi = 0$, for $x < -x_n$ and $x > x_p$. This is generally described as the depletion approximation. The region on either side of the depletion region is the quasi-neutral region. The integration of these two equations gives the following electric field across the depletion region:

$$E(x) = -\frac{qN_A(x + x_p)}{\epsilon_s} \text{ for } -x_p < x < 0$$

$$E(x) = \frac{qN_D(x_n - x)}{\epsilon_s} \text{ for } 0 < x < x_n$$

Again, integrating the above equation over the depletion region gives the total potential variation or built-in potential:

$$V_{bi} = \frac{qN_A x_p^2}{2\epsilon_s} + \frac{qN_D x_n^2}{2\epsilon_s}$$

The total negative space charge per unit area on the p-side must be equal to the total positive space charge per unit area on the n-side, therefore:

$$N_A x_p = N_D x_n$$

The electrostatic potential difference across the junction is the built-in potential, V_{bi} , and can be obtained by integrating the electric field. From the above equations, the depletion layer width as a function of the built-in potential is:

$$W = \sqrt{\frac{2\epsilon_s}{q} \left(\frac{N_A + N_D}{N_A N_D} \right) V_{bi}}$$

The total current must be zero in the absence of an applied voltage, as diffusion and drift current cancel each other for both types of carriers. When an external voltage is applied across the junction, the device exhibits typical diode current-voltage characteristics. When applying forward bias, making the p-region positive with respect to the n-region, the potential barrier decreased, thereby increasing the diffusion current of both holes and electrons. Therefore, minority carriers transfer occurs such that electrons are introduced into the p-side, whereas holes are introduced into the n-side. Reversing the polarity of applied voltage raises the diffusion barrier and permits only minority carriers near the transition regions to participate in conduction. This reduces the diffusion current and results in a small reverse saturation current. The minority carrier current densities on the p-side and the n- side are:

$$J_P(x_n) = \frac{qD_P P_{no}}{L_P} \left(e^{\left(\frac{qV}{kT}\right)} - 1 \right)$$

$$J_n(-x_p) = \frac{qD_n n_{p0}}{L_p} \left(e^{\left(\frac{qV}{kT}\right)} - 1 \right)$$

where $D_{n,p}$ is the diffusion coefficient for electrons and holes, $L_{n,p}$ is the diffusion length of electrons and holes, n_{p0} is the equilibrium electron density on the p-side, and p_{n0} is the equilibrium hole density on the n-side. The J_p and J_n must be constant across the depletion region, and the total current can be express as the sum of the electron and hole currents at the depletion edges.

$$J = J_p(x_n) + J_n(-x_p)$$

$$J = J_s \left(e^{\left(\frac{qV}{kT}\right)} - 1 \right),$$

$$J_s = \frac{qD_p p_{n0}}{L_p} + \frac{qD_n n_{p0}}{L_n}$$

where J_s is the reverse saturation current density due to carrier diffusion in the quasi-neutral region. These equations are referred to as the ideal diode equations [60, 63].

2.2 CURRENT VOLTAGE CHARACTERISTICS OF A SOLAR CELL

The current density-voltage (J-V) characteristics of illuminated solar cells can be represented by the fundamental diode equation. In a single-diode model, the current flowing through the device is the sum of the diode current density, J_{diode} , the current density flowing through the shunt, J_{shunt} , and the photogenerated current density, J_L , describe the J-V behavior of a solar cell. Therefore, we have the following sets of equations:

$$J_{diode}(V) = J_o \left[\exp \left\{ \frac{q(V - JR_S)}{AkT} \right\} - 1 \right], \quad J_{shunt}(V) = \frac{V - JR_S}{R_{Sh}}$$

$$J(V) = J_{diode}(V) + J_{shunt}(V) - J_L$$

$$J(V) = J_o \left[\exp \left\{ \frac{q(V - JR_S)}{AkT} \right\} - 1 \right] + \frac{V - JR_S}{R_{Sh}} - J_L$$

where J is the current density, V is the applied voltage, J_o is the reverse saturation current density, q is the electron charge, R_s and R_{sh} are the series and shunt resistances, A is the diode ideality factor, kT is the Boltzmann constant multiplied with temperature and J_L is the light-generated current. The equivalent circuit diagram of a solar cell for the single-diode model is depicted in Figure 4.

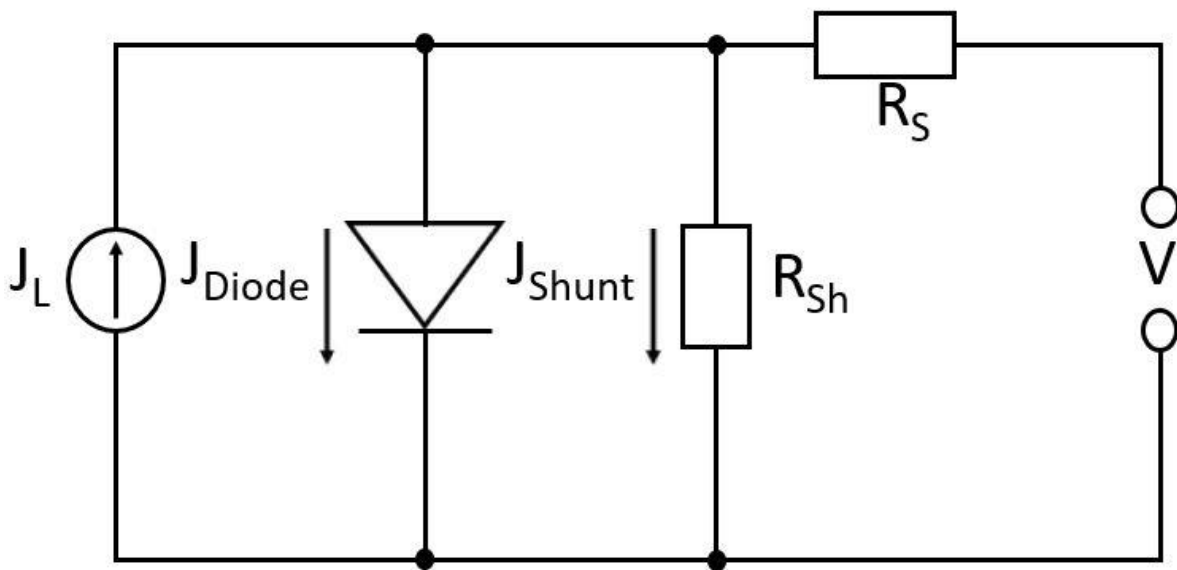


Figure 4. Equivalent circuit diagram of a solar cell with single-diode model.

The typical J-V curve of a solar cell is shown in Figure 5. The two points of the curve, the short-circuit current density (J_{sc}) and the open-circuit voltage (V_{oc}) are important parameters for analysis under illumination. The short-circuit current density is the current through the solar cell

under illumination when $V = 0$. In the absence of series resistance ($R_S = 0$) and shunt resistance ($1/R_{Sh} = 0$), the J_{SC} is equivalent to the light generated current J_L , and the diode equation simplifies as:

$$J(V) = J_0 \left(e^{\frac{qV}{kT}} - 1 \right) - J_{ph}$$

The open-circuit voltage is the voltage at which no current flows across the solar cell under illumination. In an ideal diode case, V_{OC} can be expressed as:

$$V_{OC} = \frac{kT}{q} \ln \left(\frac{J_L}{J_0} + 1 \right)$$

This is the maximum voltage that the cell can deliver. The reverse saturation current density J_0 depends on the recombination of the cell, V_{OC} is the measure of the amount of recombination in the cell. The fill factor (FF) of the solar cell is the measure of the squareness of the J-V curve and is defined as:

$$FF = \frac{V_{mp} \times J_{mp}}{V_{OC} \times J_{SC}}$$

The fill factor describes how closely the area defined by the J-V curve resembles a rectangle. Low FF is due to large R_S , small R_{Sh} , and voltage-dependent carrier collection. There is a small impact of the diode ideality factor, A , on FF. The diode ideality factor, A , changes based on device properties such as the dominant current transport mechanism and scaling factor for the voltage. An increase in diode quality factor leads to a higher V_{OC} . The power conversion efficiency of a solar cell is the ratio of the output electric power divided by the input solar radiation power under standard test conditions.

$$\eta = \frac{V_{mp} \times J_{mp}}{P_{in}} = \frac{FF \times V_{OC} \times J_{SC}}{P_{in}}$$

where P_{in} is the power density of the incident radiation, equal to 100 mW/cm^2 under standard AM1.5 conditions. The equation compares the impact of J_{sc} , V_{oc} , and FF on device efficiency [62, 63].

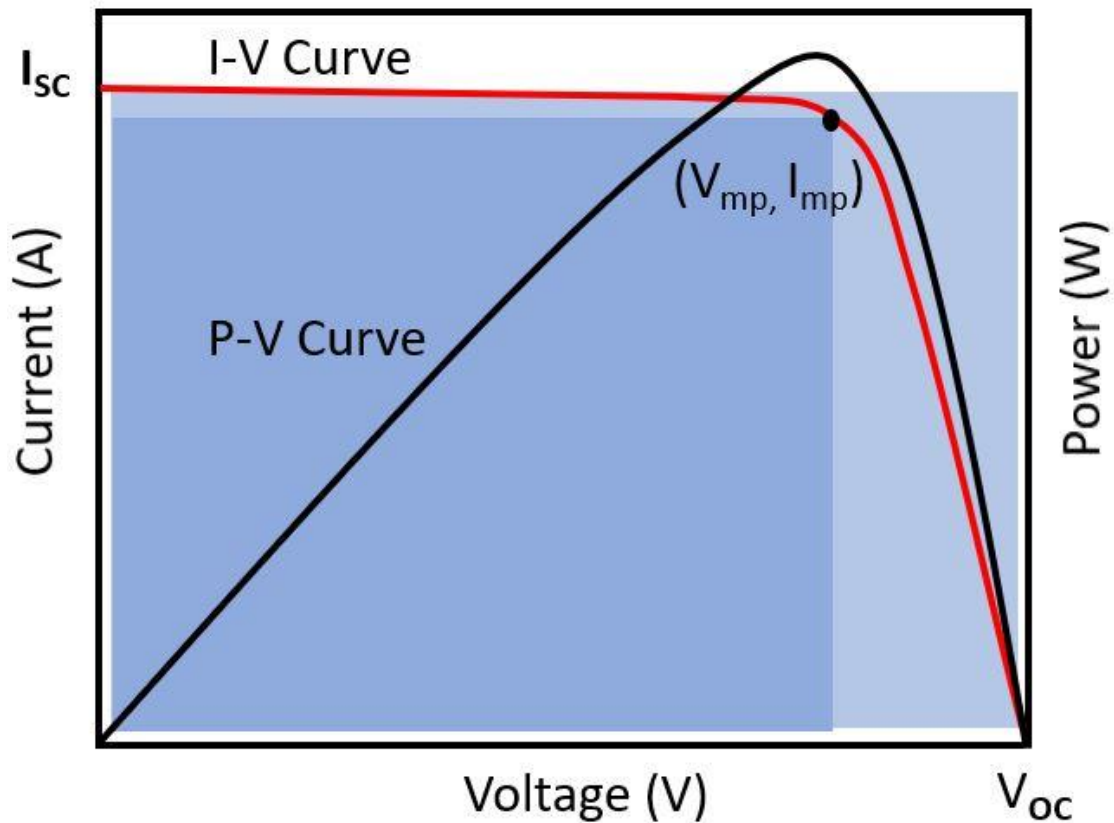


Figure 5. I-V curve and power output of a typical solar cell.

The solar cell's performance is not constant for different parts of the solar spectrum (Figure 6), so it is essential to determine the typical spectrum based on standard testing conditions. The solar radiation outside the earth's atmosphere (AM0) differs from radiation at the earth's surface (AM1.5) due to the absorption and scattering of photons of specific wavelengths. Air mass (AM) calculations are used to quantify the power loss as the light passes through the atmosphere. Air mass is defined as the path length that light travels through the atmosphere to the surface of the earth.

$$AM = \frac{1}{\cos\theta}$$

where θ is the angle of the sun's position with respect to its vertical. The standard spectrum at the earth's surface is AM1.5 Global with a power density 100 mW/cm^2 [63, 64].

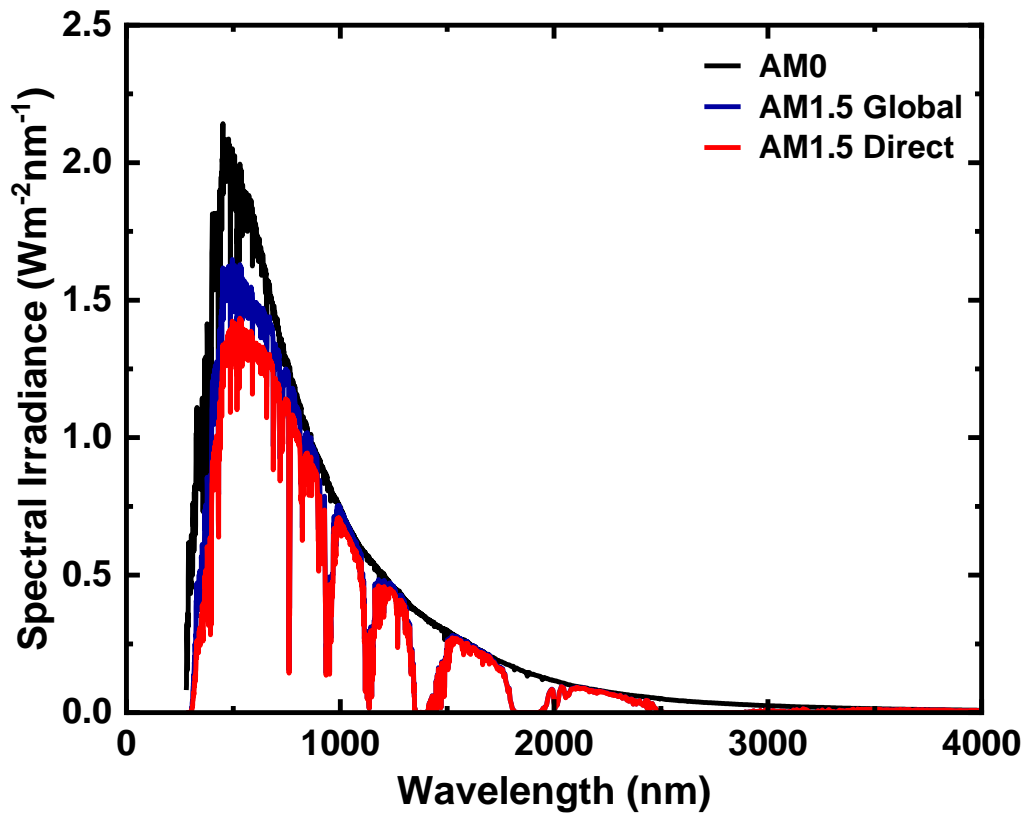


Figure 6. Spectral irradiance for AM0, AM1.5 Global and AM1.5 Direct solar spectrum [65].

2.3 QUANTUM EFFICIENCY

Quantum efficiency, $QE(\lambda)$, quantifies the capacity of the device to collect the photogenerated charge carrier. This measurement shows solar cells performance in the short-circuit condition as a

function of the wavelength of the incident light. The external quantum efficiency (EQE) measures the ratio of the number of photogenerated carriers to the number of incident photons arriving at the solar cell at each wavelength according to:

$$EQE(\lambda) = \frac{J(\lambda)}{q\Phi_0(\lambda)}$$

Here, Φ_0 is the initial photon flux, $J(\lambda)$ is the electric current density of the device as a function of incident photon wavelength, and q is the electronic charge. The photocurrent is the integral over the wavelength of the product of EQE with AM 1.5 Global illuminated spectrum and can be calculated as:

$$J_{sc} = \int q \times EQE(\lambda) \times \Phi_0(\lambda). d\lambda$$

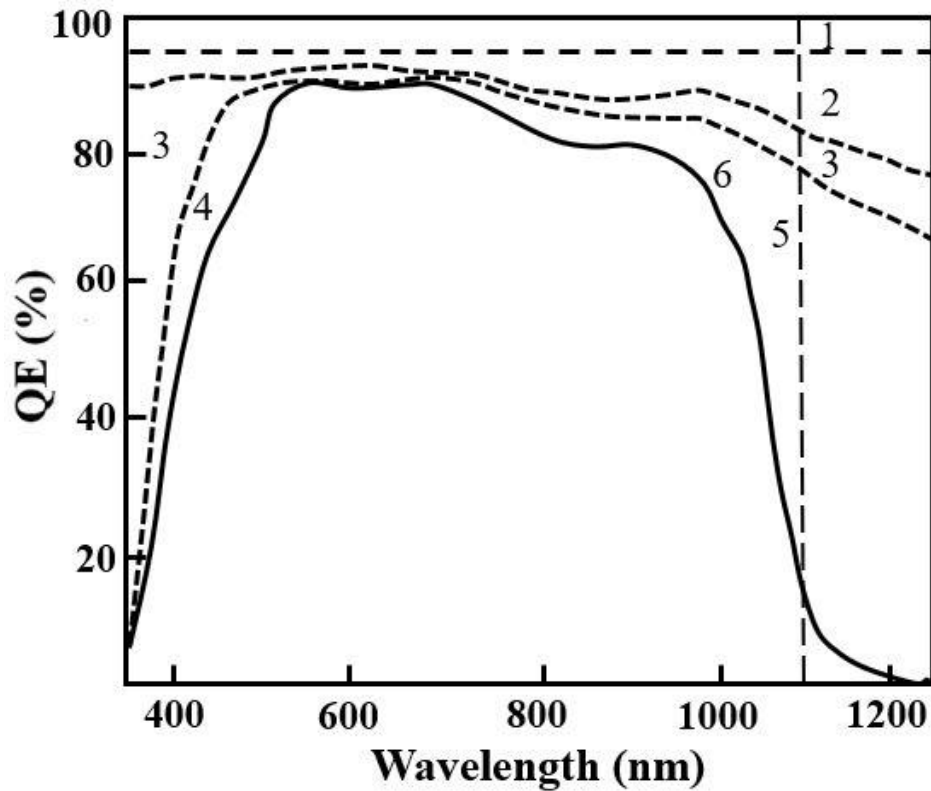


Figure 7. Quantum efficiency with optical losses in CIGS solar cell [66].

Quantum efficiency is often measured under zero bias. Device losses measured by EQE can be optical losses due to front reflection and absorption in the window layer or electronic losses due to recombination in the absorber. The EQE curve of a typical CIGS solar cell is shown in Figure 7 with respective loss mechanism highlighted as (1) wavelength-independent optical losses due to shading from collection grids, (2) front surface reflection losses at materials interface, (3) absorption in window layer as free carrier absorption, (4) absorption in the buffer layer as loss in quantum efficiency below $\lambda > 520$ nm accounts to the thickness of CdS buffer layer due to insufficient collection of the generated electron-hole pairs, (5) incomplete absorption in the absorber layer near the CIGS bandgap and (6) incomplete collection of the photogenerated carrier in the absorber [64, 66].

2.4 CIGS SOLAR CELLS DEVICE STRUCTURE

The I-III-VI₂ based thin film solar cells are heterojunction, where the absorber layer is the p-type layer, and the buffer layer is the n-type layer. Substrate configuration is the most widely researched configuration, with the substrate at the bottom and light entering the absorber layer through the top window layer. Figure 8 shows the typical CIGS solar cell structure and its corresponding band diagram. Starting from the substrate up to the surface, the standard substrate configuration consists of SLG as substrate, Mo layer as back contact, CIGS as an absorber layer, CdS (or Zn(O,S), In₂S₃) as buffer layer, intrinsic ZnO, In₂O₃:Sn (or Al:ZnO) as transparent conducting oxides and finally Ni/Al/Ni grids as front contacts. Mo is deposited on SLG substrate by dc magnetron sputtering to form an ohmic contact. The absorber layer with a typical thickness of 2 μ m is deposited by co-evaporation, and the p-n junction is formed immediately by depositing CdS by chemical bath deposition technique. The intrinsic ZnO is grown by rf sputtering, followed by the deposition of the ITO layer as front contact. In addition, metal grids at the top of the front contact support the current collection and complete the solar cell. Each layer has distinct physical and chemical properties and affects the device's overall performance, as described below.

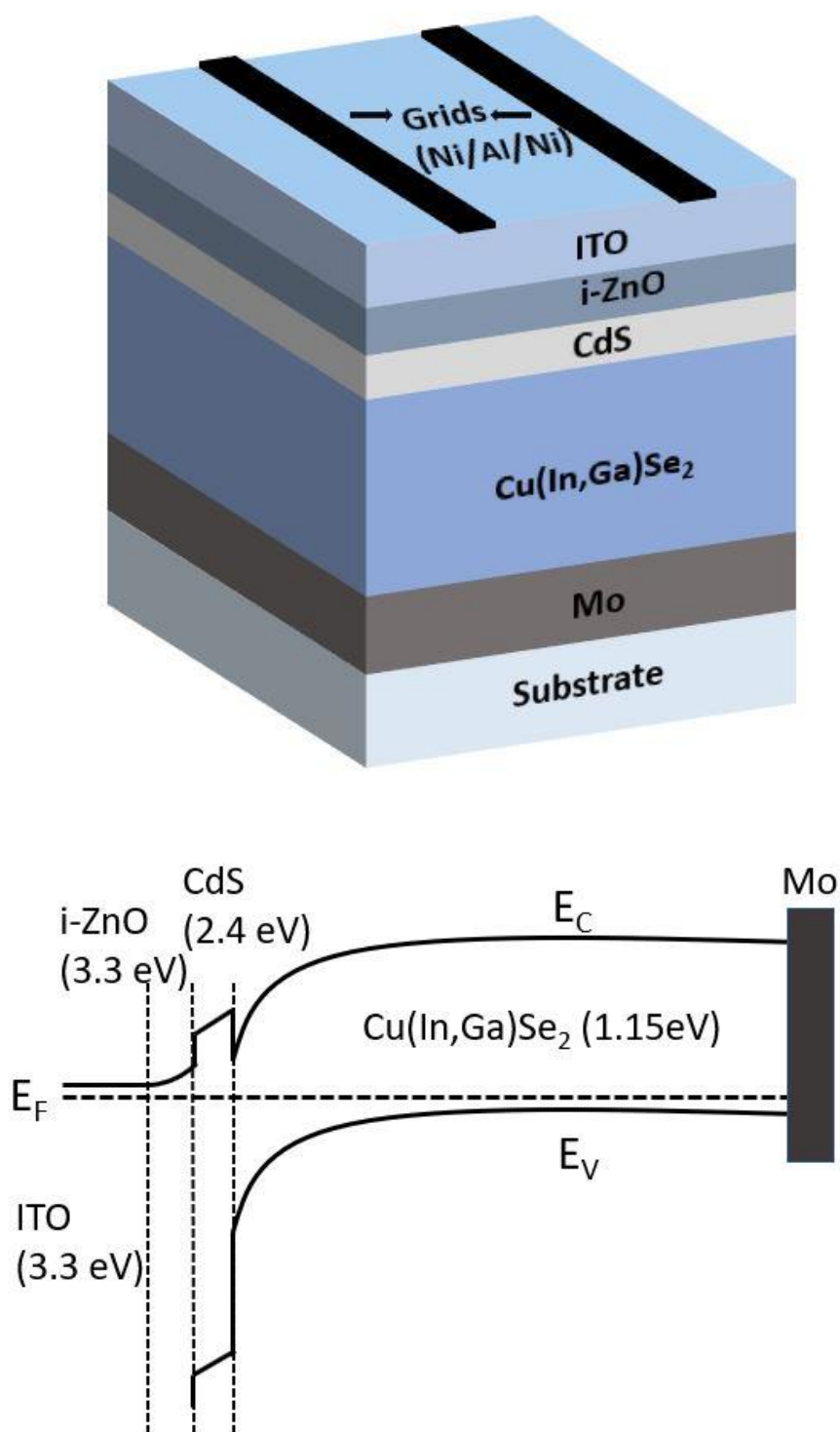


Figure 8. Schematic diagram of typical CIGS solar cell device (top) and corresponding band diagram (bottom).

2.4.1 SUBSTRATE

The substrate is a key component in the solar cell device. The basic condition for an appropriate substrate is that it should be vacuum compatible with the deposition process, thermally stable since most of the deposition process requires 400°C – 600°C, matching thermal expansion coefficient to avoid crack formations and chemical inertness as it should not decompose and release impurities [67]. Soda-lime glass (SLG) is the preferred substrate for I-III-VI₂ absorber (CIS and CIGS) solar cells as it has a well-matched thermal expansion coefficient with CIGS and has achieved the highest efficiency to date. Furthermore, diffusion of sodium and potassium out of SLG through the molybdenum back contact into the absorber improves morphology and enhances open-circuit voltage, fill factor, and hole density [68, 69]. The metal foils and polymers are the two major substrates used for flexible thin film solar cells and offer potential advantages compared to the SLG substrate. These substrates are recognized as lightweight, highly flexible, and facilitate manufacturing using roll to roll deposition, reducing the production cost, and developing to be highly effective. The temperature tolerance of polymer is only below 500°C, whereas metallic foils stand for growth around 500°C – 600°C but yield impurities diffusion during growth [70, 71]. They are considered favorable for space applications because of their radiation tolerance ability and high power/mass ratios [72].

2.4.2 BACK CONTACT

Molybdenum has developed as the dominant option for back contact material for the base electrode in I-III-IV₂ thin film solar cells because it acts as an optical reflector to reflect the light to the absorber layer, forms low resistivity ohmic contact, and has high conductivity. It is chemically and mechanically stable during the high temperature depositions process and has an optimum thermal expansion coefficient [73, 74]. The formation of a MoSe₂ layer during absorber layer deposition improves the adhesion and forms a back surface field due to a wider bandgap than CIGS. The CIGS/Mo contact, including MoSe₂ layers, is ohmic [75]. An optimum MoSe₂ thickness is required for better solar cell devices because a thick MoSe₂ layer increases the series resistance, and holes may not tunnel through the barrier. CIGS solar cells without MoSe₂ will have a Schottky junction [76]. Many other materials such as W, Cr, Ta, Nb, V, Ti, and Mn have been

used as potential replacements for Mo. Ti, V, Cr, and Mn react with Se, affecting the absorber layer, whereas W and Mo provide the best CIGS back contact interface passivation and improve V_{oc} [77]. Mo films deposited for solar cells are formed of a bilayer, the first layer is deposited at high Ar pressure is generally found to be under tensile stress, has good adhesion and high resistivity whereas the second layer deposited at low Ar pressure is under compressive stress, has poor adhesion and low resistivity [78, 79].

2.4.3 CIGS ABSORBER LAYER

The I-III-VI₂ semiconductors with a wide range of bandgap energies are ideal absorber layers for single-junction solar cells [40]. This chalcopyrite forms a significant group of semiconducting materials with various optical, electrical, and structural properties. They are structurally like their II-VI binary analogs with a much smaller bandgap [23]. CuInS₂, with a bandgap of 1.53 eV, though judged as the ideal material for absorber, has encountered problems in optimizing sulfur and diffusion of metals and impurities at low temperature, making it less advantageous relative to its counterparts. On the other side, CuInSe₂ (CIS) seems to have a wide range of anion to cation off-stoichiometry composition available as it is less sensitive to impurities, grain size, and crystal defects. However, the difficulty to control precisely the composition makes CIS a less plausible nominee for large-scale production [68]. The ternary chalcopyrite CIS crystallizes in tetragonal type space. It can be interpreted as a superlattice of a zincblende structure (Figure 9), doubling its unit cube along the z-axis, which becomes the c-axis of the chalcopyrite structure. The ratio c/a is called the tetragonal deformation [23].

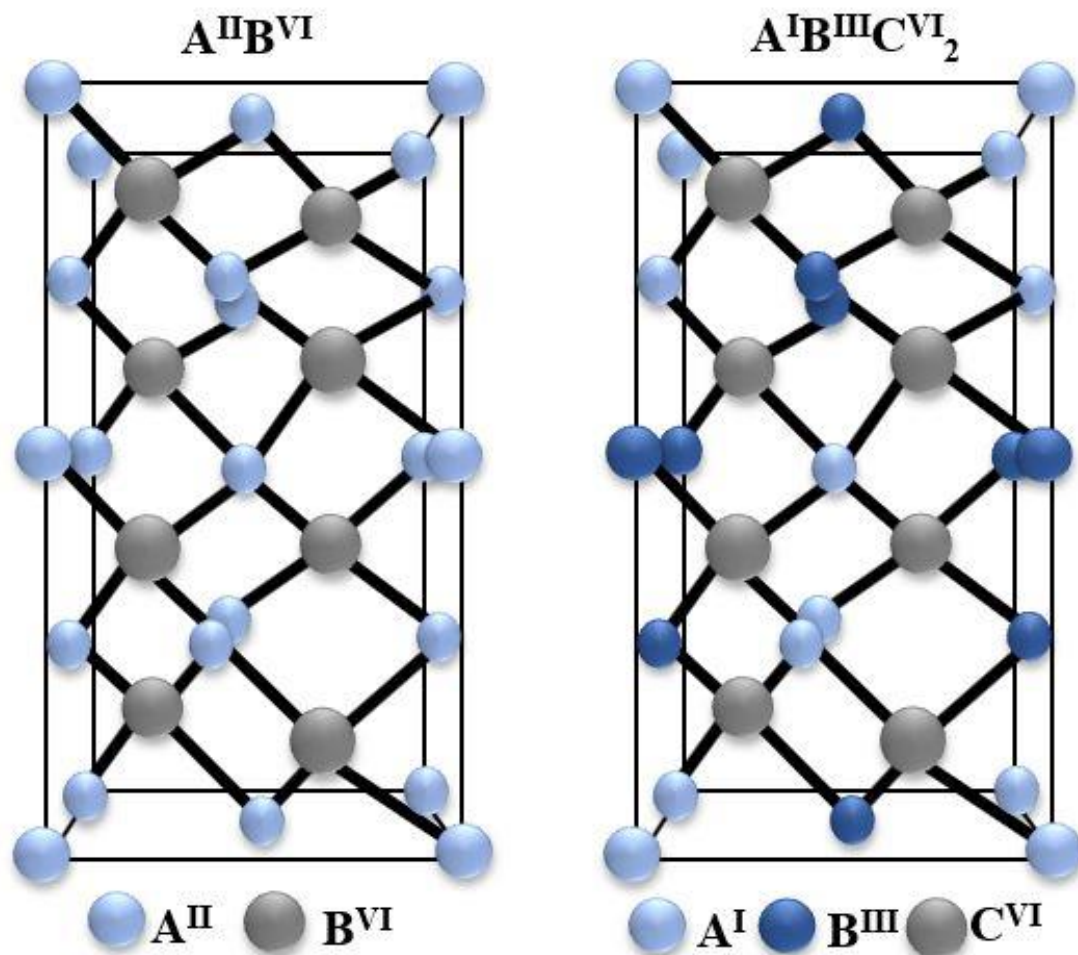


Figure 9. Crystal structure of zincblende (left) and chalcopyrite (right) [40].

In the CuInSe₂ ternary system, the Cu₂Se and In₂Se₃ phases allow building of the pseudo-binary system containing the intermediate CuInSe₂ phase (Figure 10). The β-phase (CuIn₃Se₅) has a defective chalcopyrite structure, and the γ-phase (CuIn₅Se₈) has a layered structure. The best high efficiency solar cell phase is the α-CuInSe₂ phase corresponding to space group I42d [80]. The δ-phase is unstable at room temperature and formed by the solid-phase transformation from either α or β-CuInSe₂ phase [81]. Its intrinsic defects dope CIS, and the deposition process affect the conductivity type of the film. Material grown in Cu-poor condition and annealed under high Se vapor pressure will results in p-type materials, whereas Cu-rich film with Se deficiency results in

n-type films [82]. The bandgap of CIS is lower than the ideal value for solar cells. However, these ternary semiconductors can be alloyed, yielding flexible properties from their chemical and structural freedom. For example, CGS is more suitable for application in thin film solar cells when alloying with CIS, yielding an ideal bandgap close to 1.4 eV [83].

CIGS crystalize in the chalcopyrite lattice structure (similar to a zincblende structure) in which Cu and In (or Ga) occupy the cation positions such that Se (anion) is bonded to two Cu and two In (or Ga) atoms. CIGS is a direct bandgap semiconductor due to the alignment of the maximum valence band and the minimum conduction band at the same value of the crystal momentum. Due to direct bandgap property of CIGS, the absorption coefficient rises promptly by order of magnitude at the bandgap energy, which allows a thin film of about 2-3 μm to be used as an absorber layer in the solar cell. Different alloys of quaternary chalcopyrite compounds can be formed and are found to show a composition dependence of bandgap following the equation:

$$E_g(x) = xE_g(1) + (1 - x)E_g(0) - b(1 - x)x$$

where the parameter b is referred to as the bowing parameter [81].

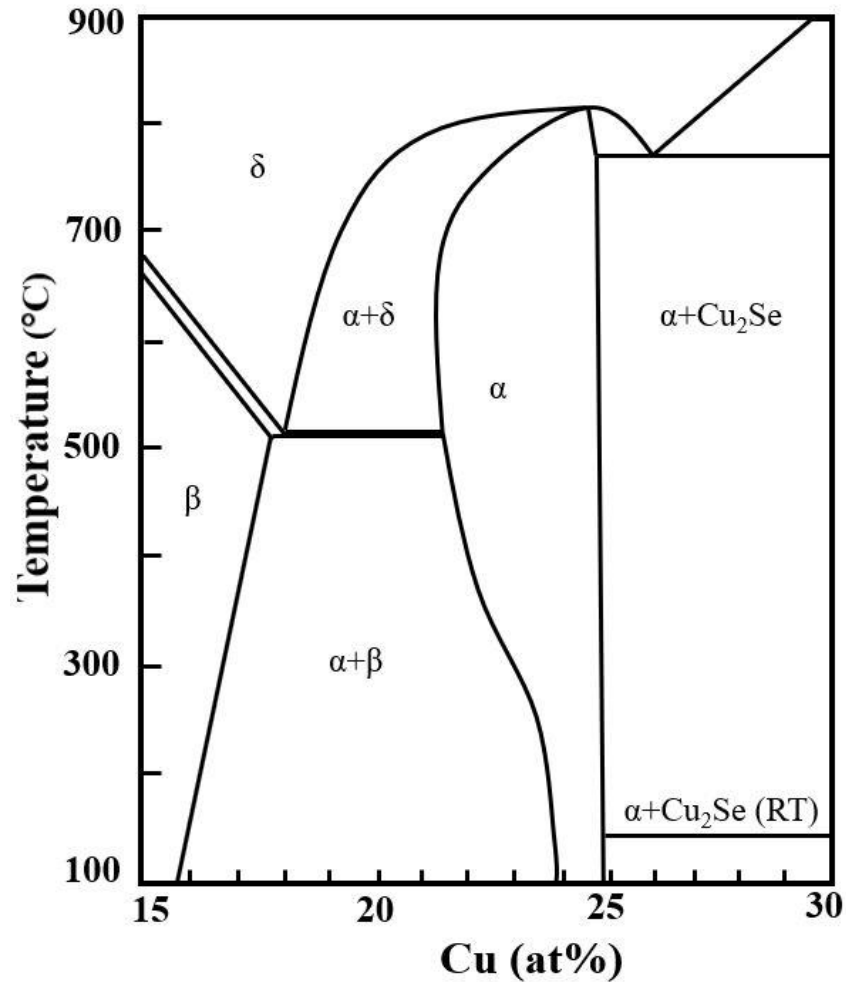
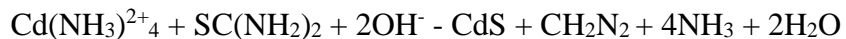


Figure 10. A pseudo-binary Cu₂Se-In₂Se₃ equilibrium phase diagram [81].

2.4.4 BUFFER LAYER

The buffer layers in solar cells are used to enhance lattice matching between the absorber and the window interface, protect against the sputtering damage during window deposition, and generate a buried junction [84, 85]. The chemical bath deposition (CBD) grown CdS is the most extensively used buffer layer in CIGS solar cells because of high solar cell conversion efficiency and high photoconductivity [86]. CdS is normally developed from the reaction between dissolved cadmium ions and thiourea molecules in ammonia solutions according to the standard reaction [87]:



However, there are few shortcomings of the CdS buffer layer. CdS is possibly toxic, which produces environmental risk. Also, technological problems are projected from the non-vacuum process such as CBD [88]. The bandgap of the CdS layer is 2.4 eV, which is quite low such that a certain amount of light is absorbed before it is reaching the absorber layer. Because of high recombination rates in CdS, restrict the level of optimum performance in the short wavelength region. To overcome these challenges, the development and use of substitute buffer layers like Zn(O,S), In₂S₃, (Zn,Sn)O₄, and (Zn,Mg)O were made in recent years. The bandgap energies of these materials are larger than that of CdS and can be tuned in range. As a result, blue absorption losses in the buffer layer are lessened as compared with solar cells containing the CdS buffer layer [89, 90].

2.4.5 FRONT CONTACT

Transparent conducting oxides (TCOs) are the fundamental part of the PV devices as they act as structural templates, electrode elements, diffusion barriers and regulates open-circuit voltage through work function [91]. The fundamental characteristics of TCOs are high visible wavelength transparency and electrical conductivity. The majority of the TCOs are n-type semiconductors, mostly intrinsic doping by native donors such as oxygen vacancies, impurities substitutions, and interstitial metal atoms that facilitate the flow of electrons [92]. TCOs must have bandgap energies above 3 eV and a carrier concentration of 10^{20} cm^{-3} for the use as a transparent electrode [93]. The most widely used TCOs are indium-doped tin oxides (In:SnO₂, ITO), fluorine-doped tin oxides (F:SnO₂, FTO), and aluminum-doped zinc oxides (Al:ZnO, AZO). ITO demonstrates outstanding electrical and optical properties with an intrinsic bandgap of 3.7 eV and low electrical resistivity [94]. Furthermore, germanium-doped indium oxides (IGO) and fluorine-doped indium oxides (IFO) are considered equivalent to ITO, whereas FTO is less expensive and shows good thermal and chemical stability. Based on cost and availability, ZnO based TCOs such as AZO, and gallium-doped zinc oxides (GZO) are considered potential alternatives to ITO for thin film solar cells. They present high transparency due to their wide bandgap, low temperature growth, thermal stability, and low resistivity [95].

CHAPTER 3

EXPERIMENTAL DETAILS AND CHARACTERIZATION TECHNIQUES

This chapter will discuss the Cu(In,Ga)Se₂ thin films and solar cells fabrication details and the deposition technique employed in this study. The various electrical and structural characterization methods used to analyze and understand the materials and device properties are also described.

3.1 SAMPLE PREPARATION

3.1.1 SUBSTRATE

2.5 × 7.5 cm² (1 mm thick) soda-lime glass (SLG) slides were used as the main substrate in this study. The sonicator cleaned SLG for 90 mins with Micro 90 soap (16 - 20 mL) solution. After that, SLG were rinsed thoroughly with deionized (DI) (18 MΩ) water and completely dried off with nitrogen gas.

3.1.2 BACK CONTACT

In this work, molybdenum was used as the back contact for the CIGS solar cells. The bilayer of Mo was deposited using a dc magnetron sputtering system (PVD 75, Kurt J. Lesker). Metallic grey 2.00-inch diameter and 0.125-inch-thick Mo targets were used with 99.95% purity. The bottom layer was deposited at high Ar pressure (7.5 mTorr) and the top layer was deposited at low Ar pressure (2.5 mTorr), using a constant power of 150 W. The approximate thickness calculated was ~800 nm.

3.1.3 CIGS ABSORBER LAYER

Single-Stage Process

The CIGS films were deposited on molybdenum back contact by a single-stage thermal co-evaporation process from independently controlled elemental sources of Cu, In, Ga and Se. The substrate temperature (T_{SS}) was kept constant throughout the deposition process. The deposition rate was monitored through crystal sensors. After completion, the substrate shutter was closed, and all the source temperature and substrate temperature were gradually decreased back to room temperature.

Three-Stage Process

The CIGS absorber layer was also deposited by elemental thermal co-evaporation with a three-stage process. In the first-stage, a precursor layer of (In,Ga)Se was deposited at a temperature of 350°C. During the second-stage, only Cu was evaporated onto the precursor layer at a temperature of 350°C or 400°C. The termination point or state of stoichiometry can be decided by endpoint detection [96]. The Cu flux stopped, and finally, in the third-stage, In and Ga was evaporated onto a Cu-rich layer to acquire the CIGS absorber layer with Cu-poor composition at a temperature of 400°C or 450°C [97]. The deposition time for CIGS was approximately 10 minutes. The Se flux keeps on constant throughout the process. The additional details about the experimental setup and deposition processes are discussed in the following chapters.

3.1.4 BUFFER LAYER

The junction was made by chemical bath deposition (CBD) of Cadmium Sulfide (CdS) as a buffer layer, instantaneously on the top of the absorber layer. Typically, the solution of the process first includes the mixture of 185 mL H₂O, 15 mL of Cd (CH₃COO)₂ in an aqueous solution of 6.74g/L, and 35 mL of NH₄OH (28%). The solution was kept in a hot bath of 70°C for 1 minutes. Then, the 15 mL of thiourea (H₂NCSNH₂) in an aqueous solution of 28.48 g/L, is added to the

solution. Finally, the samples were placed for 18 minutes in a heated bath and resulted in an approximate thickness of 50 - 80 nm.

3.1.5 FRONT CONTACT

A bilayer of transparent conducting oxides (TCOs), consisting of i-ZnO and ITO, was used as standard front contact and was deposited by rf magnetron sputtering. Both i-ZnO and ITO were deposited at Ar pressure of 5 mTorr and constant power of 100W. The targeted thickness was 60 - 80 nm for i-ZnO and 250 - 300 nm for ITO. The deposition was performed without heating the substrate.

3.1.6 METAL CONTACTS

Metal grids were consequently deposited by e-beam evaporation on the top of the TCO layers for device completion. It consists of three layers: 100 nm of Ni, then 2 μm of Al, and finally 50 nm of Ni. The grids were deposited through a shadow mask.

3.2 CHARACTERIZATION TECHNIQUES

3.2.1 SCANNING ELECTRON MICROSCOPY

A scanning electron microscope (SEM) scans a centered electron beam over a surface to produce an image. SEM comprises an electron gun, a lens system, scanning coils, an electron collector, and a display. The electrons released from the electron gun pass through the series of lenses to be focused and interact with the atoms in the specimen, providing distinct signals related to the surface morphology and composition. The signals induced by SEM involve notably secondary electrons, generated when the primary beam strikes the specimen, reflected electrons as back-scattered electrons (BSE), or emitted x-ray photons. SEM uses the secondary electrons to image the sample, back-scattered electrons to provide information about the bulk properties of the material, while the x-ray photons are used for elemental information about the specimen [98]. A

JEOL model 6060LV was used in this study for SEM imaging of the surface and cross-section of the specimen.

3.2.2 SECONDARY IONS MASS SPECTROSCOPY

Secondary ions mass spectroscopy (SIMS) is an exceptionally sensitive surface analysis technique used to determine the surface composition, distribution of dopants, contaminants in microelectronics materials, and their depth profile in solids. The procedure is element precise and can detect all elements as well as isotopes and molecular species. The basis of SIMS is the destructive removal of materials from the sample by ion sputtering and the analysis of ejected materials by a mass analyzer. The primary ion beam (Ar^+ , Ga^+ , Cs^+) strikes on the sample, and atoms from the sample are sputtered or ejected from the sample. The ion ejected from the material is called secondary ions. The mass/charge ratio of the ions is evaluated and detected on a mass spectrum. Based on the polarity of the sample, positive or negative secondary ions can be acquired. The SIMS experiments can be done in a dynamic or a static mode depending upon the total dose of primary ions imposing on the sample surface. Dynamic SIMS sputtered at a higher sputtering rate yielding depth profiles, whereas static SIMS operates at a low sputtering rate. In a time of flight (TOF) SIMS, the incident beam consists of pulsed ions instead of continuous sputtering with narrow slits in the spectrometer, increasing the ion collection. Consequently, the mass/charge ratio is substantial, and ions detection is much larger than other SIMS methods [98-100]. The depth profiles in this work were measured by TOF-SIMS analysis, using an ION-TOF SIMS V instrument.

3.3.3 X-RAY FLUORESCENCE

X-ray Fluorescence (XRF) is a fast, accurate, and non-destructive analytical technique to analyze the elements and their concentration in the material. It includes a wide range of elements and can measure a weight fraction range from traces to pure elements. The elements that can be investigated, their detection levels primarily depend on the spectrometer. The elemental range for energy-dispersive XRF goes from sodium to uranium, while wavelength dispersive XRF goes from beryllium to uranium. The elements within high atomic numbers have better detection limits than

the lighter elements. The XRF technique includes the exposure of a sample to x-rays characterized by an energy in the range of 0.125 keV to 125 keV in the electromagnetic spectrum. The incident x-rays removed the strongly bound electron from an inner orbital. The loss of electrons causes an atom in an electronically unstable configuration. To restore the equilibrium, the higher orbit electrons fill the empty inner shells. By determining the energies of the emitted radiation, and intensities of energies, it is likely to determine the elements and their concentrations. In this work, the composition of the CIGS samples was measured using Solar Metrology System SMX, XRF system. The primary x-rays at 65 keV with a 2 mm beam size and an exposure time of 30 seconds were used.

3.2.4 X-RAY DIFFRACTION

X-ray Diffraction (XRD) is a rapid and powerful non-destructive technique that offers qualitative information on crystal phases, grain size, preferred orientation, and crystal defects in the thin film structure. XRD techniques are based on the scattering of x-rays in an atom in a periodic array. Scattering occurs when the phase difference between scattered waves from an atom in the lattice plane is multiple of 2π , a condition met when the path length difference of scattered waves is an integral number of wavelengths λ . When an x-rays beam strikes a target specimen, x-rays are diffracted at various angles based on the specimen crystal structure. Diffraction peaks appear when Bragg's law ($2d\sin\theta = n\lambda$) is satisfied. The diffraction spectrum of the samples plotted as a function of 2θ . The diffracted peak position represents lattice plane spacing, which correlates to crystalline phases, and the interplanar spacing, d_{hkl} , is related to compositional or structural distortion of the atoms [99]. In this work, samples were analyzed by XRD measurements using a Rigaku Miniflex benchtop X-ray diffractometer in θ - 2θ configuration.

3.2.5 HALL EFFECT MEASUREMENT

Hall effect measurement is one of the powerful tools used for the characterization of semiconductor thin films. It is a fundamental method for evaluating electrical properties such as carrier mobility, bulk concentration, hall coefficient, hall voltage, resistivity, conductivity type, and magnetoresistance of the sample. The Hall effect is basic to solid-state physics, caused by the

action of a magnetic field on the current flowing in a solid. Hall effect is the production of a potential difference across an electrical conductor when a magnetic field is employed in a direction perpendicular to the flow of current. The underlying principle is the Lorentz force, which is applied on a charged particle q moving with velocity v through an electric field E and magnetic field B . The electromagnetic force F on the charged particle is given as; $F = qE + qv \times B$. The Van Der Pauw measurement method is generally used for the evaluation of electrical properties in semiconductor materials. The technique involves applying a current and measuring the voltage using four small contacts on the circumferences of a flat, arbitrarily shaped sample of uniform thickness, point contacts placed at the edges used for the measurements. In this work, hall effect measurements were done by Ecopia, HMS 3000 Hall Measurements System on films deposited on SLG.

3.2.6 CURRENT-VOLTAGE AND QUANTUM EFFICIENCY MEASUREMENTS

The current density-voltage (J-V) characteristics of solar cells were measured under simulated AM 1.5G illumination (1000 W/m^2) (Model: IV5, PV Measurement, Inc). Quantum efficiency was measured at room temperature using chopped monochromatic light in the range 300 - 1300 nm, usually in the step of 10 nm (Model: QEX7, PV Measurements, Inc).

CHAPTER 4

EX-SITU RECRYSTALLIZATION OF CIGS THIN FILMS

Thin film solar cells based on Cu(In,Ga)Se_2 established themselves in a new domain of high efficiencies solar cells after several modifications of the CIGS deposition process were made [20]. It is crucial to develop a better absorber layer and enhance back contact, buffer layer, and window layer. The important advancements are made in the device structure or process parameters to optimize the device to boost the energy conversion ability of the devices. The post-deposition treatment by alkali halides or supplied by soda-lime glass during the CIGS deposition process is considered a key to achieving such high efficiency [101]. The incorporation of alkali influences the structural and electronic properties of the CIGS bulk with an increase in open-circuit voltage (V_{OC}) caused by an increase in net acceptor concentration, and fill factor (FF). The KF post deposition treatments (PDTs) related to beneficial modification of the surface, increased hole concentration, grain boundaries (GBs) passivation, increased diffusion length, and decreased concentration of traps [102-105]. The properties of a polycrystalline semiconductor are affected by the properties of GBs, and efficiency improvement is associated with GBs passivation. For example, one can cite cadmium chloride treatment in CdTe solar cells [44] and polymer treatment in perovskite solar cells [106]. Furthermore, the selenization process under a Se-containing atmosphere is required to recrystallize the CIGS films to get a high quality absorber layer for better performance of the device [107, 108]. CIGS films selenized at 450°C display a densely packed, small grain structure and large grain boundaries, whereas an increase in the selenization temperature to 500°C produced a dense surface with larger grains [109]. Also, a higher Se-flux yields a decrease of the (112) preferred orientation and pores along the grain boundaries, ultimately degrading the device performance [110]. All these parameters are critical to keep in mind when designing new processes for CIGS solar cells fabrication.

4.1 EXPERIMENTAL DETAILS

Soda-lime glass (SLG) was used as the substrate. A molybdenum back contact was deposited by dc magnetron sputtering at a constant power density of 7.4 W/cm^2 . A tensile/compressive stress dipole was maintained as the bottom layer was deposited at higher Ar pressure (7.5 mTorr) and the top layer was deposited at a low Ar pressure (2.5 mTorr). The thickness of Mo was about 800 nm [111-113]. A single-stage co-evaporation process was used to grow CIGS thin films at a substrate temperature of 350°C . The source temperature and substrate temperature were kept constant. To compensate for the introduction of both In and Se during the post-deposition annealing process, the films were grown Cu-poor (elemental compositional ratio $\text{Cu}/(\text{In}+\text{Ga}) < 1$) and with a slightly lower $\text{Ga}/(\text{In}+\text{Ga})$ ratio than usual. The samples were inserted into a small annealing chamber after deposition. The annealing chamber was designed to ensure recrystallization of CIGS samples in a vacuum environment. The design consists of a CF flange, a 2.75" CF full nipple, another CF flange with a welded Swagelok high temperature resistant needle valve, followed by a pressure gauge connected to a rotary vane pump that can be disconnected. Sample holders made of quartz were used to hold the sample and halide compound inside the CF full nipple. The annealing chamber contains small quartz tube loaded with the samples to guarantee more fluxing agent interacts with the films. Two different annealing processes were used. One of them was a control anneal with just elemental Se. The elemental Se was used to avoid evaporation of Se from the films. The other one had a small charge of metal halides in addition to the Se. The chamber was pumped down to less than 10 mTorr and was annealed for a specific duration at various temperatures. The samples were then cool down. Finally, the samples were rinsed with deionized water to remove residual surface phases.

Surface and cross-section morphological analysis were performed by scanning electron microscopy (SEM) (JEOL JSM-6060LV). Depth profiles of the films were measured by time-of-flight secondary ion mass spectrometry (TOF-SIMS) analysis, using an ION-TOF SIMS V instrument. The depth profiling was achieved with a $100 \times 100 \mu\text{m}^2$ imaged area and a $300 \times 300 \mu\text{m}^2$ sputter-beam raster area. A 30 keV Bi^{3+} beam was applied as the testing beam scanned over the sputtered crater's center. A 2 keV Cs^+ beam with a current of 75 nA was used to sputter the sample for depth profiling. The film composition was measured by x-ray fluorescence (XRF). The

crystallographic structure evaluation was completed by symmetric θ - 2θ x-ray diffraction (XRD) and analyzed using the International Center for Diffraction Data (ICDD) database. The Hall effect was used to measure the electrical properties of the films.

4.2 RECRYSTALLIZATION BY INDIUM BROMIDE TREATMENT

One of the most essential criteria for CIGS modules fabrication is deposition at a high-rate and low-cost. The typical three-stage process includes a very high temperature to obtain the ideal Ga profile, which is costly, time-consuming, and influences the economic viability. The single-stage process is considered as faster to deposit, low-cost, and with high output for manufacturing purpose [42]. The grain growth in polycrystalline CIGS plays a vital role in the development of semiconductor quality. This can potentially be achieved by the post-deposition treatment and/or recrystallization of CIGS thin film [51]. The procedure could become more efficient with treatment via metal halides.

In this section, CIGS films deposited at 350°C were recrystallized with indium bromide (InBr_3) vapor treatment at two different temperatures of 400°C and 500°C to explore the viability and specifications required for post-deposition recrystallization. 50 mg of Se was used for the Se-annealing process, whereas 5 mg of InBr_3 was used in addition to Se for the metal halide recrystallization process. InBr_3 is highly hygroscopic and absorbs water vapor from the atmosphere. Because of this, during chamber loading, InBr_3 absorbs a significant amount of water, and some of that water remains during the annealing process. This water vapor might then react with our film and chamber walls, and add various impurities to our annealed film. The films were evaluated for their composition and morphological changes.

4.2.1 POST-DEPOSITION TREATMENT AT LOW TEMPERATURE

All films demonstrated drastic change when comparing characterizations before and after annealing. The results for each recrystallization temperature will first be looked at in detail. The as-deposited samples were recrystallized at 400°C in InBr_3 environment for a time of 30 minutes. The surface and cross-sectional images of CIGS samples before and after recrystallization was

captured by scanning electron microscope shown in Figure 11. A significant change in morphology can be noticed for the films after recrystallization by InBr_3 vapor treatment. This showed that recrystallization occurred even for these low temperatures of 400°C . The films developed from small structure for the as-deposited to larger grains size and increased thickness after annealing.

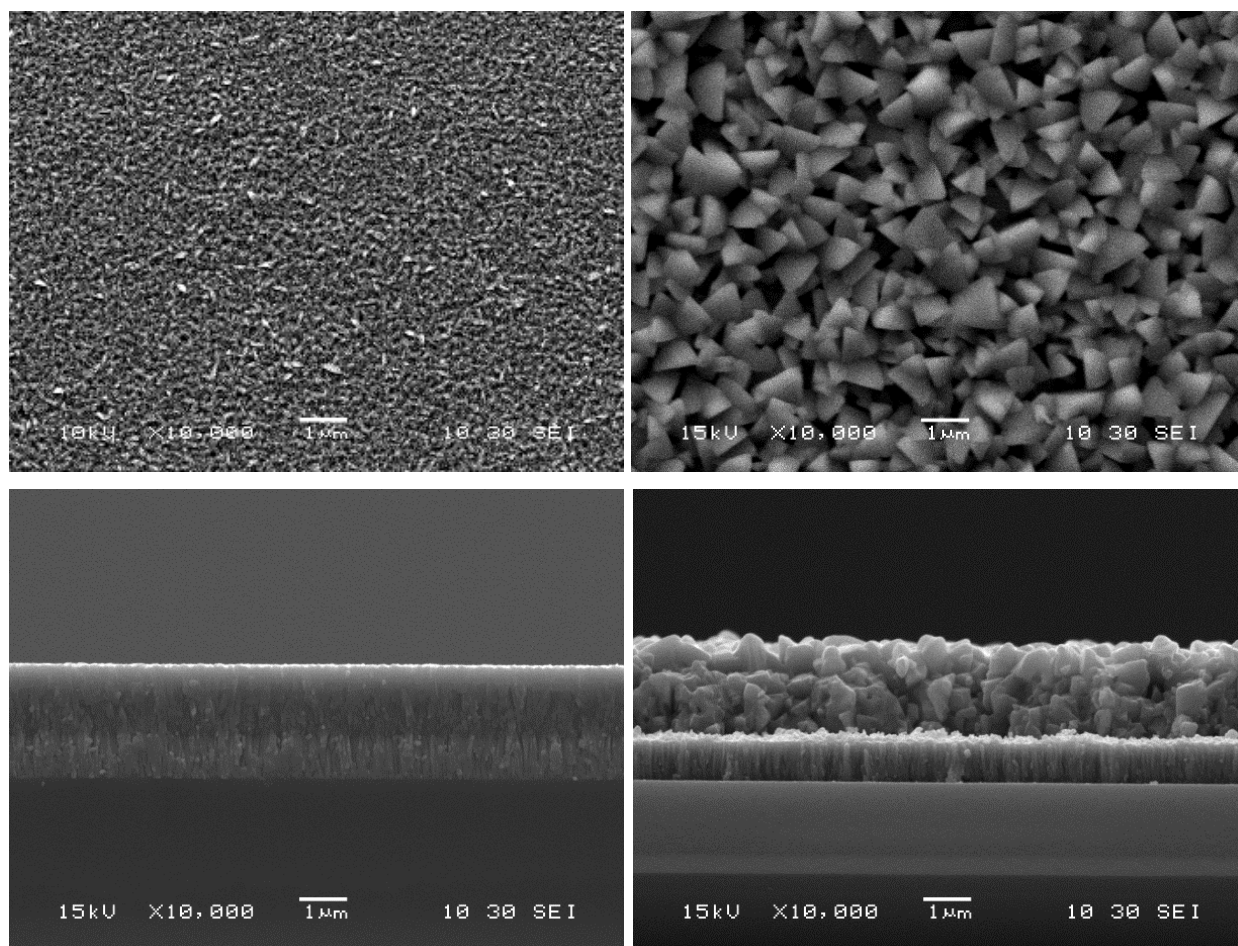
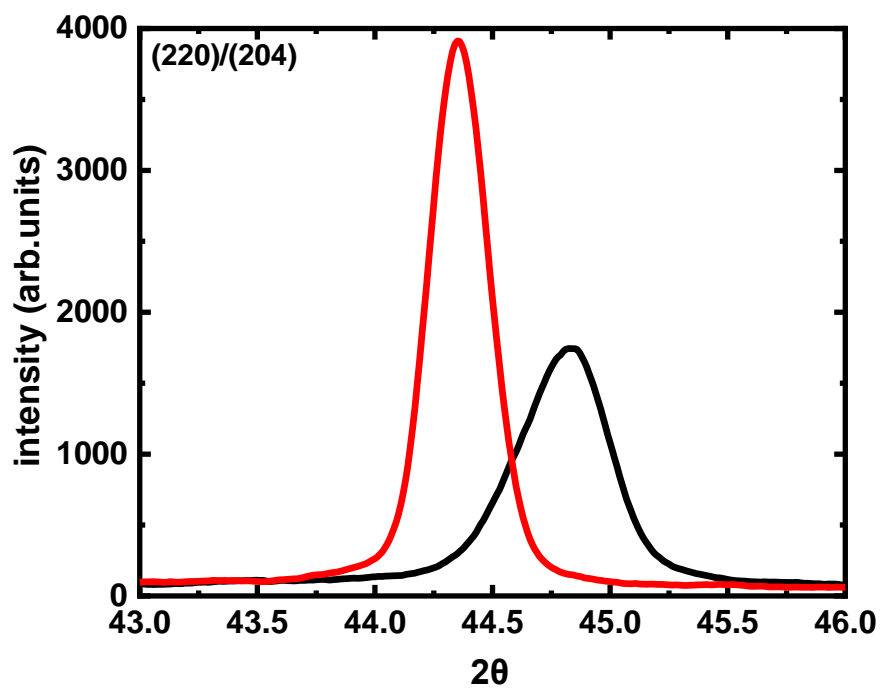
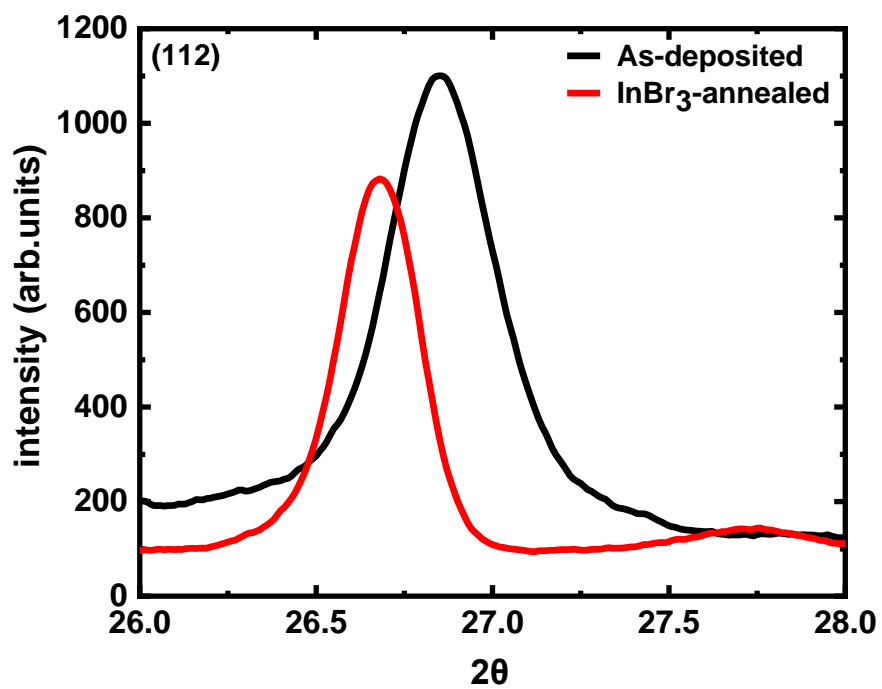


Figure 11. Scanning Electron Microscopy micrographs (surface and cross section) of CIGS films: as-deposited (left) and recrystallized (right) in InBr_3 at 400°C for 30 minutes.

To analyze how the crystalline structure of the films altered with InBr_3 treatment, XRD measurements were completed on the as-deposited and recrystallized films, as shown in Figure 12. The details of XRD parameters are presented in Table 1. The composition of Ga/III was 0.24, which was extrapolated from the XRD of the as-deposited films for the respective CIGS characteristics peaks. The XRF measurement was consistent with the XRD calculation. A change in all parameters can be observed after recrystallization. The films were slightly (220)/(204) oriented. The full width at half maximum (FWHM) decreases from 0.29° to 0.17° for the (112) peak. This connects well with growth in grain size seen by SEM. The films have a higher degree of preferential orientation along the (220)/(204) direction, indicating a preferential orientation change. The peak positions changes from higher to a lower angle, from 26.8° to 26.6° in case of (112) peak corresponding to a decrease in Ga/III ratio [114]. This was in good agreement with XRF results, suggesting a reduction of Ga/III from 0.24 to 0.05. The Cu/III ratio decreases from 0.85 to 0.72, resulting in more Cu-poor films. Indium was added to the films during the InBr_3 vapor treatment as the films become Cu-poor, as indicated by XRF measurement. The hall effect measurements results showed an enhancement of the conductivity from $1.9\text{E-}3 \text{ ohm}^{-1}.\text{cm}^{-1}$ for the as deposited films to $35.7\text{E-}3 \text{ ohm}^{-1}.\text{cm}^{-1}$ for the recrystallized films, due to increase in the carrier concentration from $5.0\text{E+}15 \text{ cm}^{-3}$ to $5.2\text{E+}16 \text{ cm}^{-3}$ and mobility from $2.4 \text{ cm}^2/\text{s}$ to $4.3 \text{ cm}^2/\text{s}$ as shown in Table 2.



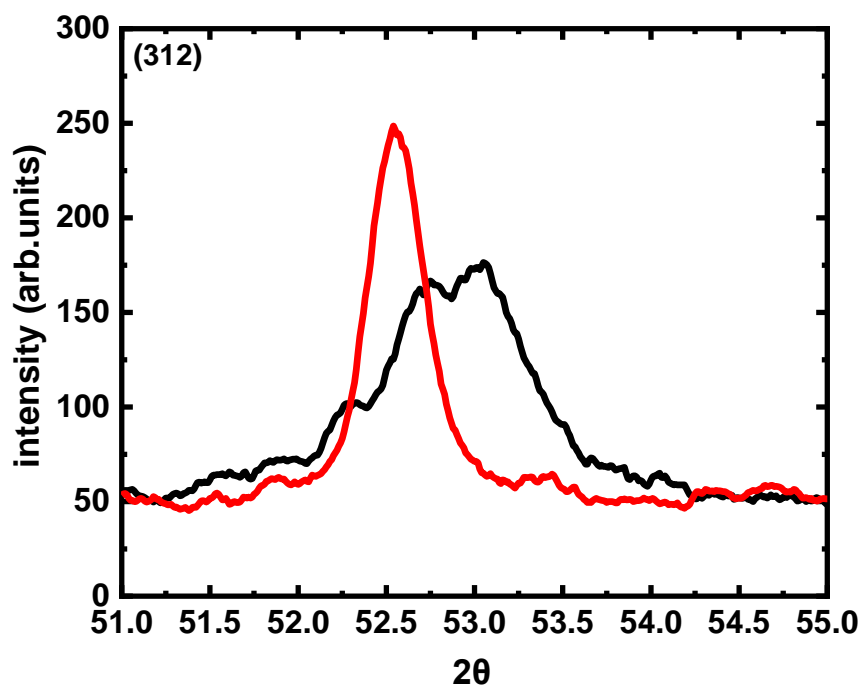


Figure 12. X-ray Diffraction plots of three key CIGS peaks (112), (204) and (312) for as-deposited (black) and InBr_3 -annealed (red) CIGS films at 400°C for 30 minutes.

TABLE 1. X-ray Diffraction data measurements and analysis of as-deposited and samples annealed by InBr_3 at 400°C for 30 minutes.

	Parameters	As-deposited			InBr_3 -annealed		
		(112)	(204)	(312)	(112)	(204)	(312)
XRD	Peaks	(112)	(204)	(312)	(112)	(204)	(312)
	Angles (deg)	26.8	44.8	52.9	26.6	44.3	52.5
	Intensity (counts)	1092	1714	170	890	3900	248
	FWHM (deg)	0.29	0.39	0.48	0.17	0.19	0.29
	Ga/III	0.24			0.07		

TABLE 2. X-ray Fluorescence and Hall Effect measurements of as-deposited and samples annealed by InBr₃ at 400°C for 30 minutes.

	Parameters	As-deposited	InBr ₃ -annealed
XRF	Ga/III	0.24	0.05
	Cu/III	0.85	0.72
Hall Effect	N _A (10 ¹⁶ cm ⁻³)	0.5	5.2
	Mobility (cm ² /s)	2.4	4.3
	Conductivity (10 ⁻³ ohm ⁻¹ .cm ⁻¹)	1.9	35.7

4.2.2 POST-DEPOSITION TREATMENT AT HIGH TEMPERATURE

A post-deposition treatment at a higher temperature was performed. Figure 13 shows the surface and cross-sectional SEM images of CIGS samples before and after recrystallization. The as-deposited CIGS samples were recrystallized at 500°C in Se and another set recrystallized at 500°C in InBr₃ environment with supplemental Se for 30 minutes. The increase in grain dimension for all annealed films were observed from cross-section and surface images, as the small grain size transformed into grains of micrometer sizes after the treatment. As seen in the surface SEM, the Se-annealed samples demonstrate only a slight change in microstructure, compared to the as-deposited. The significant microstructural evolution with larger grains can be seen clearly for the SEM micrographs of the CIGS films annealed in the InBr₃ environment. This showed increased surface faceting and enhanced surface roughness too. This suggests that InBr₃ vapor treatment not only promotes grain growth and recrystallization but also transport of matter, compared to Se-annealed samples.

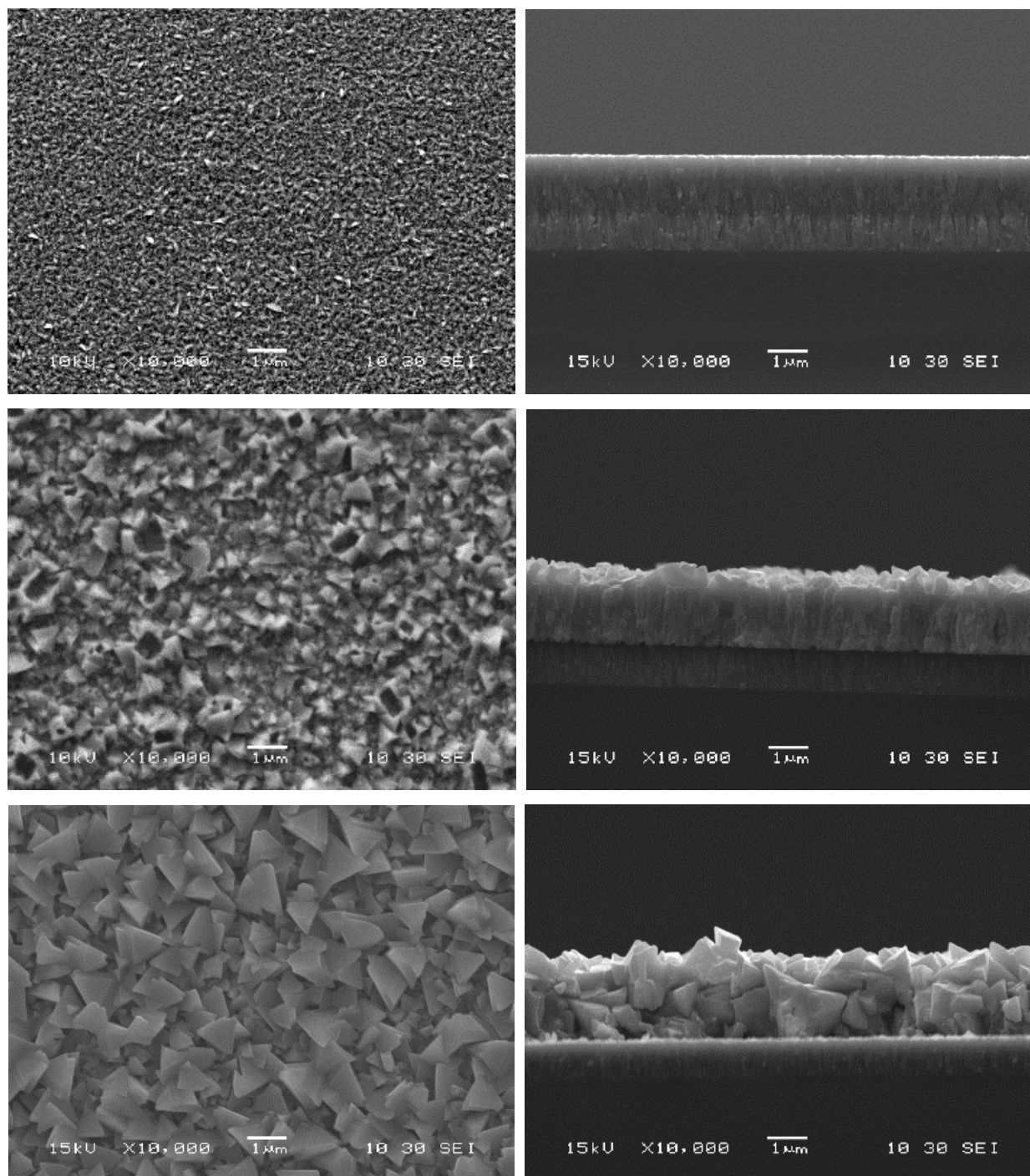


Figure 13. Scanning Electron Microscopy micrographs of CIGS films: as-deposited (top), recrystallized in Se (center) and recrystallized in InBr₃ (bottom) at 500°C for 30 minutes.

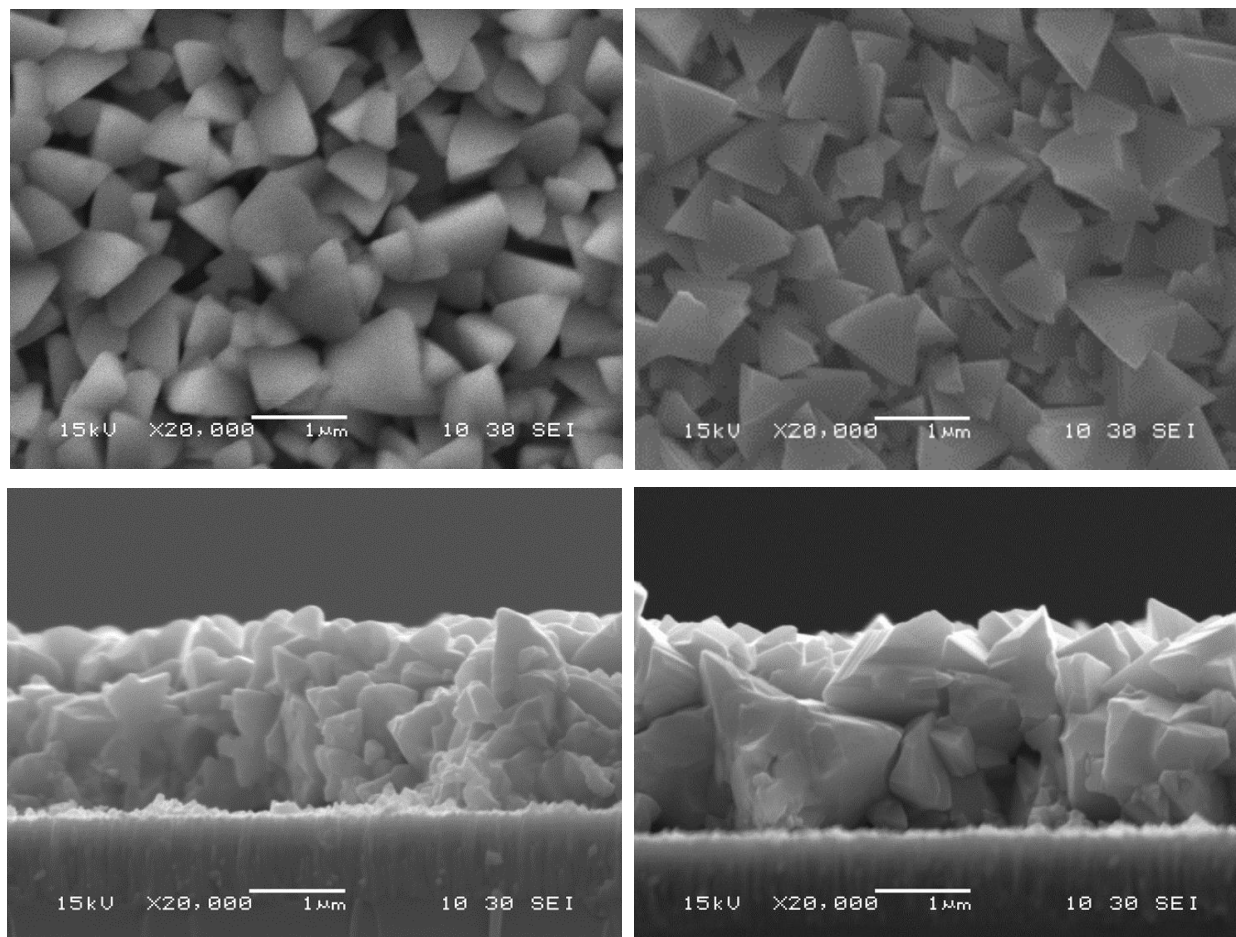


Figure 14. Scanning Electron Microscopy micrographs of CIGS films comparing recrystallization by InBr_3 at 400°C (left) and 500°C (right) for 30 minutes.

The annealing temperature plays the most crucial role in grain growth and its subsequent formation. Figure 14 shows the distinction in the development of grains by InBr_3 vapor treatment in terms of annealing temperatures 400°C and 500°C . The films deposited at 500°C showed more uniformity relative to films deposited at 400°C . No tiny crystals appeared on the surface as all crystals were fully integrated into films. The cross-section morphology showed larger and distinct grain size at temperature of 500°C in comparison to 400°C . Furthermore, no distinct delineation between upper and lower film was observed, whereas clear faceting was seen in films annealed at 500°C .

To interpret the structural evolution within the films, XRD measurements were performed on all three films, as shown in Figure 15. The corresponding parameters are shown in Table 3. No phase separation was seen for the (112) orientation. The development of a shoulder in the (220)/(204) XRD peak in the Se-annealed sample compared to the as-deposited sample indicates the formation of two distinct phases. The InBr₃-annealed films were preferentially oriented along the (220)/(204) direction, the Se-annealed films preferentially oriented along the (112) direction, and the as-deposited films were preferentially oriented along the (220)/(204) direction. According to Scherrer's formula, the full width at half maximum (FWHM) is inversely proportional to the grain size. Looking at the figure and table, an increase in grain size from the as-deposited films to the Se-annealed films, and a more significant increase in grain size from the Se-annealed films to the InBr₃-annealed films was observed, consistent with SEM micrographs.

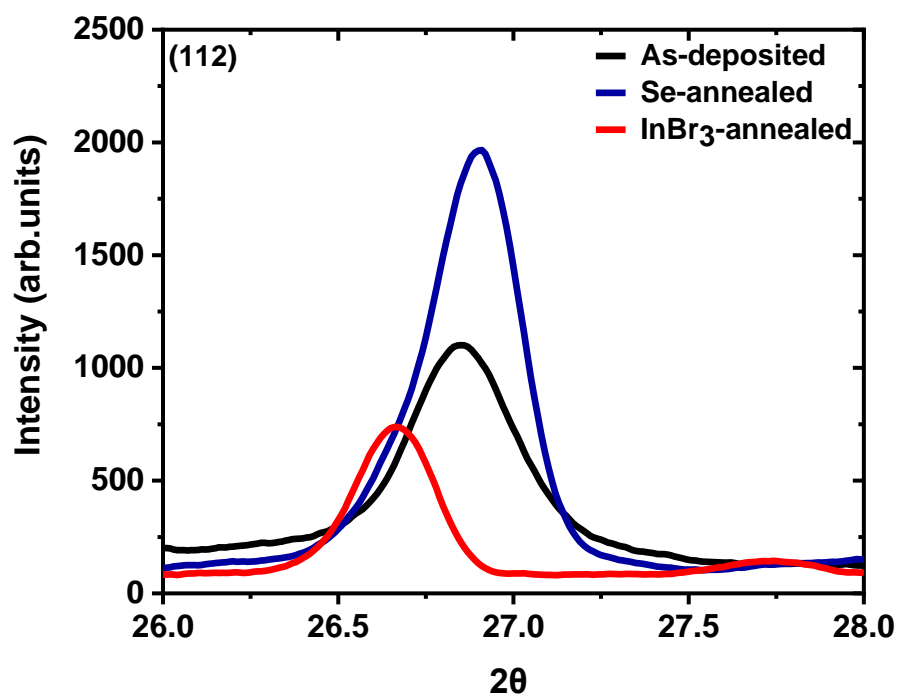
The elemental composition was also determined from XRD calculation for the respective position of CIGS characteristics peaks. This was in good agreement with XRF measurements (Table 4). There were two peaks, one with lower Ga content and one with higher Ga content as shown by XRD, representing a Ga redistribution in the film rather than the Ga depletion. As indicated by both XRF and XRD, on the other hand, the InBr₃-annealed samples become indium rich to some extent. Hall effect measurements were completed on CIGS thin films deposited on SLG and endured the same thermal treatment. The electrical properties of the films changed after the treatment. The results imply an improvement of the conductivity from 1.9E-3 ohm⁻¹.cm⁻¹ for the as-deposited films to 70.5E-3 ohm⁻¹.cm⁻¹ for the recrystallized films, due to both an increase in the carrier concentration from 5.0E-15 cm⁻³ to 7.1E-16 cm⁻³ and mobility from 2.4 cm²/s to 6.2 cm²/s as shown in Table 4.

TABLE 3. X-ray Diffraction data measurements and analysis of as-deposited and samples annealed by InBr₃ at 500°C for 30 minutes.

	Parameters	As-deposited			Se-annealed			InBr ₃ -annealed		
		(112)	(204)	(312)	(112)	(204)	(312)	(112)	(204)	(312)
XRD	Peaks	(112)	(204)	(312)	(112)	(204)	(312)	(112)	(204)	(312)
	Angle (deg)	26.8	44.8	52.9	26.8	44.3/44.7	52.9	26.6	44.3	52.6
	Intensity (counts)	1092	1714	170	1875	512/1688	320	719	3221	356
	FWHM (deg)	0.29	0.39	0.48	0.19	0.40/0.22	0.36	0.19	0.22	0.14
	Ga/III	0.24			0.09/0.30			0.08		

TABLE 4. X-ray Fluorescence and Hall Effect measurements of as-deposited and samples annealed by InBr₃ at 500°C for 30 minutes.

	Parameters	As-deposited	Se-annealed	InBr ₃ -annealed
XRF	Ga/III	0.24	0.24	0.04
	Cu/III	0.85	0.84	0.70
Hall Effect	N _A (10 ¹⁶ cm ⁻³)	0.5	1.8	7.1
	Mobility (cm ² /s)	2.4	3.5	6.2
	Conductivity (10 ⁻³ ohm ⁻¹ .cm ⁻¹)	1.9	10.1	70.5



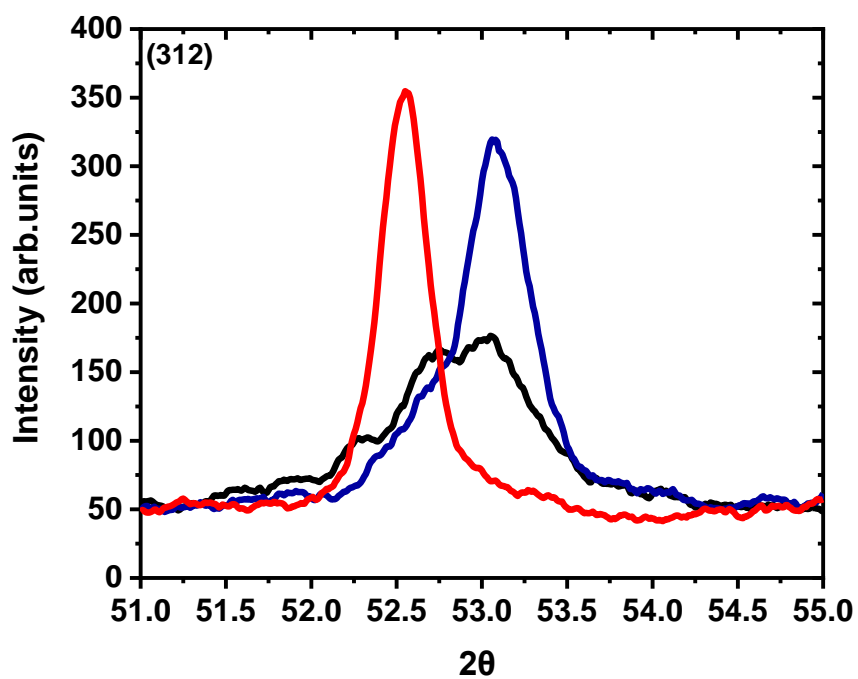
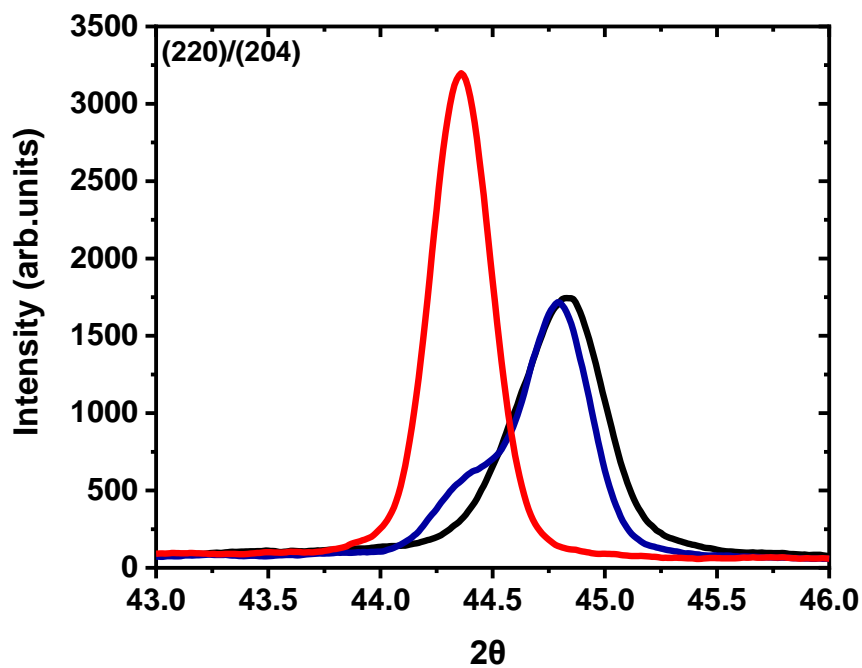
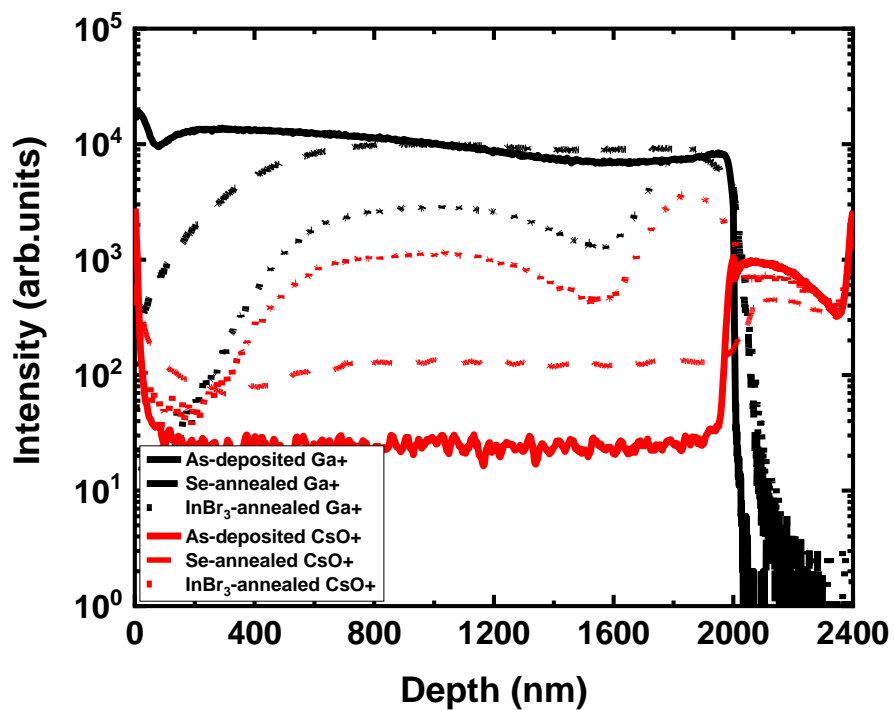
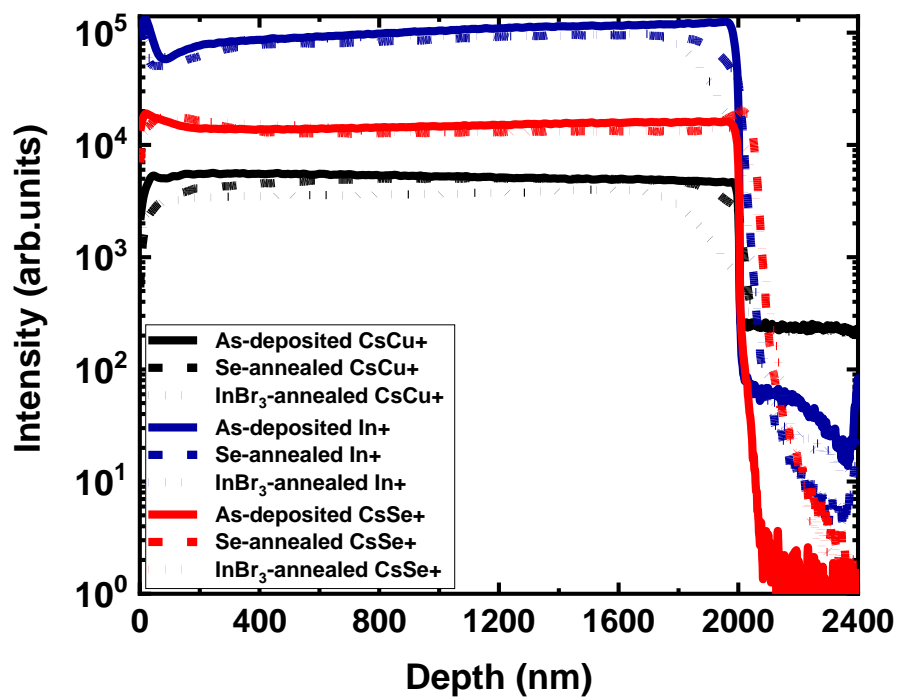


Figure 15. X-ray Diffraction plots of three key CIGS peaks (112), (204) and (312) for as-deposited, Se-annealed and InBr_3 -annealed CIGS films at 500°C for 30 minutes.

The samples were also studied by secondary ion mass spectroscopy (SIMS) to evaluate the impact of the recrystallization process on the elemental depth profile. The actual elemental composition cannot be determined by the analysis of the SIMS spectra because the intensity was not calibrated to any standard. However, this data allows for a great comparative study of the elemental profiles. Figure 16 shows the depth profiles of the positive ions of the main elements for all samples. The constituent elemental profile for CIGS main elements (Cu, In, Ga, and Se) and the corresponding existence of alkali (Na^+ and K^+) are consistent with CIGS films deposited by a single-stage process for as-deposited sample.

There was no variation in the three main element profiles specifically, Cu, In, and Se, after Se annealing treatment. Looking at the Ga and O_2 profile, there was a decline in the Ga concentration at the surface compared to the as-deposited samples. A small rise in O_2 content, at the surface and in the bulk of the films was also observed (Figure 16 center). In the case of Na profile, the intensity increases drastically by nearly two orders of magnitude (Figure 16 bottom). The overall intensity profile of K increases from surface to the bulk after Se-annealing treatment. The elevated temperature from the recrystallization process likely modifies the Na concentration, as Na diffuses from the glass, all through the molybdenum, into the CIGS layer [115, 116]. The Ga profile showed an unusual behavior, as Ga did not inter-diffuse even at 500°C . This property was used in developing the classical three-stage process, where no Ga is being deposited during the second-stage, leading to a lack of Ga in the middle of the device and an improved CIGS device efficiency [117, 118]. The change in Ga profile is more likely associated with the grain size transformation and rearranging of the elemental matrix, as seen by XRD and SEM. Another possible explanation is that Se functions as a fluxing agent along with Na [50], consequently redistributing Ga slightly at the surface. Indeed, XRF showed that the overall composition did not alter.



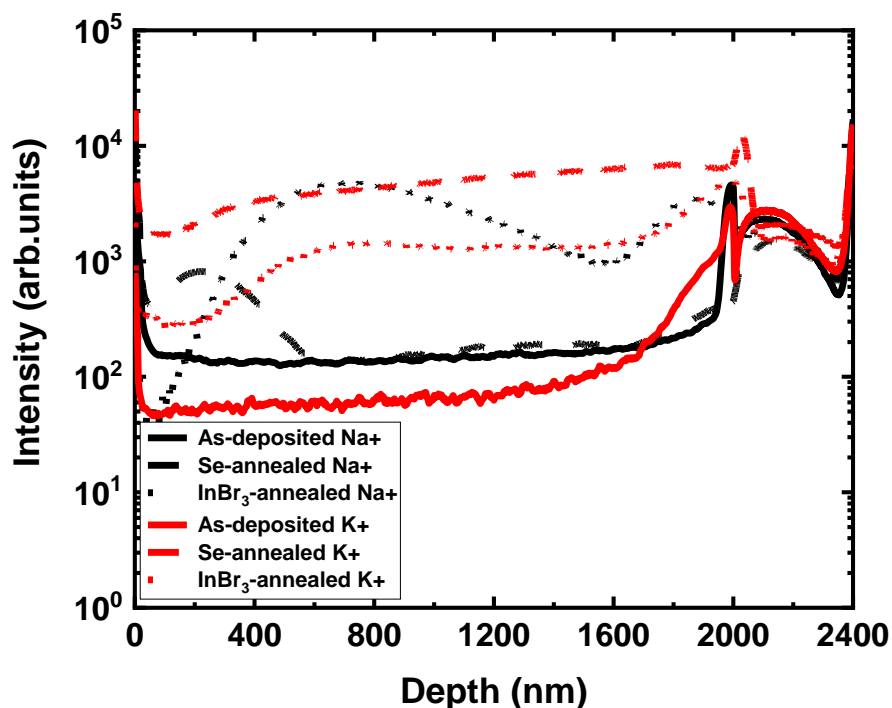


Figure 16. Secondary Ions Mass Spectrometry depth profile (positive ions) for the as-deposited, Se-annealed and InBr_3 -annealed CIGS films at 500°C for 30 minutes. Cu, In and Se ions (top), Ga and O ions (center), alkali ions (bottom).

Likewise, no noticeable change in the profile of Cu, In, and Se was observed after InBr_3 annealing treatment. Compared to the as-deposited, there was an overall decrease in the Ga intensity for the Se-annealed, most notably at the surface and all through the depth of the film. The same changes can be observed in the case of O_2 profile with a slight increase at the surface. This suggests that both changes were correlated in their method and occurrence. Looking at these O_2 profiles, significant increase in oxygen content in the Se-annealed and the InBr_3 -annealed samples was observed. While it is easy to do the in-situ Se-annealing process, by doing it within annealing chamber, it can be seen, how the effect of regular oxidation of the film during the annealing process occurs. The much higher CsO^+ and O^+ species present in the InBr_3 films showed how significant the problem of hygroscopicity of InBr_3 was during the annealing process.

The decrease in Ga content as measured by XRF and XRD was in good agreement with the measurement of depth profiles. The oxygen atoms were coming from the chamber (which was only evacuated to the level of 10 mTorr). A much lower level of oxygen was incorporated during Se-annealing. The change in grain structure during recrystallization due to the grain surface exposure to the atmosphere and the hygroscopic nature of InBr_3 might be potential causes for this effect. The recrystallization process seemed to affect Ga most but not the other main elements. A possible justification is that Br reacts with elements of a matrix. Both InBr_3 and SeBr_3 are volatile, and the added Se and InBr_3 frequently replenish them during the process. Furthermore, CuBr has a low vapor pressure, with a value of less than 10 mTorr at 500°C . On the other hand, as the boiling point of GaBr_3 is 279°C , the high vapor pressure of GaBr_3 causes it to be rapidly volatilized and could explain the depletion of Ga [119, 120]. Compared to the Se-annealed, the Na profile concentration increases instead of decreasing and follows the Ga profile in its shape. The K profile indicated a slight decrease in intensity. The increase in Na concentration from as-deposited to InBr_3 recrystallized films was related to increased carrier concentration [121].

Furthermore, how the advent of water vapor impacts the chemistry of the film was observed in the negative SIMS, as shown in Figure 17. One of the key concerns with water vapor in the annealing process was the introduction of impurities through a reaction of water vapor with the CF flange walls. Over time, both chloride ions and bromide ions could build upon the chamber walls over multiple deposition processes. While they would desorb due to heating under vacuum, the introduction of water vapor would further excite chemical reactions, possibly forming HBr and HCl vapors within the chamber. Transitioning to a quartz vacuum furnace will help mitigate these issues by improving the ability to bake out and clean the surfaces within the furnace.

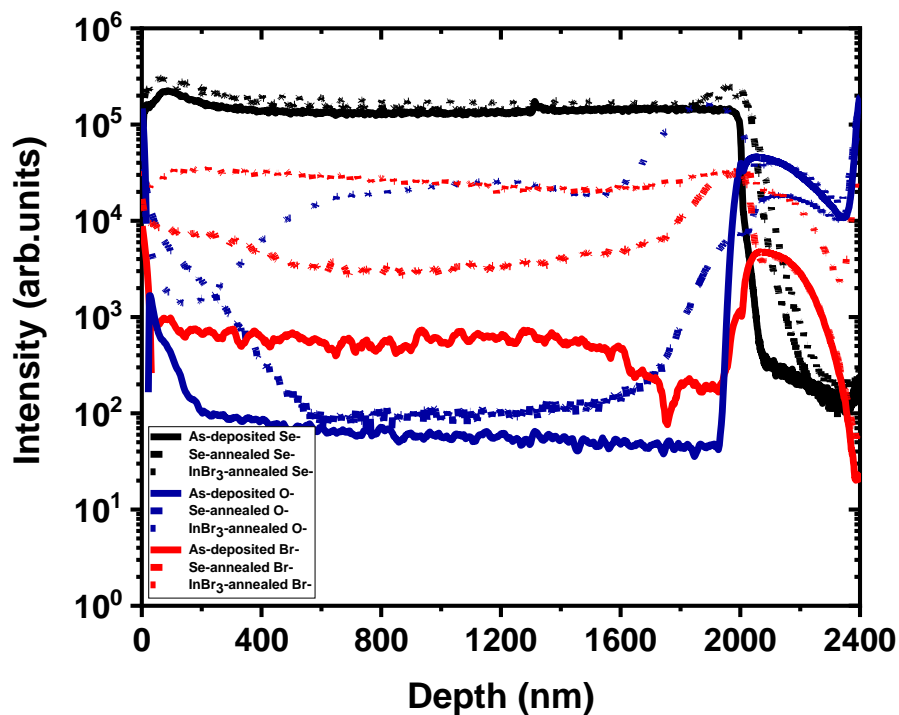


Figure 17. Secondary Ions Mass Spectrometry depth profile (negative ions) for the as-deposited, Se-annealed and InBr_3 -annealed CIGS films at 500°C .

4.3 RECRYSTALLIZATION BY INDIUM CHLORIDE TREATMENT

In this section, CIGS thin films were fabricated and annealed in the presence of InCl_3 as a fluxing agent at two different temperatures of 450°C and 500°C for 60 minutes to analyze the process of recrystallization. Similarly, to the InBr_3 process, CIGS thin films deposited at low temperature were placed in a quartz tube with 50 mg of elemental Se and 5 mg of InCl_3 . The compositional, structural, and morphological changes of the films were evaluated. The characterization techniques such as SEM, XRD, and SIMS were employed to understand the underlying changes due to the treatment.

4.3.1 LOW TEMPERATURE RECRYSTALLIZATION

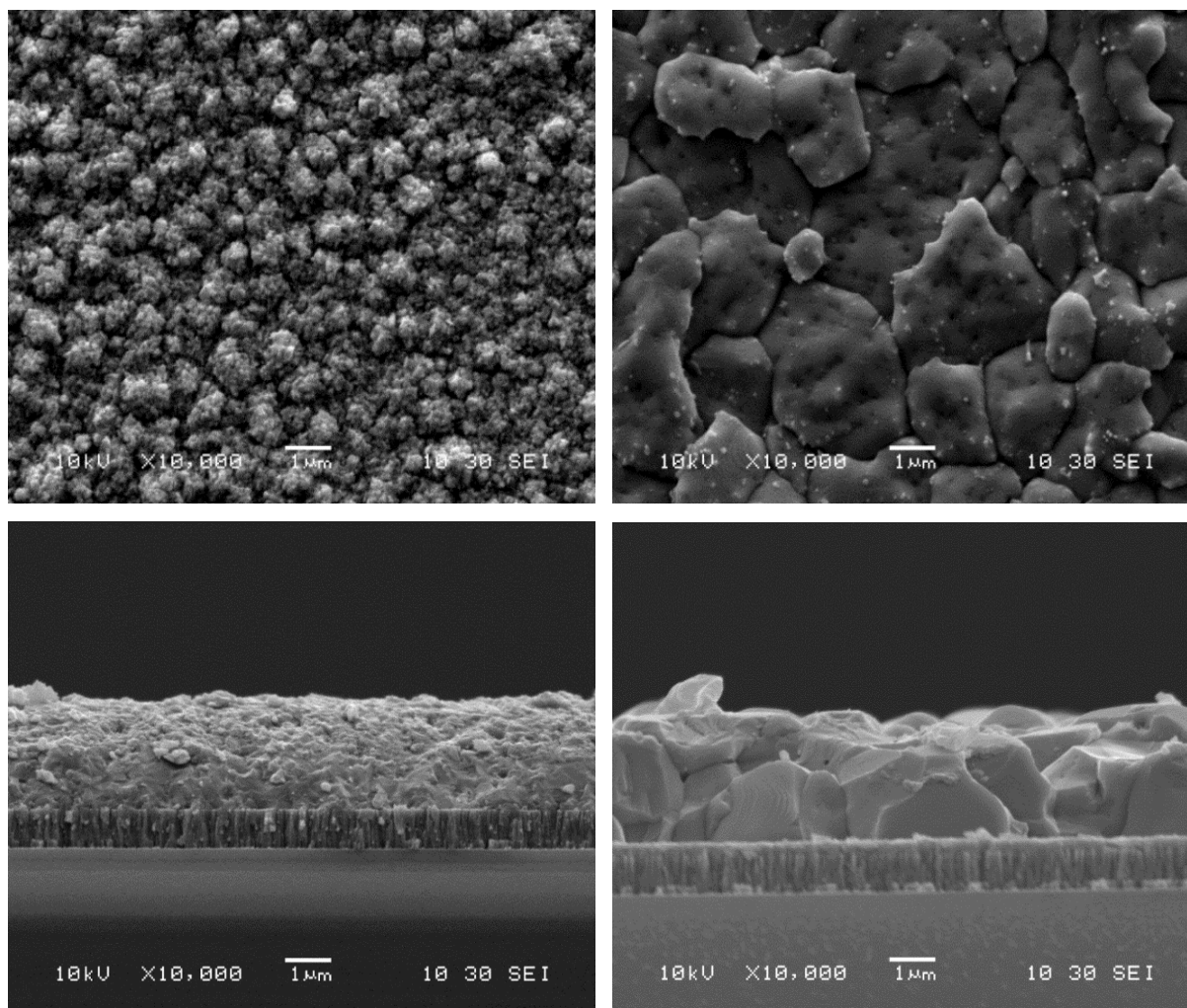
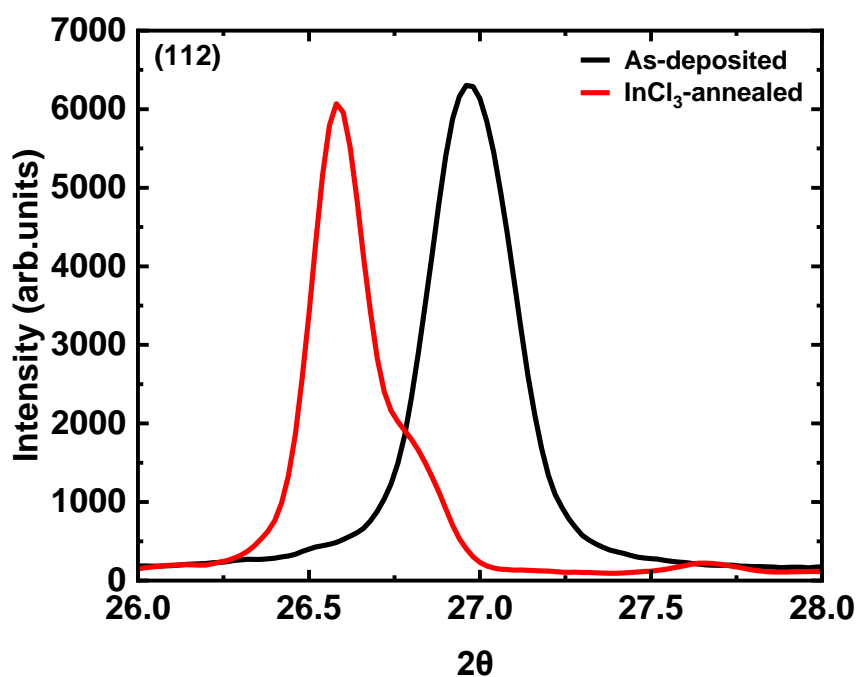


Figure 18. Scanning Electron Microscopy micrographs (surface and cross-section) of CIGS films: as-deposited (left) and recrystallized in InCl_3 (right) at 450°C for 60 minutes.

The as-deposited CIGS samples were deposited at 350°C. The samples were then recrystallized at 450°C for 60 minutes in an InCl_3 environment. Figure 18 shows the change of the surface and cross-sectional morphology before and after recrystallization. The variation in grain size and structure can be observed clearly. The small grain size in the as-deposited samples were changed into a larger than the micrometer size after 60 minutes of recrystallization. The surface image of the as-deposited film implies the surface is Cu-rich [122]. The larger grains on the surface might function as the seed sites for successive grain growth. Fully recrystallized films were observed after treatment, as surface grains seemed to completely vanish.



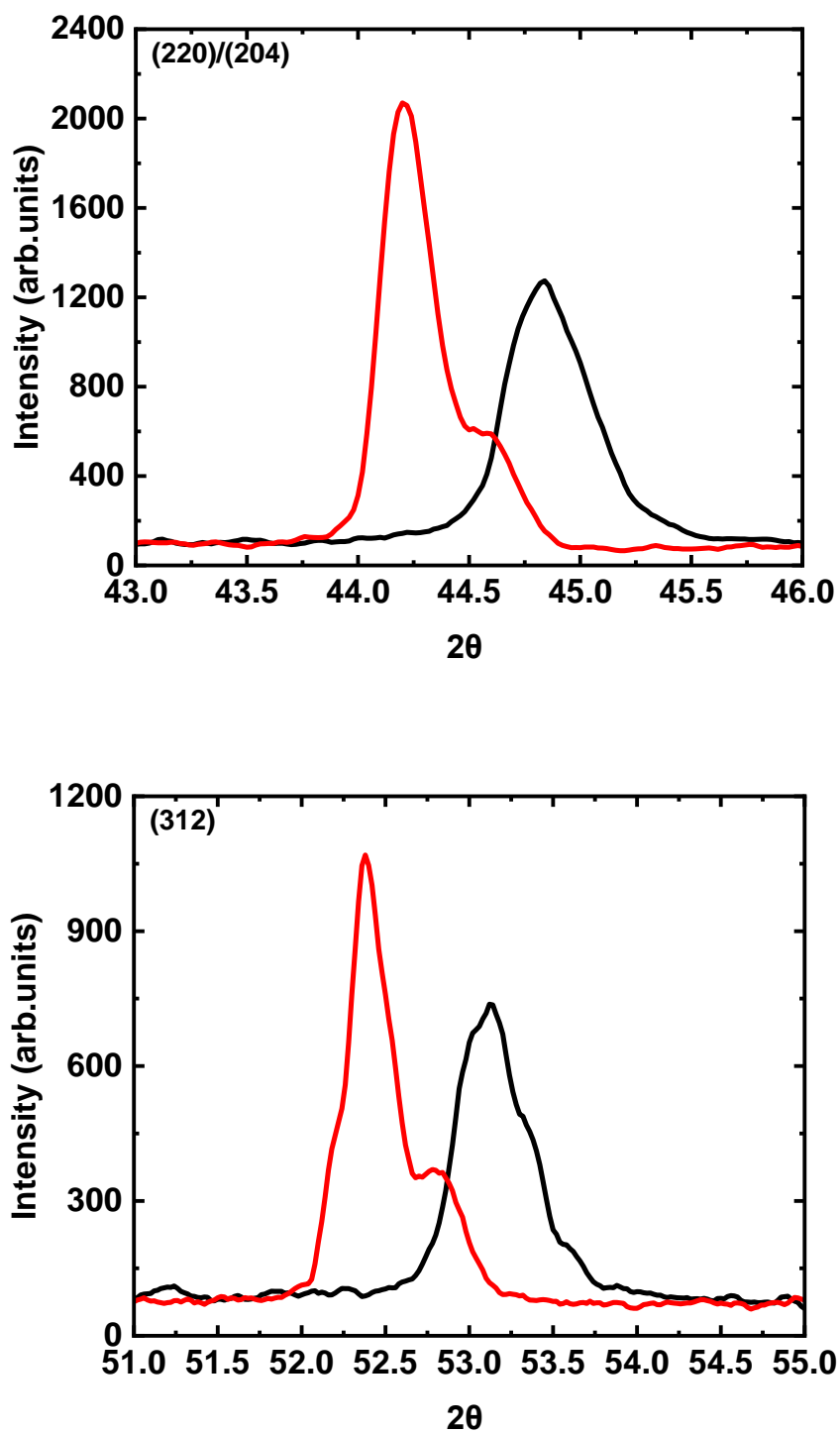


Figure 19. X-ray Diffraction plots of three key CIGS peaks (112), (204) and (312) for as-deposited and InCl_3 -annealed CIGS films at 450°C for 60 minutes.

XRD and XRF measurements were performed on the as-deposited and recrystallized films to know the microstructural and composition evolution of the films. Figure 19 shows the XRD plots of characteristics CIGS peaks of the as-deposited and recrystallized film by InCl_3 at 450°C . The respective parameters are shown in Table 5. The distinctive characteristic in the XRD spectra was peak shifting after the annealing treatment. This was in good agreement with a lower Ga concentration within the film, as measured by XRF.

TABLE 5. X-ray Diffraction and X-ray Fluorescence data measurements and analysis of as-deposited and InCl_3 -annealed samples at 450°C for 60 minutes.

	Parameters	As-deposited			InCl ₃ -annealed		
XRD	Peaks	(112)	(220)/(204)	(312)	(112)	(220)/(204)	(312)
	Angle (deg)	27.1	44.9	53.2	26.7/26.9	44.3/44.6	52.6/53.0
	Intensity (counts)	6220	1294	742	6035/1508	2085/587	1061/319
	FWHM (deg)	0.25	0.38	0.45	0.15/0.16	0.19/0.50	0.23/0.26
XRF	Ga/III	0.42			0.24		

The film revealed (220)/(204) preferential orientation as well as peak intensity increases and FWHM decreases after the treatment, indicating the increase in the film crystallinity, which was consistent with the SEM results. The intensity of the (112) peak seemed to be lower as compared to the as-deposited. The decrease in Ga content after the treatment most probably results from either the film losing Ga through halide-mediated evaporation, or the additional indium brought during recrystallization.

4.3.2 HIGH TEMPERATURE RECRYSTALLIZATION

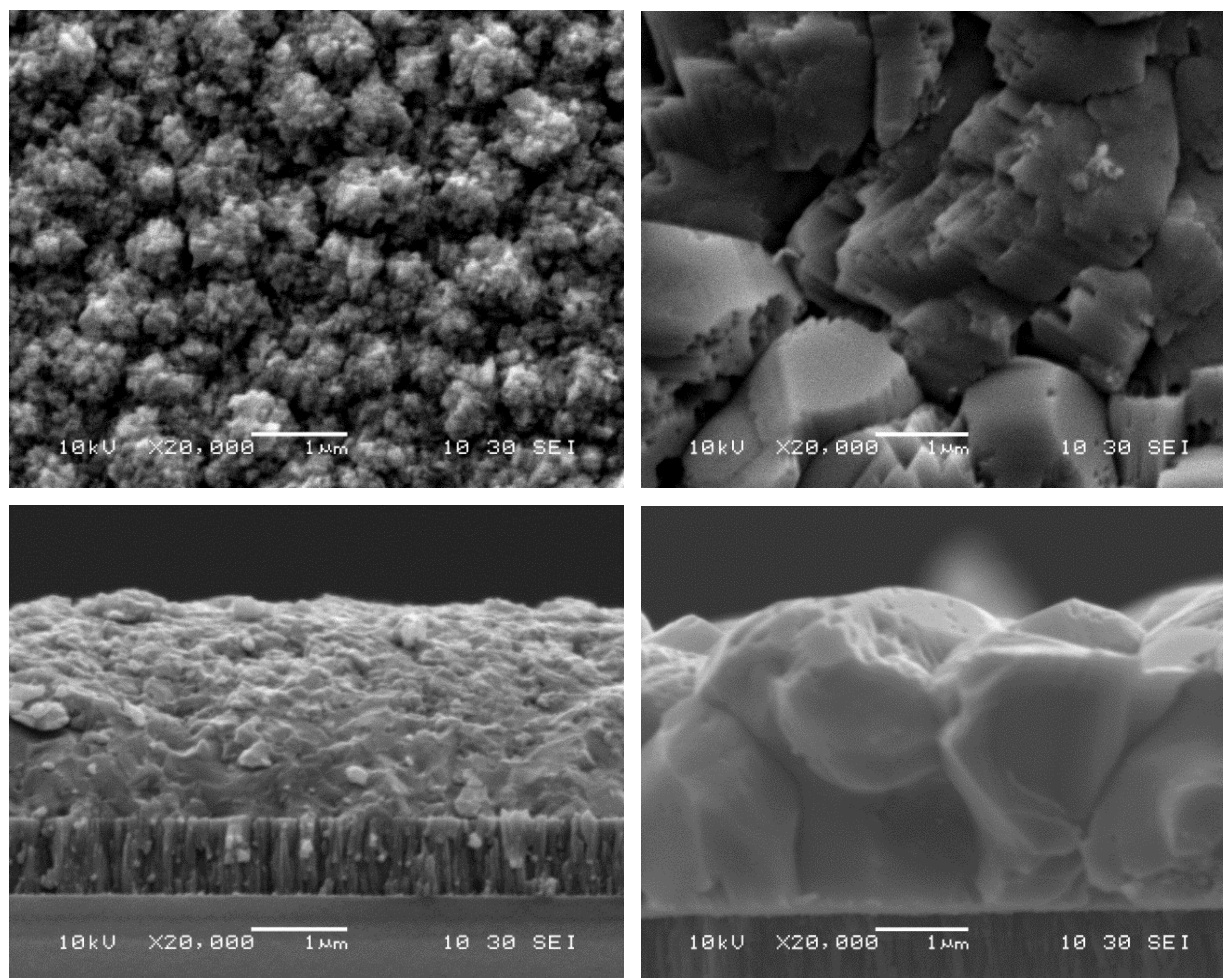
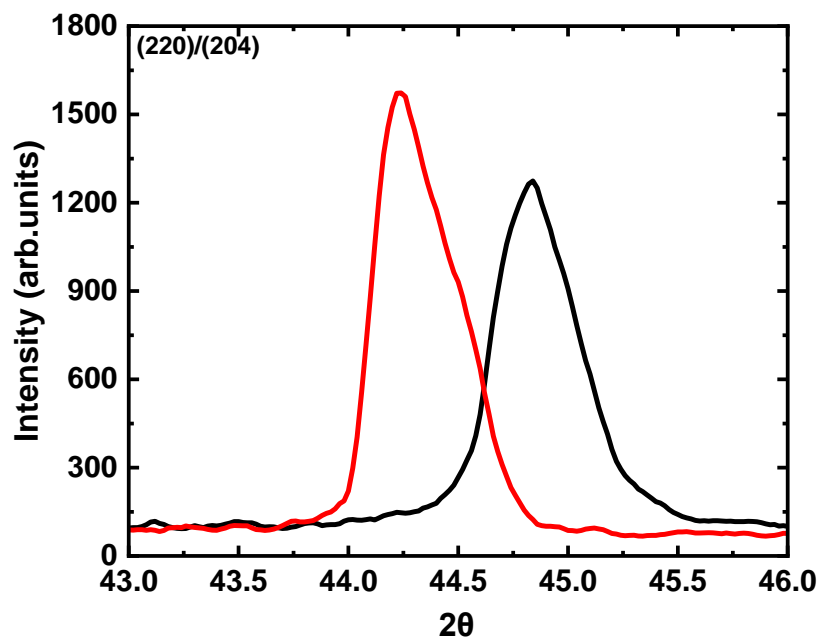
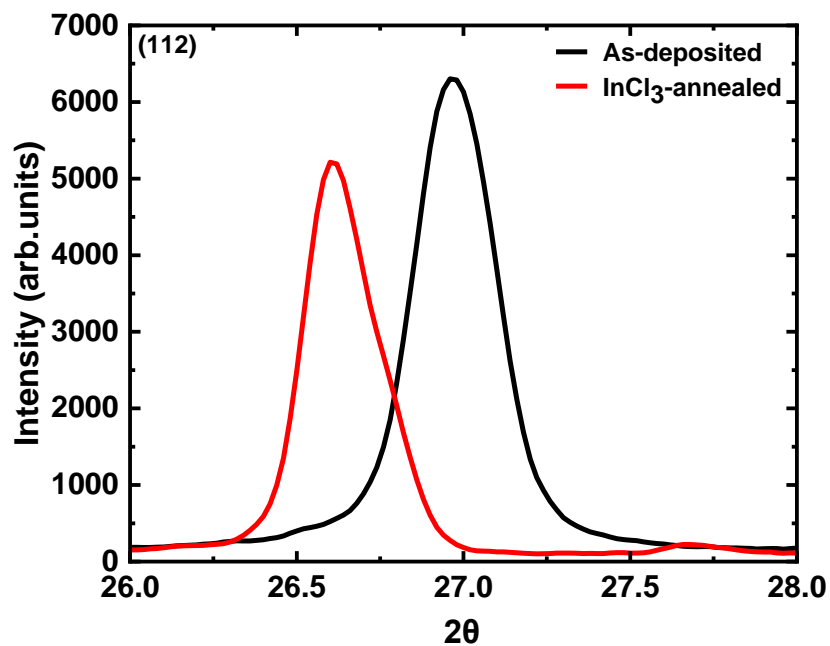


Figure 20. Scanning Electron Microscopy micrographs (surface and cross-section) of CIGS films: as-deposited (left) and recrystallized in InCl_3 (right) at 500°C for 60 minutes.

Similarly, CIGS samples fabricated at 350°C were recrystallized at 500°C in an InCl_3 environment for 60 minutes. Drastic changes were observed on these films surface and cross-section morphology after the recrystallization, as shown in Figure 20. The substantial grain growth was noticed as small grains changed into large grains. The film recrystallized at 500°C showed different behavior as compared to the film deposited at 450°C . An extensive surface faceting was

observed at 450°C, whereas, at 500°C, there was some faceting, but large, compact, continuous grains were observed. The high temperature seemed to help in improving the grain size and consistency of the film after recrystallization.



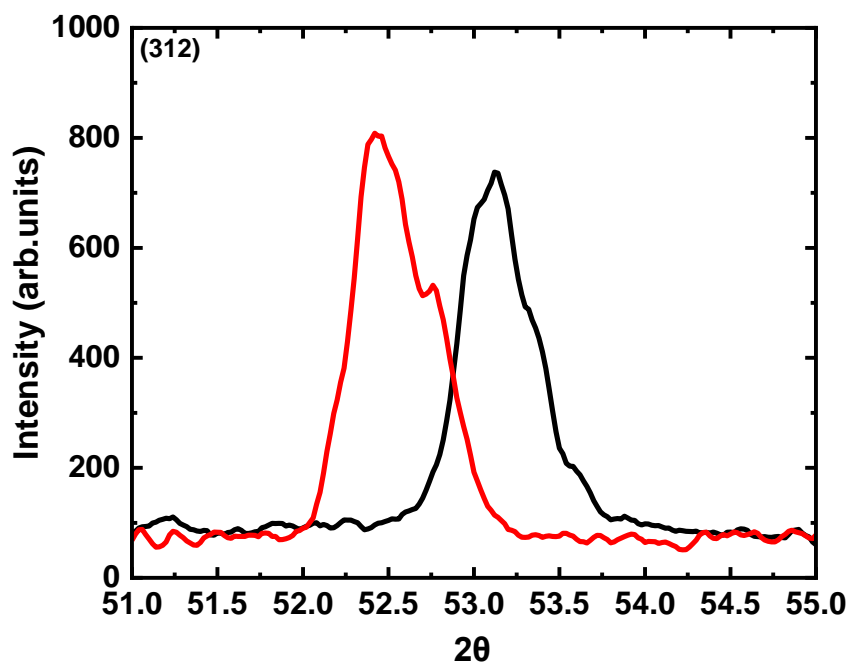
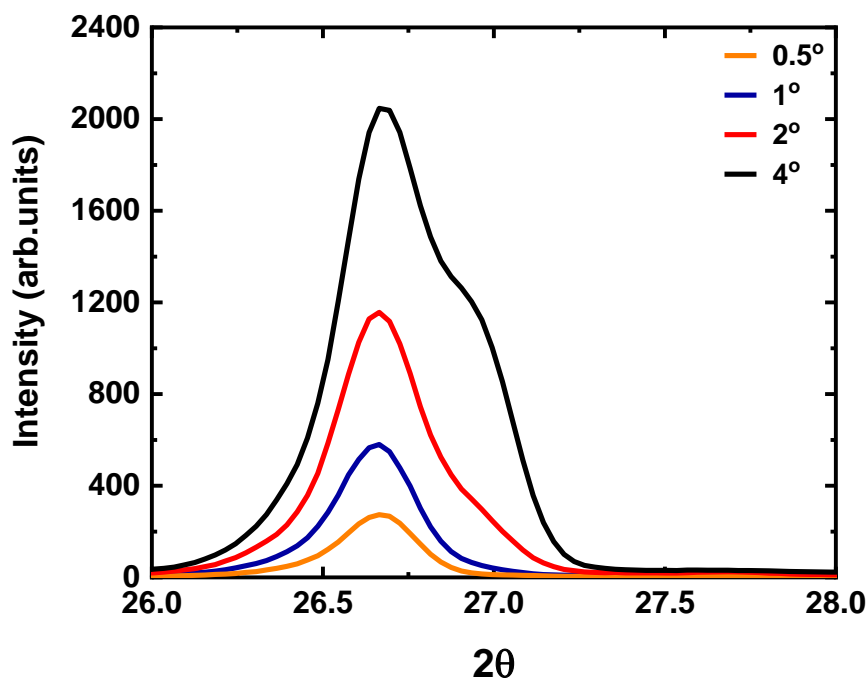


Figure 21. X-ray Diffraction plots of three key CIGS peaks (112), (204) and (312) for as-deposited and InCl_3 -annealed CIGS films at 500°C for 60 minutes.

TABLE 6. X-ray Diffraction and X-ray Fluorescence data measurements and analysis of as-deposited and InCl_3 -annealed samples at 500°C for 60 minutes.

	Parameters	As-deposited			InCl_3 -annealed		
		(112)	(220)/(204)	(312)	(112)	(220)/(204)	(312)
XRD	Peaks	(112)	(220)/(204)	(312)	(112)	(220)/(204)	(312)
	Angle (deg)	27.1	44.9	52.3	26.7/26.9	44.3/44.7	52.6/53.0
	Intensity (counts)	6220	1294	742	5175/1517	1584/611	812/362
	FWHM (deg)	0.25	0.38	0.45	0.18/0.14	0.20/0.31	0.37/0.18
XRF	Ga/III	0.42			0.14		

Structural and compositional analyses were done using XRD and XRF. Figure 21 shows the XRD plot of the as-deposited and recrystallized films at 500°C. The corresponding parameters are shown in Table 6. The XRD data for the films recrystallized at 500°C was comparatively similar to those at 450°C. The (220) and (312) peak intensity increased after InCl_3 recrystallization. The peak shifting and shoulder peak were observed in both cases, indicating the change in composition after the post-deposition treatment. The decrease in FWHM and increase in peak intensity suggest an increase in crystallite size, which was consistent with the SEM images. Glancing incidence x-ray diffraction (GIXRD) measurements were performed to understand further process of the films recrystallized at 500°C for 60 minutes. The GIXRD measurements plot shown in Figure 22 illustrates that the secondary phase starts to emerge for the angle between 1° and 2°. The surface phase aligns correctly with CIS, indicating the absence of Ga. Also, the second phase aligns well with Ga/III content of 0.14, which agrees with XRF.



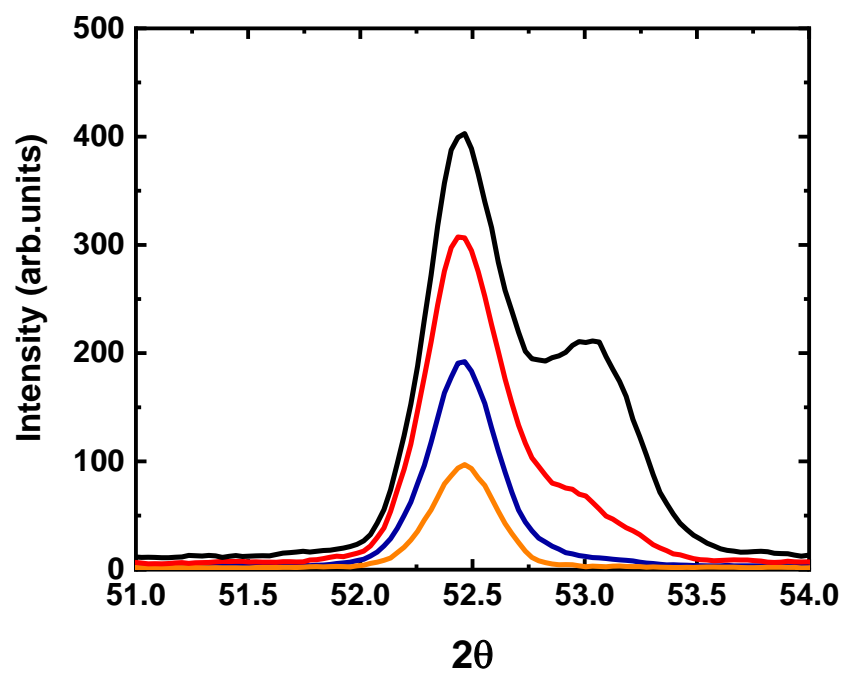
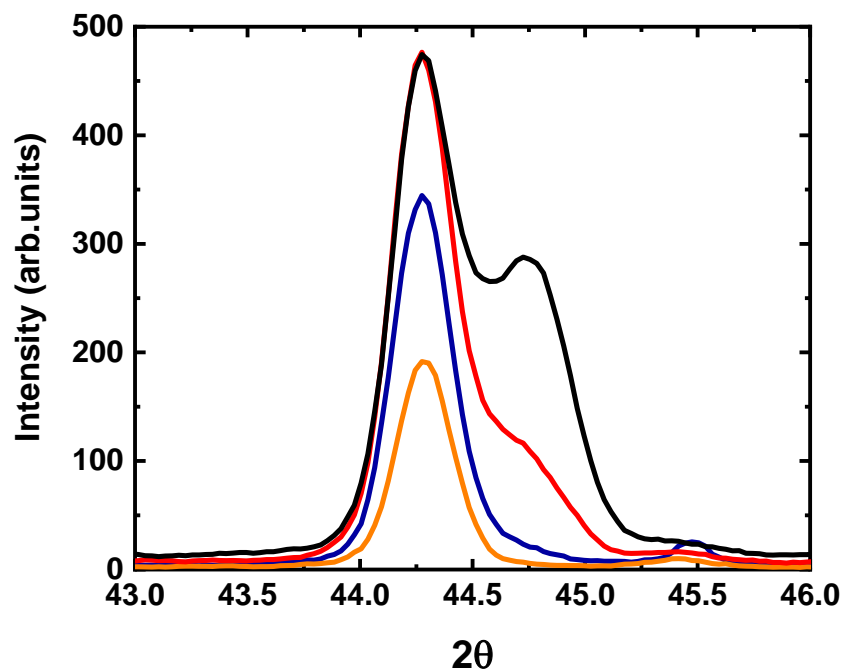
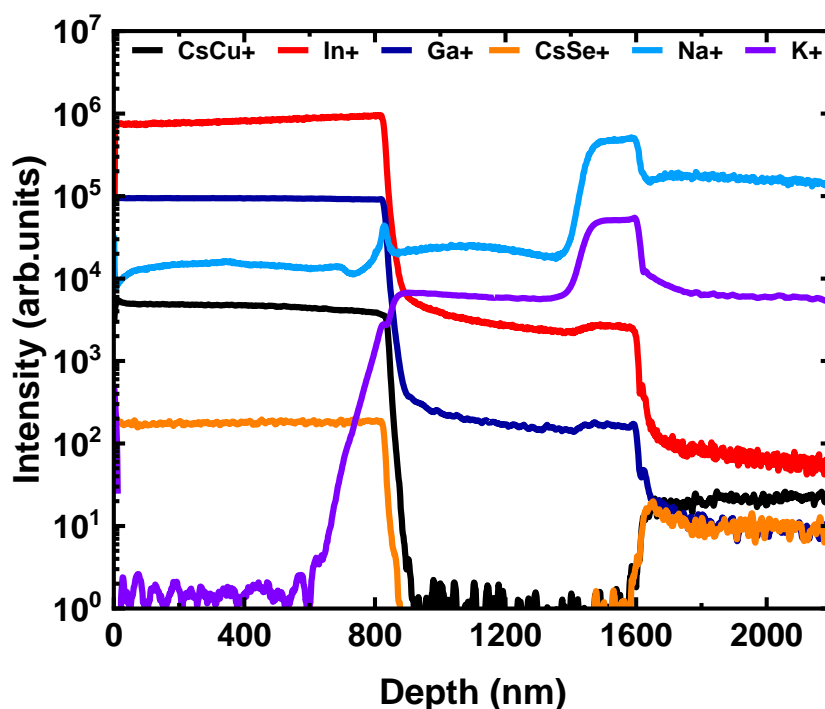


Figure 22. Grazing Incidence X-ray Diffraction plots of three key CIGS peaks (112), (220) and (312) at 0.5°, 1°, 2° and 4° of incidence for CIGS films recrystallized at 500°C for 60 minutes.

To further understand the post-deposition treatment process and phase separation, SIMS measurements were completed on as-deposited and recrystallized samples at 500°C. The positive ions spectra of the main elements for the as-deposited and recrystallized films are shown in Figure 23. The Cu, In, Ga, and Se profiles and alkali profiles Na and K were consistent with CIGS films deposited by a single-stage process on soda-lime glass. The profile of the constituent elements varies after the recrystallization. One of the main changes that occurred was that the intensity of Ga drops considerably near the surface. As stated earlier, the overall Ga/III ratio decreases from reference to annealed films according to XRD, which agrees with SIMS results even though the Ga profile stabilizes deeper into the film. Also, a decrease in the Cu to In ratio was noticed, indicating the transition from Cu-rich to Cu-poor films. This was also consistent with the XRF results. The K profile seemed to be follow the same trend as the Ga profile [123, 124], decreasing at the surface. Na was likely to have a higher concentration, as Na diffuses from glass through CIGS boundaries during the process [125].



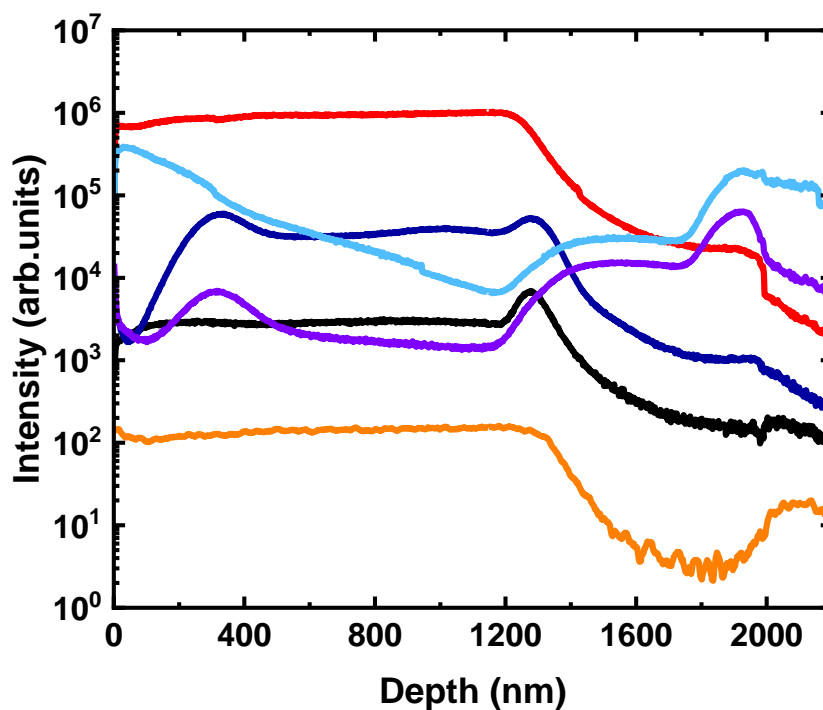


Figure 23. Secondary Ions Mass Spectrometry depth profile (positive ions) of the main elements for as-deposited and InCl_3 -annealed CIGS films at 500°C for 60 minutes.

The spatially-resolved SIMS profiles of these samples are shown in Figure 24. The analysis showed that the surface was poor, corresponding to a Ga-free CIS layer. This can be correlated with GIXRD, explaining the variation in the Ga/III with varying angles. The higher Ga layer below the CIS layer was found as the angle of incidence increases. This also explains why the Ga/III ratio in GIXRD was higher than observed by XRF measurements.

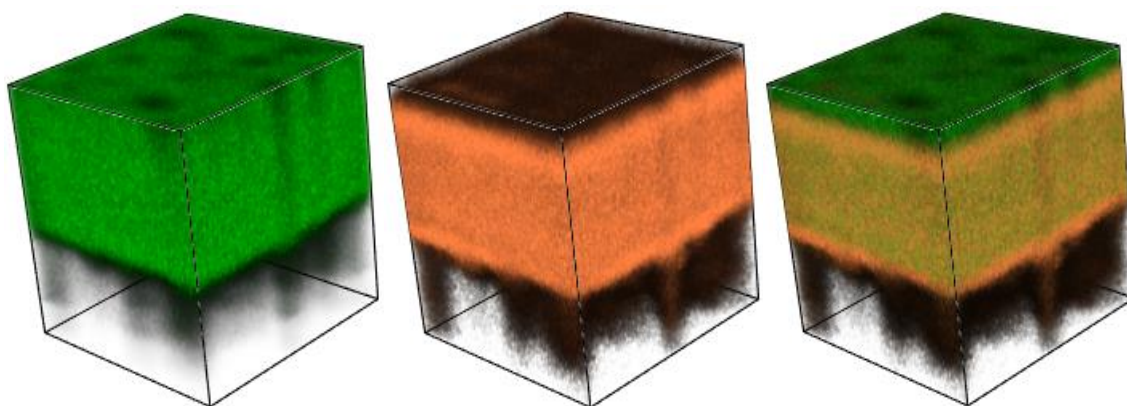


Figure 24. Spatial Resolution of secondary ion mass spectroscopy for CIGS films recrystallized in InCl_3 at 500°C for 60 minutes for Indium (left), Gallium (center) and Indium and Gallium (right) superimposed.

4.3.3 IMPACT OF COMPOSITION ON THE MICROSTRUCTURE

Based on the previous results, it appeared that InCl_3 changes the chemistry of the film. In this section, the impact of Ga/III and Cu/III ratios on the recrystallization process was examined. As a preliminary assumption, it is presumed that InCl_3 treatment probably add indium to the film; the process should therefore start with a Ga-rich film. To this end, CGS was deposited via a single-stage process at 350°C and then annealed at 500°C for 60 minutes with and without supplemental Se. SEM micrographs are shown in Figure 25.

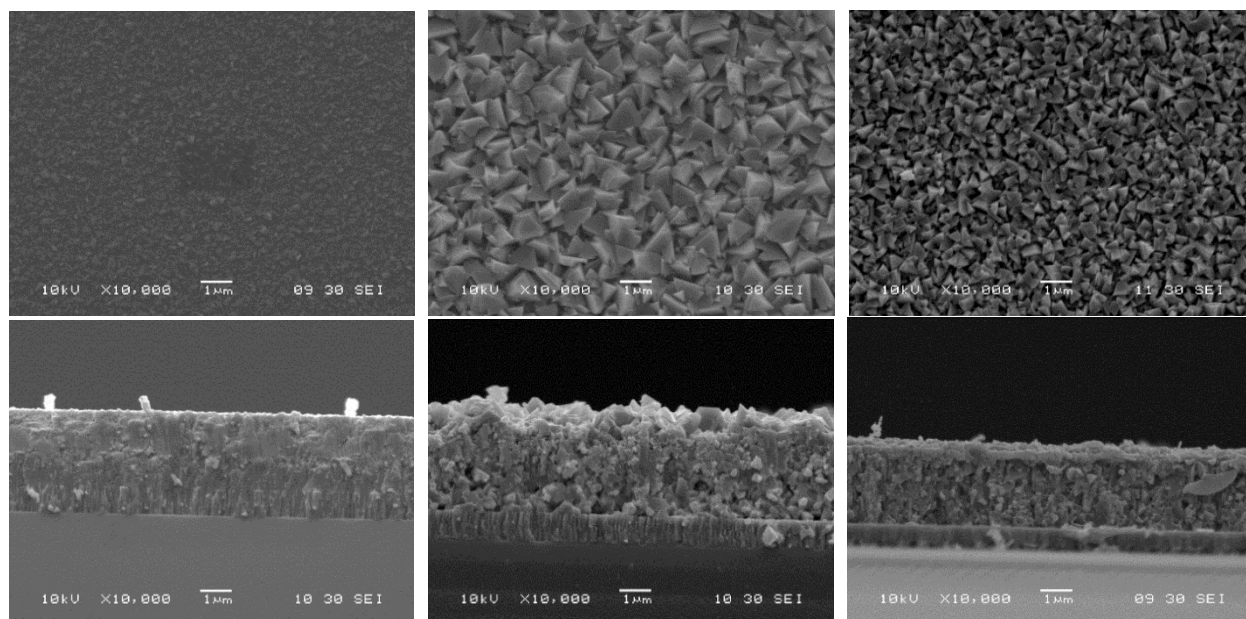


Figure 25. Scanning Electron Microscopy micrographs (surface and cross-section) of CGS films: as-deposited (left), recrystallized in InCl₃ (center) and recrystallized in InCl₃+Se at 500°C for 60 minutes.

A similar process was used for CIGS samples. The surface morphology of the as-deposited films resembles the CGS films, as demonstrated in Figure 26. The plain-view SEM images showed a significant change in the surface morphology, especially without Se. Unfortunately, the cross-sections showed that these changes do not occur across the film. From this, it is surmised that the InCl₃ forms large CIS grains on the surface, but the fluxing agent is either unable to diffuse or is not strong enough to affect the entire layer meaningfully. Because CGS did not undergo significant recrystallization, the next thing tried was a Ga/III ratio that aligned more closely to actual device stoichiometry: Ga/III = 0.3. When the Ga content was higher, the entire film structure undergoes meaningful changes.

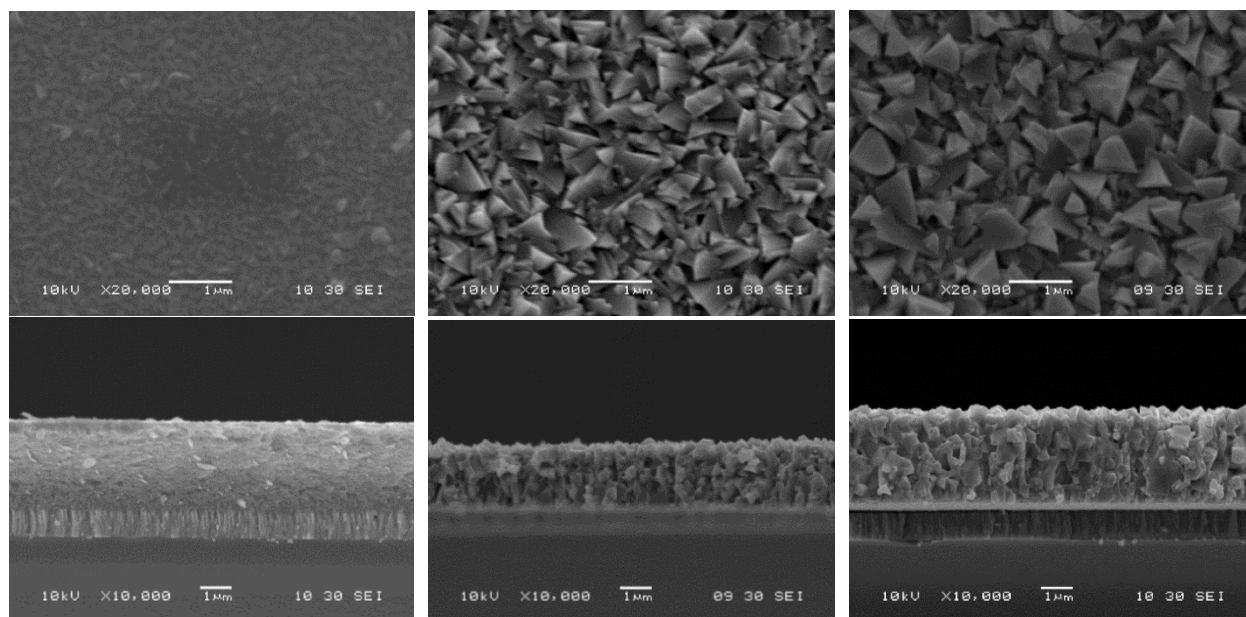


Figure 26. Scanning Electron Microscopy micrographs (surface and cross-section) of CIGS films: as-deposited (left), recrystallized in InCl_3 (center) and recrystallized in InCl_3+Se at 500°C for 60 minutes.

When looking at the transport phenomena within CIGS layers, high mobility of In and low mobility of Ga was observed. The presence of In within the film allows the grains to be more mobile. Looking at the InCl_3 anneal without Se, the decrease in layer thickness highlights the importance of Se overpressure during the annealing process. At elevated temperatures, Se can re-evaporate from the layer, causing a Se-deficient film. Since it is known that indium is key to recrystallizing with InCl_3 , the logical conclusion is to do a similar analysis with CIS films. As expected, the CIS films showed further improvement over the CIGS films, as shown in Figure 27. With CIS, significant change in microstructure were start to seen. From these initial tests, CIS demonstrated the most significant increase in grain size by far.

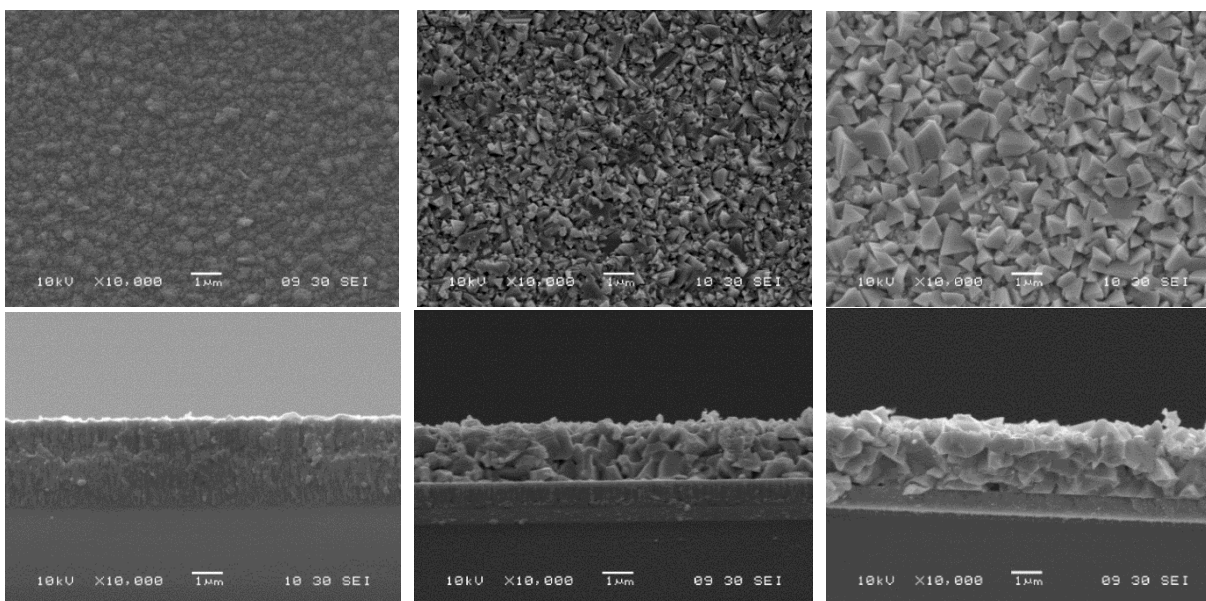


Figure 27. Scanning Electron Microscopy micrographs (surface and cross-section) of CIS films: as-deposited (left), recrystallized in InCl_3 (center) and recrystallized in InCl_3+Se at 500°C for 60 minutes.

As InCl_3 initiates the best recrystallization with CIS, further studies were done to determine the impact of time, temperature, and copper content on the recrystallization process. For this study, two times (30 and 60 minutes), two temperatures (450°C and 500°C), and two copper contents were tested. Both Cu-rich and Cu-poor CIS samples were examined at each of these temperatures and times. Copper content, much like indium content, was of extreme interest because, during the recrystallization process, indium from InCl_3 and Se could significantly change the film's stoichiometry. From preliminary XRF experiments, it was known that these annealing processes decreased the Cu concentration in the film compared to the other species. Because of this, initial Cu-rich films, that would become Cu-poor after annealing, were deposited. Cu-poor samples were also tested because Cu-poor CIGS films typically have higher efficiencies. The purpose of this experiment was to deposit a layer as fast as possible and then anneal it for the shortest amount of time at the lowest temperature possible while still reaching the highest efficiency. To that end, the first temperature analyzed was 450°C . This temperature is 100°C above initial single-stage

deposition, and from preliminary experiments, it was known that grain structure evolution at these temperatures would be observed.

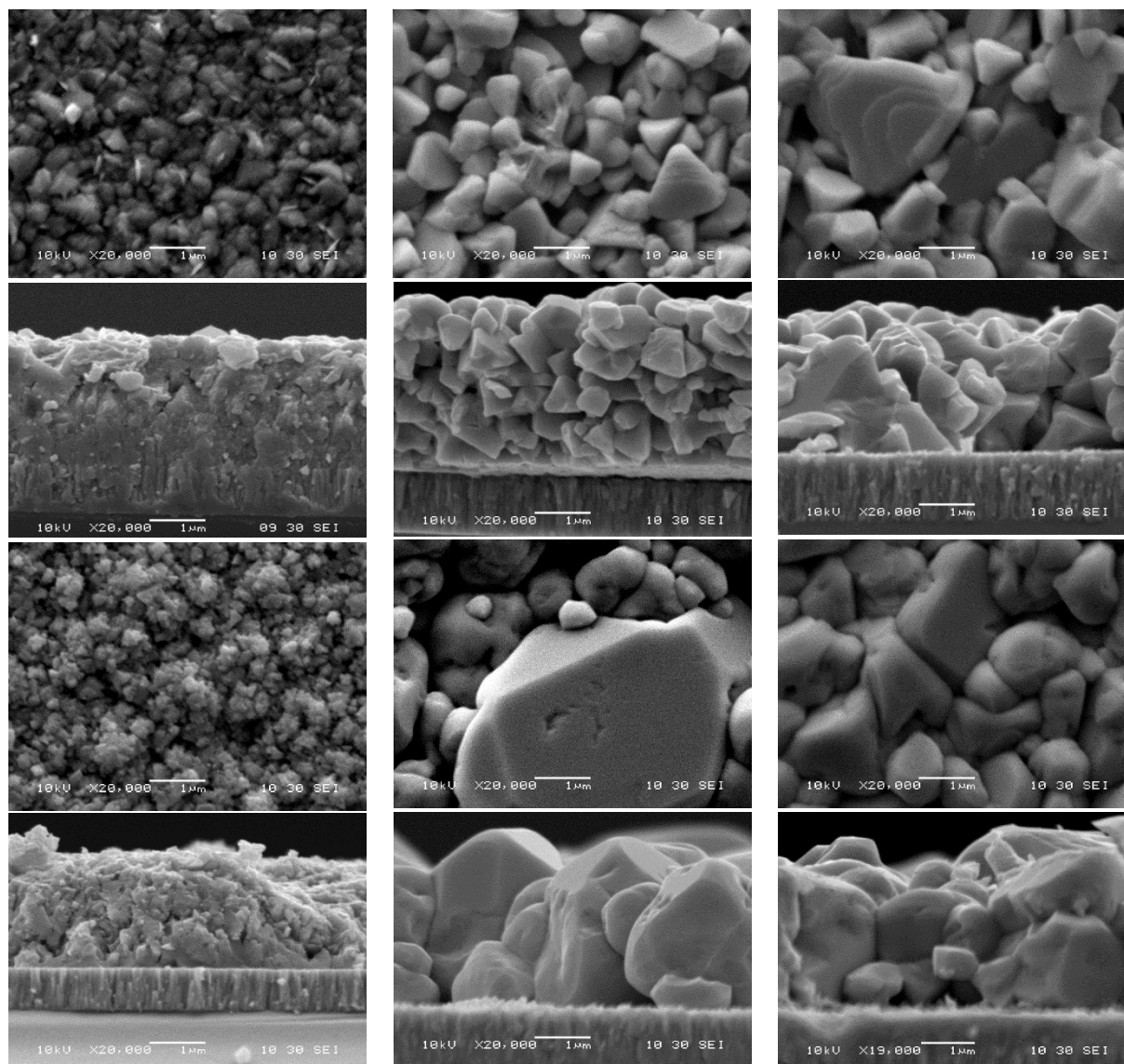
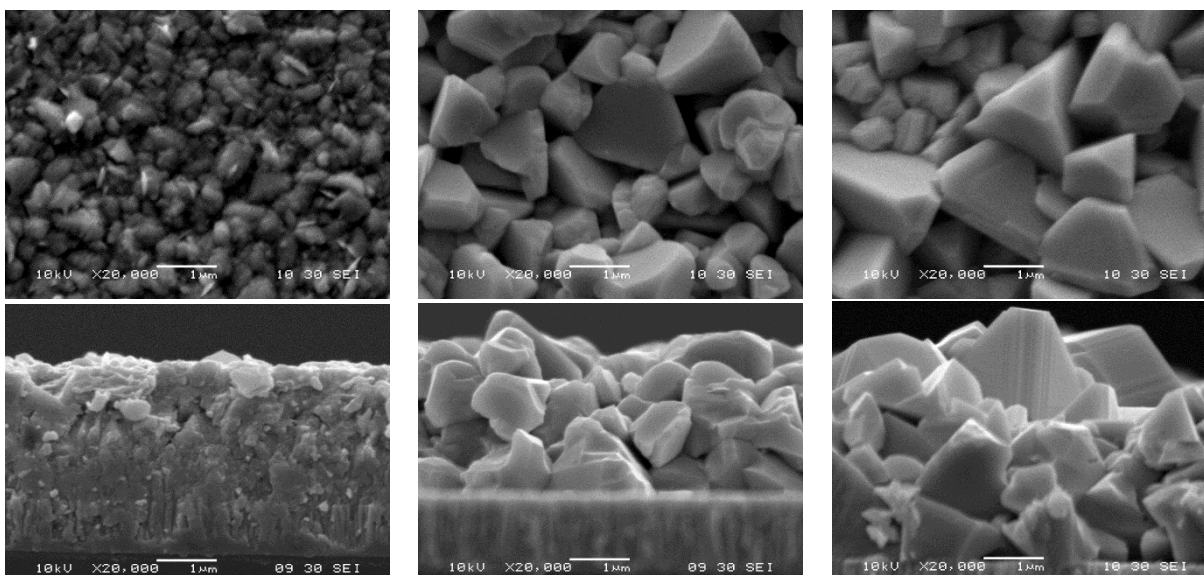


Figure 28. Scanning Electron Microscopy micrographs (surface and cross-section) of CIS films: as-deposited (left), recrystallized for 30 minutes (center) and 60 minutes (right) at 450°C by InCl_3 vapor treatment for Cu-poor (top two row) and Cu-rich (bottom two row) films.

A significant increase in the CIS films grain size during the annealing process was observed regardless of the time. The change of the surface and cross-section morphology of these films before and after recrystallization at 450°C are shown in Figure 28. The larger grains were formed for Cu-rich films. After 60 minutes, most of the small grains vanished and transform into larger ones. Also, after the 30 minute annealing process, the Cu-rich film looks to have the larger grain size, but the 60 minutes anneal appears more uniform. The initial hypothesis on copper content proved to be correct, with the Cu-rich films being the best. Now that significant recrystallization at 450°C was demonstrated, analyzing the process at 500°C to determine if the grain size is further improved was of great interest. The trends at 500°C mirror the trend at 450°C, as shown in Figure 29. However, the one key variation was that, in the 500°C processes, the CIS grains appear to reach the bottom of the film. Removing the small grains at the bottom is key to improving device quality because small grains near interfaces can cause serious carriers recombination issues. The grains were observed to be denser and uniform at a higher temperature. Overall, the Cu-rich tends to generate larger grains than Cu-poor, and the best grains were observed at a higher temperature.



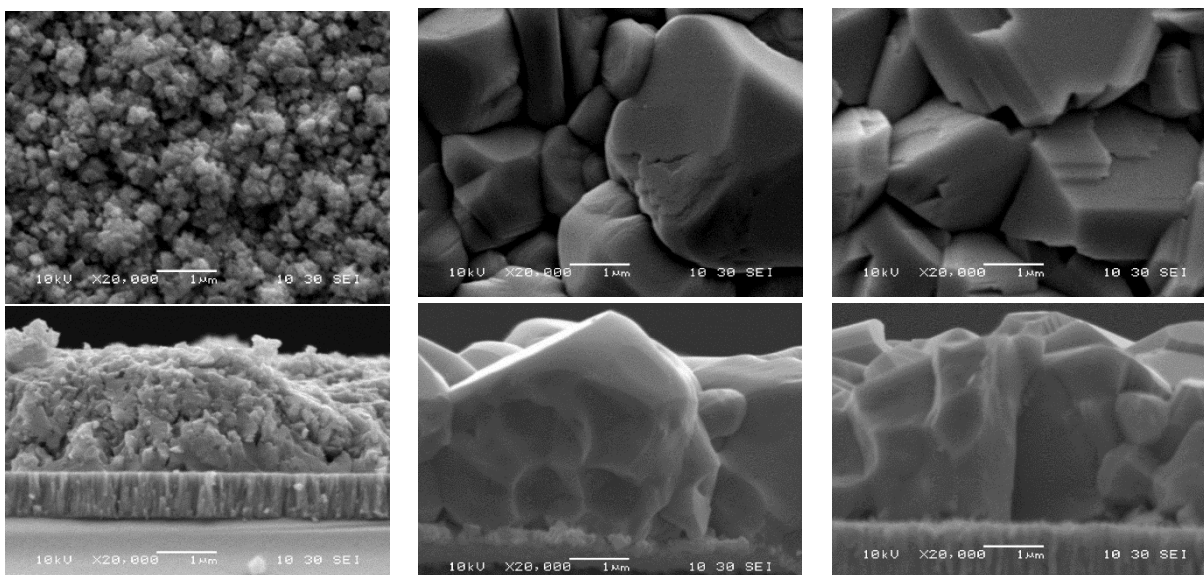


Figure 29. Scanning Electron Microscopy micrographs (surface and cross-section) of CIS films: as-deposited (left), recrystallized for 30 minutes (center) and 60 minutes (right) at 500°C by InCl_3 vapor treatment for Cu-poor (top two row) and Cu-rich (bottom two row) films.

4.4 SUMMARY

This section demonstrated that large crystals can be created through the recrystallization for CIGS semiconductors. The frequently used chemical vapor transport process allows for crystallites growth in a semiconductor. As exhibited by CdTe solar cells, the capability to execute post-deposition treatments on polycrystalline solar cells to improve their properties is essential for the potential industrial development of these technologies. In this chapter, a procedure built on a similar idea but replacing the group CdTe/ CdCl_2 with CIGS/metal halides (InBr_3 and InCl_3) was studied. SEM and XRD indicated a variation in grain size. The Hall effect measurements showed the changes in the electrical properties of the film after InBr_3 recrystallization.

Via the SIMS profiles, the significant changes in the Ga and Na profile were noticed with the change in the overall composition profile compared to the as-deposited samples of both InBr_3 and

Se-annealed samples. An optimum Na concentration in CIGS is suitable for device performance, whereas the Ga concentration change might produce a very poor device. Based on these initial results better control process will therefore be required to improve the device performance. Some potential solutions might be the change of temperature, the dose of InBr_3 , or depositing Ga with a higher Ga concentration at the front. It is not likely one can get high efficiency devices without the modification of the Ga and Na profiles. Similarly, the changes in the structural properties of the CIGS film were observed by SEM and XRD with InCl_3 treatment. The variation of Ga within the annealed films was not optimal. The InCl_3 post-deposition treatment induces depletion of Ga at the surface with significant grain recrystallization. The films become more indium rich, whereas most of the element profile remains flat through the films. The K profile follows the Ga profile, while the Na profile did not follow it. Also, the change in composition, particularly Ga content showed that, the CIS demonstrate the significant change in microstructure with better increase in grain size as compared to CGS and CIGS. Overall, it may be possible to recrystallize the deposited sample with ideal composition by more precise timing and different fluxing agent to get high performance devices.

CHAPTER 5

IN-SITU RECRYSTALLIZATION OF CIGS THIN FILMS-I

CIGS thin film solar cells have been intensively investigated over the past two decades due to the advantages of high-power conversion efficiency, potentially low-cost, tolerance to the wide variation of elemental composition, and durability. High efficiency CIGS solar cells are generally fabricated using a three-stage process via a vacuum-based method that can accurately control the composition and vary the bandgap gradients within the absorber layers. Among the many factors during the fabrication of CIGS thin films, the substrate temperature plays a significant role in the quality of the absorber layer. The thermal co-evaporation requires high energy input, as the process requires a high substrate temperature over 500°C during the deposition close to the softening temperature of soda-lime glass. The high temperature could lead to the loss of elements when the materials are deposited on the substrate [126-128]. The advancement in the fabrication process with the best possible economic viability and increasing the deposition rate at low temperature while maintaining high efficiency, is a current need for thin film solar cells [42]. The lower substrate temperature is appropriate for multiple substrate choice, lowered energy cost of fabrication, and lead to a CIGS-based tandem cell application. In addition, a lower temperature can allow faster heat up and cool down time, decrease the heat load and thermal stress on the entire deposition system. This could provide the path for producing flexible CIGS solar cells on polymer substrate suitable for continuous and roll to roll deposition process and ultimately reduce the manufacturing cost. However, the decrease in substrate temperature is linked to a decreased in solar cell performance and smaller grain sizes compared to the films deposited at higher temperatures [129, 130]. The potential of the three-stage process seems uncertain at a low temperature since the CIGS films have to undergo phase transformations, which require the interdiffusion of the constituent atoms facilitated by thermal energy from the substrates [131]. However, the fabrication of CIGS films at low temperatures has been studied in previous years, but significant conclusion has not been made from the results [132-134].

5.1 EXPERIMENTAL DETAILS

The CIGS devices were fabricated with a standard SLG/Mo/CIGS/CdS/i-ZnO/ITO/Grads structure. The i-ZnO/ITO was used as transparent conducting oxides, CdS as the buffer layer, CIGS as the absorber layer, molybdenum as a back contact, and soda-lime glass as the substrate for all samples. A molybdenum bilayer was first deposited on the SLG substrate at a power density of 7.4 W/cm^2 . The absorber layer CIGS was then deposited by a three-stage co-evaporation process from independently controlled elemental sources of Cu, In, Ga and Se. The balance between incoming heat flow from the heater and outgoing radiation from the film determines the temperature of the growing film. The incoming heat flow is nearly constant under constant heating power. Therefore, the substrate temperature was determined from the radiative loss from the film. The process was performed with high deposition rates of about $10 \text{ }\mu\text{m/hr}$ with low substrate temperature for the second and third-stages. First, In, Ga and Se were evaporated during the first-stage. In the second-stage, evaporation of Cu and Se was performed and finally followed by the evaporation of In, Ga, and Se again until the films become Cu-poor ($[\text{Cu}]/[\text{In}+\text{Ga}] < 1$) [96, 135]. Recrystallization was performed between the second and third-stages by evaporating the metal halides in a short period. The CdS layer of thickness 80 nm was deposited using chemical bath deposition to form a junction with the CIGS layer. Afterward, the transparent conducting oxides consisting of i-ZnO/ITO with a thickness of about 80 nm and 250 nm respectively was deposited by rf sputtering. The e-beam evaporation was used to deposit the metal contacts of Ni/Al/Ni. Finally, the solar cells were defined by mechanical scribing with an active area of 0.5 cm^2 .

The film composition was evaluated by x-ray fluorescence (XRF). Surface and cross-section morphological analyses were performed by scanning electron microscopy. The crystallographic structure analysis was done by symmetric θ - 2θ x-ray diffraction (XRD) and analyzed using ICDD database. Depth profiles of the films were measured by a time-of-flight secondary ion mass spectrometry (TOF-SIMS) instrument. The photovoltaic characteristics of the devices were evaluated by current density-voltage (J-V) measurements under AM 1.5G with a light intensity of 100 mW/cm^2 at 25°C and by external quantum efficiency (EQE) measurements.

5.2 RECRYSTALLIZATION BY COPPER CHLORIDE TREATMENT

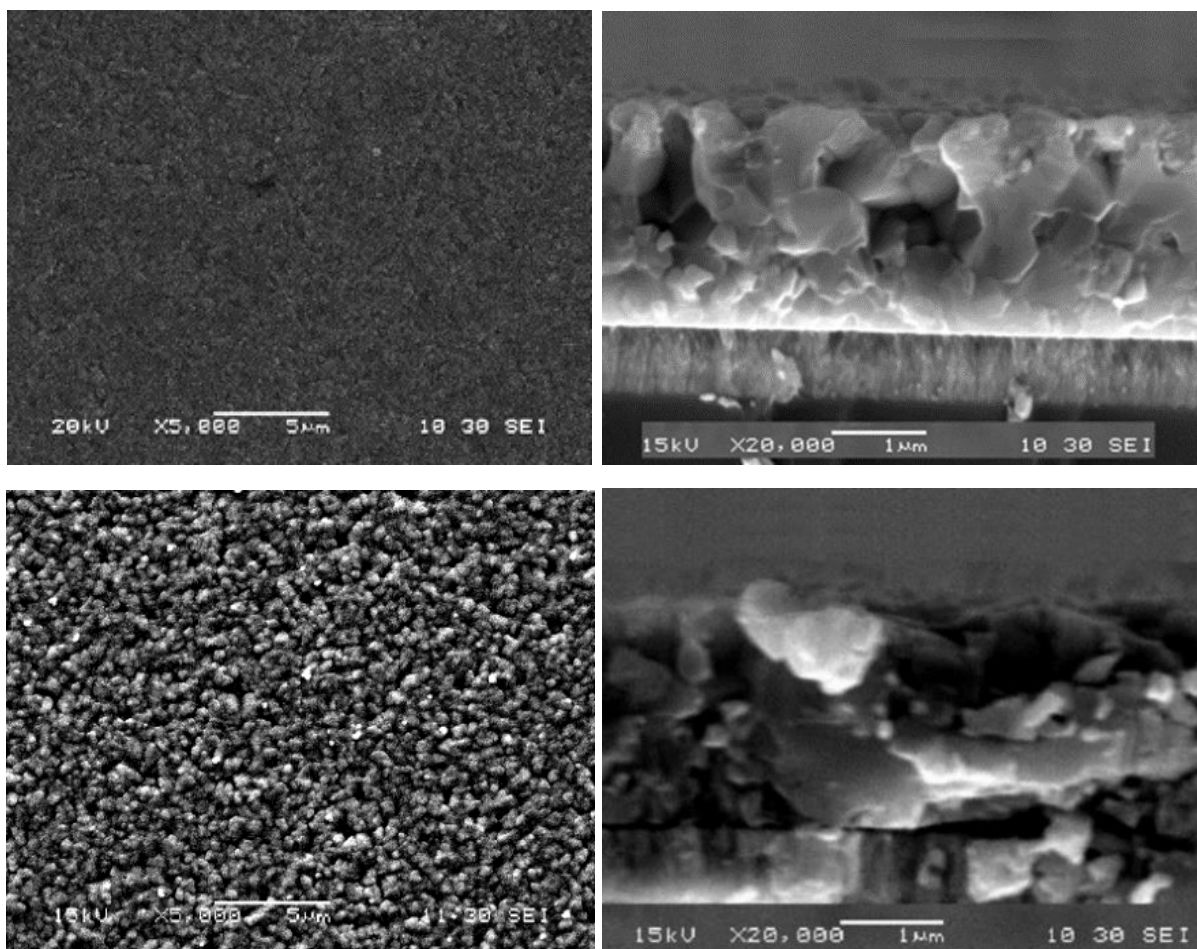
The three-stage deposition process of CIGS uses very high temperatures, up to 550°C, for a good quality device. Due to high processing temperature and slow deposition rate, CIGS solar cells are not as competitive as their counterpart's crystalline silicon technology. The focus of this experiment is increasing the deposition rate with simultaneously decreasing the deposition temperature, while keeping the high efficiency. In this section, CIGS films deposited at 350°C were recrystallized in-situ with CuCl₂ vapor treatment at different temperatures in the second and third-stages. The recrystallization was performed in the middle of the second and third-stages by flashing 20 mg of CuCl₂ in 1 minute. No further post-deposition treatment of any alkali halides, such as sodium fluoride and potassium fluoride, was performed. The films were evaluated for composition and morphological changes. In this chapter, samples were also generated independently for reference without CuCl₂ treatment and are termed "reference" samples. The other half were referred to as recrystallized samples. The substrate temperature for the second and third-stages was changed during the process, as shown in Table 7. The overall experiment and subsequent results were presented as the second-stage temperature dependence and third-stage temperature dependence, which are discussed in the following section.

TABLE 7. Substrate temperature for the different stages of the CIGS runs.

Samples	1 st -Stage T _{SS} (°C)	2 nd -Stage T _{SS} (°C)	3 rd -Stage T _{SS} (°C)
Reference Sample	350	400	450
2 nd -Stage Low Temperature (LT)	350	350	400
2 nd -Stage High Temperature (HT)	350	400	400
3 rd -Stage Low Temperature (LT)	350	400	425
3 rd -Stage High Temperature (HT)	350	400	450

5.2.1 SECOND-STAGE TEMPERATURE DEPENDENCE

Two distinct sets of runs were done with a change in substrate temperature of the second-stage. The first set of samples was deposited at 350°C, referred to as second-stage low temperature, whereas another set was deposited at 400°C, referred to as second-stage high temperature. The temperature of the first and third-stages was kept constant at 350°C and 400°C, respectively. As previously mentioned, the samples were recrystallized by flashing 20 mg of CuCl_2 . Figure 30 shows the change in the surface and cross-section of the films before and after recrystallization, as observed by SEM. At both temperatures, a clear change in the grain size was observed. The small grains in the reference samples were transformed into larger grains after recrystallization. The films recrystallized at 350°C seemed to be less dense, whereas the films recrystallized at 400°C seemed to be more compact, distinct, and uniform.



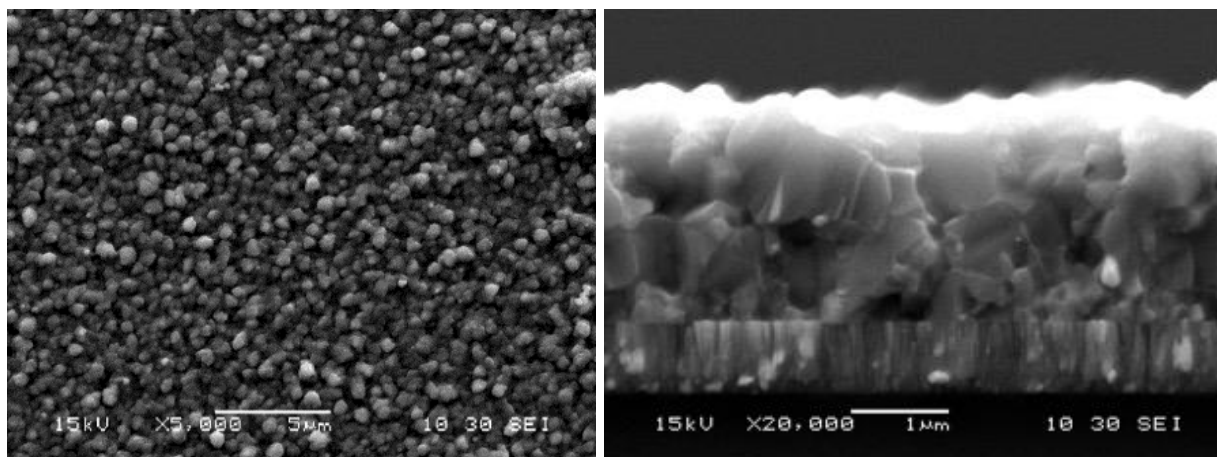
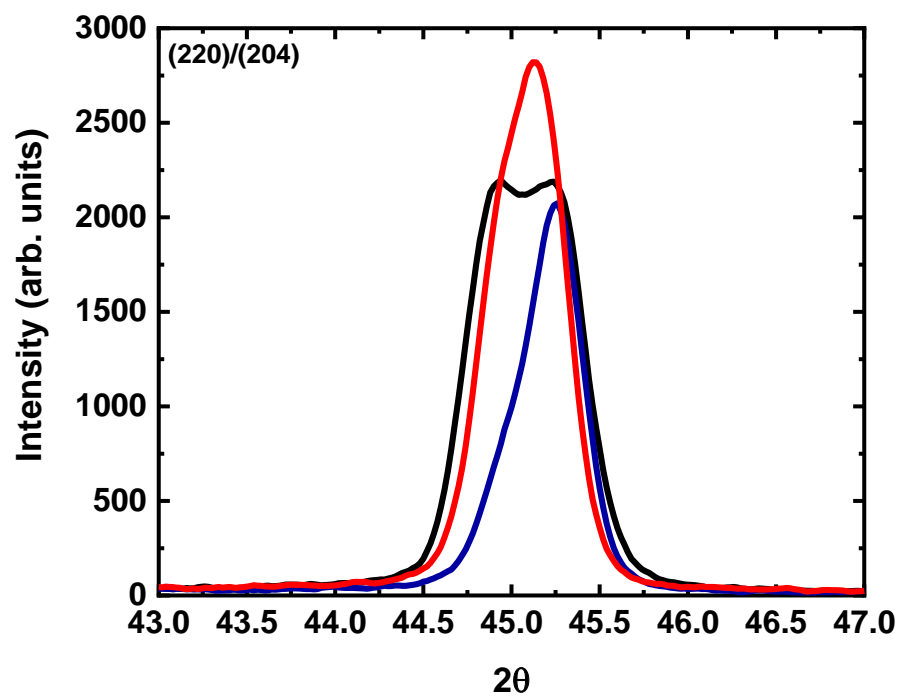
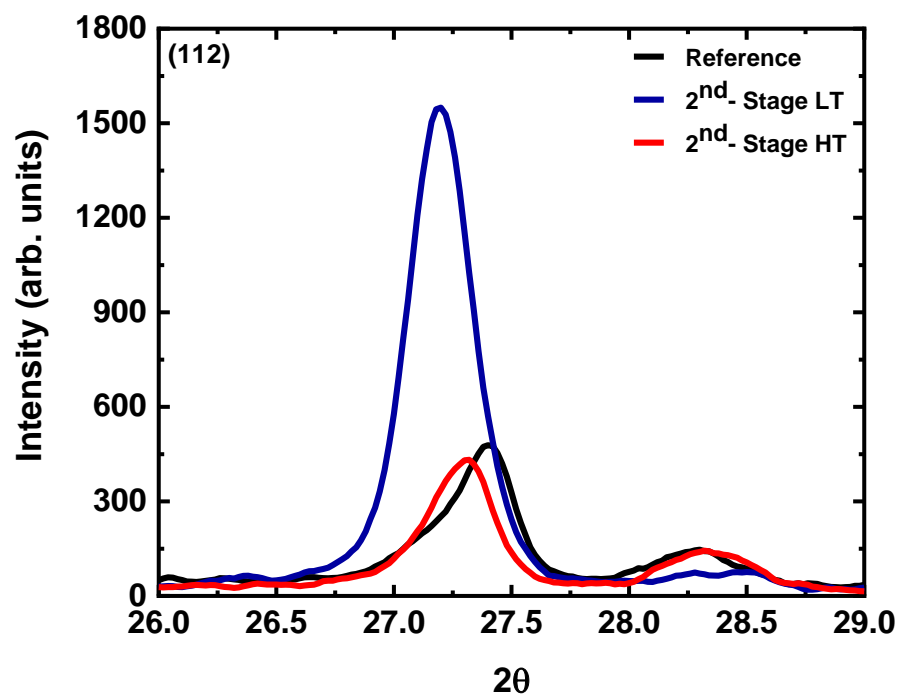


Figure 30. Scanning Electron Microscopy micrographs (surface and cross-section) of CIGS films: reference (top), 2nd-stage LT (center) and 2nd-stage HT (bottom) recrystallized in CuCl_2 environment.

As seen from the SEM, the structure of the films changed with the treatment. To further analyze the structural properties, XRD measurements were performed on the reference and recrystallized films (Figure 31). Table 8 shows the corresponding parameters extracted from the measurement. The XRD peaks exhibited the different preferential orientations for both films. The (112) peak intensity was higher in the case of 350°C samples, whereas the intensity of the (220)/(204) peak was higher in the case of 400°C samples. However, there was an increase in the film crystallinity, as seen by a decrease in full width at half maxima (FWHM) and an increase in peak intensity for both recrystallized samples. Besides these, a shift in the peak position was also observed. The (112) peak moves in the direction of the lower angle, implying a lower Ga content, while the (220)/(204) peak moves in the direction of the higher angle. This overall change implies that there was a redistribution of Ga. The XRF measurements confirmed the results as the Cu/III, and Ga/III ratio barely changed from one film to another. In the case of 400°C, the peak shift to a higher angle for the (112) peak, while it remains the same for the (220)/(204) peak. The FWHM decreases in both cases.



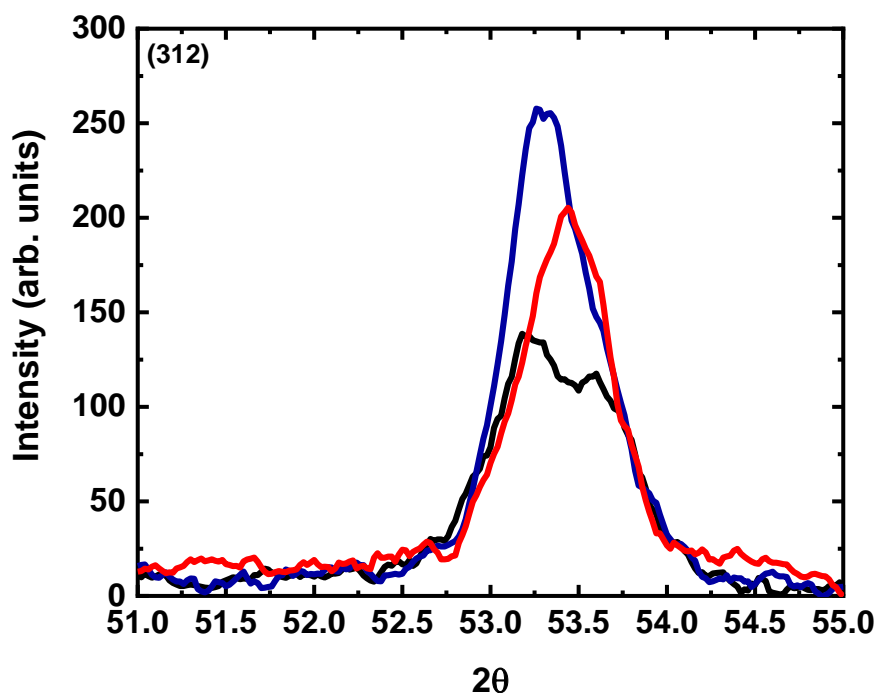
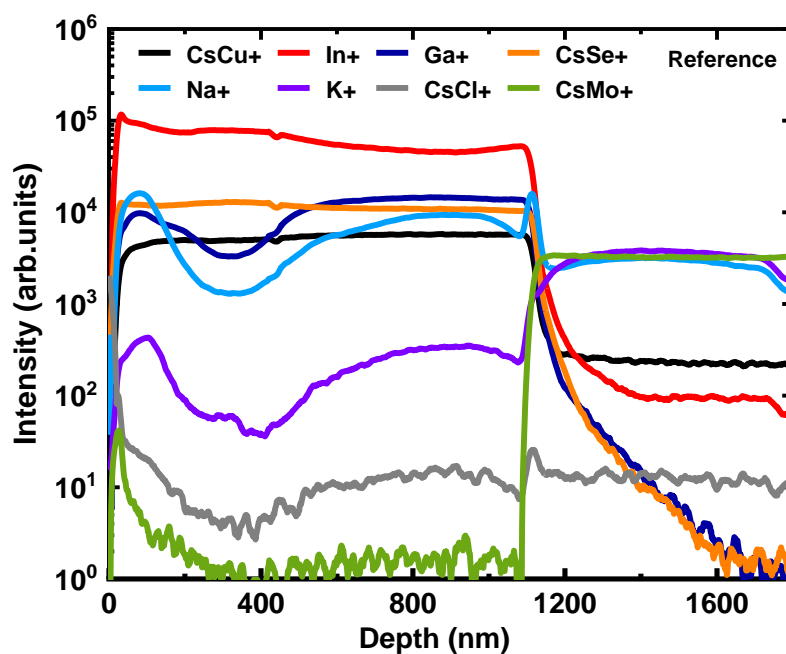


Figure 31. X-ray Diffraction plots of three key CIGS peaks (112), (204) and (312) for the reference (black), 2nd-stage LT (blue) and 2nd-stage HT (red) CIGS films recrystallized in CuCl₂ environment.

TABLE 8. X-ray Diffraction and X-ray Fluorescence results of the reference, 2nd-stage LT and 2nd-stage HT CIGS samples.

Parameters	Reference			2 nd -Stage LT			2 nd -Stage HT		
	(112)	(204)	(312)	(112)	(204)	(312)	(112)	(204)	(312)
Angles (deg)	27.4	44.8/45.3	53.3	27.1	45.2	53.5	27.3	44.9/45.1	53.4
FWHM (deg)	0.32	0.30/0.56	0.82	0.30	0.41	0.58	0.30	0.25/0.44	0.54
Intensity (counts)	472	2239/2230	137	1569	2115	266	446	1845/2771	216
Crystallite size (nm)	26.7	29.9/16.0	11.3	28.4	21.9	16.0	28.4	35.9/20.4	17.2
Cu/III	0.89			0.88			0.88		
Ga/III	0.34			0.33			0.32		

SIMS depth profile measurements were used to investigate the samples, with the matrix element of each layer being characterized. The depth profiles for the positive ions of the main elements are shown in Figure 32. SIMS was employed to understand the recrystallization process and to determine whether there was a redistribution of elements within the film. The alkali profile and positive ions of the main elements of the reference sample were coherent with CIGS film deposited by a three-stage process. The Cu, In, and Se profiles remain the same after the annealing. The chlorine does not remain in the film, as no significant signal was noticed despite improving the grains. CIGS films deposited by a three-stage process typically exhibit a Ga notch, as observed in the reference sample. The Ga notch decreases after introducing CuCl_2 in the second-stage low temperature, whereas it almost vanishes for the second-stage high temperature. This showed the interdiffusion of Ga due to the treatment, with a higher rate at a higher temperature. Similarly, as compared to reference, the Na profile decreased after recrystallization while the K profile remains almost the same. A possible explanation is that, due to the increase in grain size, the grain boundary density changes, which lessens the paths for Na to diffuse through the films [50] and ultimately causes the decrease of Na profile after the treatment.



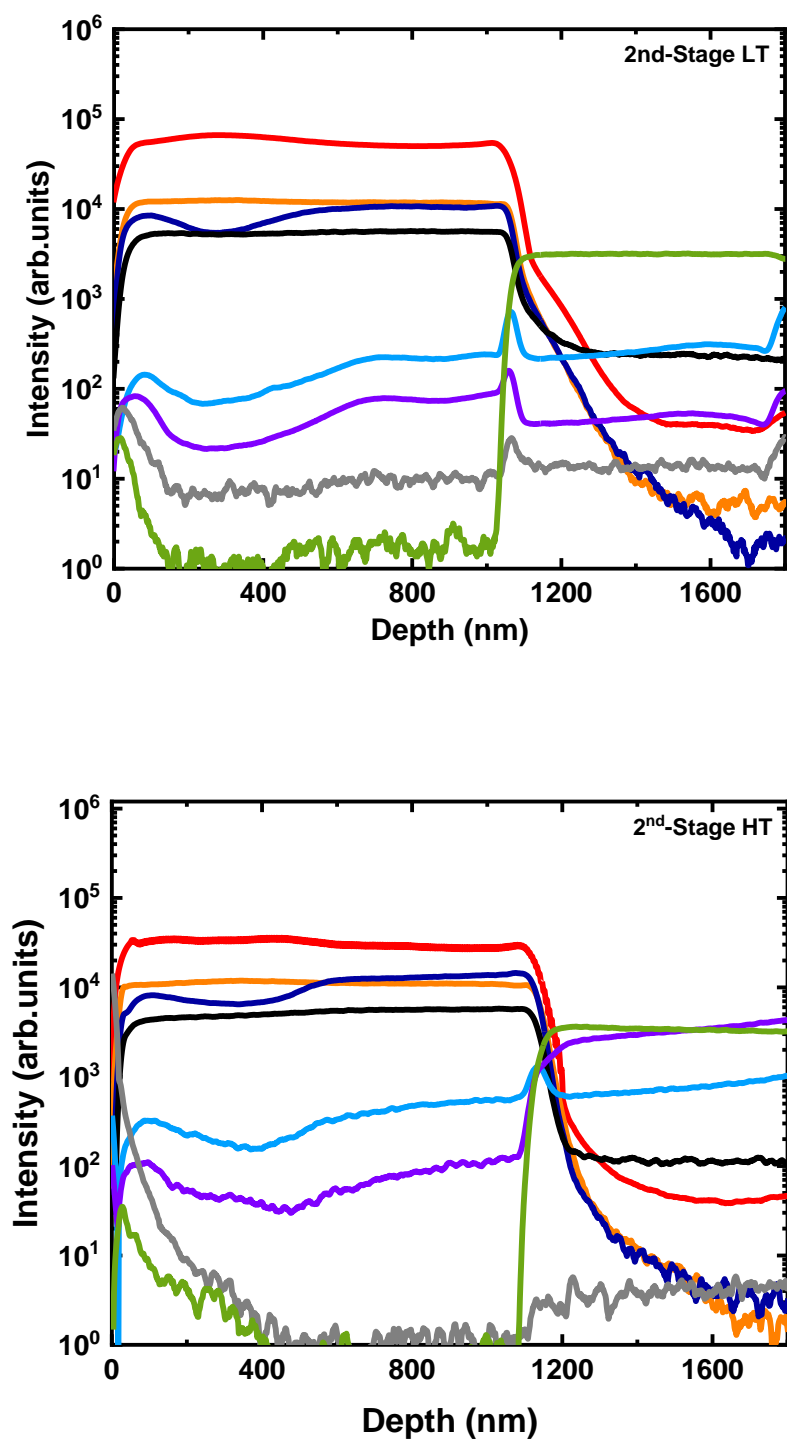
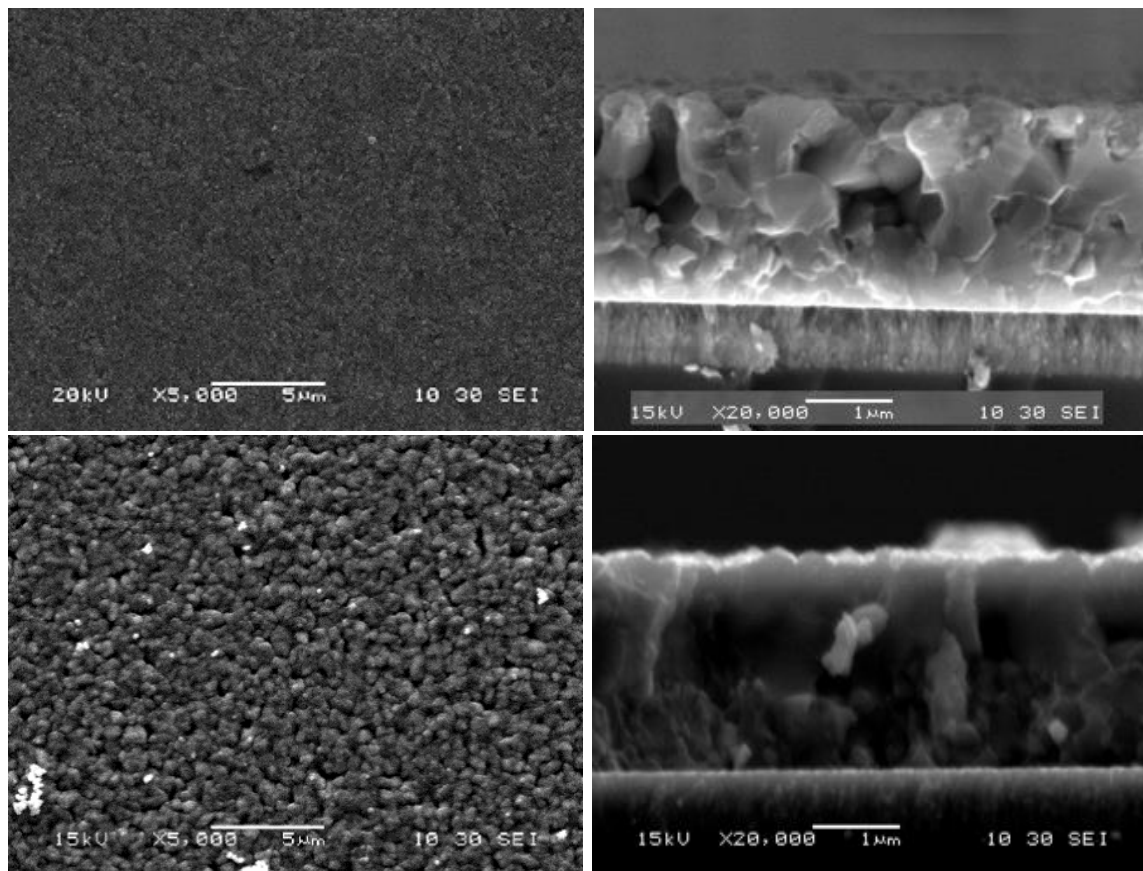


Figure 32. Secondary Ions Mass Spectroscopy depth profile (positive ions) of the main elements for the reference (top), 2nd-stage LT (center) and 2nd-stage HT (bottom) CuCl₂-treated CIGS films.

5.2.2 THIRD-STAGE TEMPERATURE DEPENDENCE

Another two different sets of runs were done with a change in substrate temperature of the third-stage. The first set of samples was fabricated with a third-stage at 425°C, termed third-stage low temperature, whereas another set was deposited with a third-stage at 450°C, termed third-stage high temperature. The temperature of the first and second-stages was kept constant at 350°C and 400°C, respectively. The process of in-situ treatment was the same as in section 5.2.1, with 20 mg of CuCl_2 flashed in 1 minute in between the second and third-stages. Figure 33 shows the surface and cross-section SEM images before and after the recrystallization.



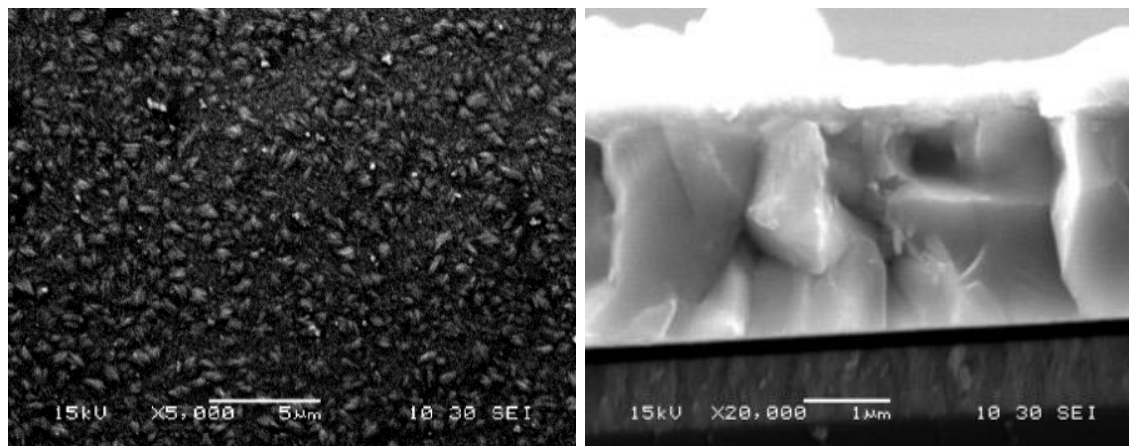
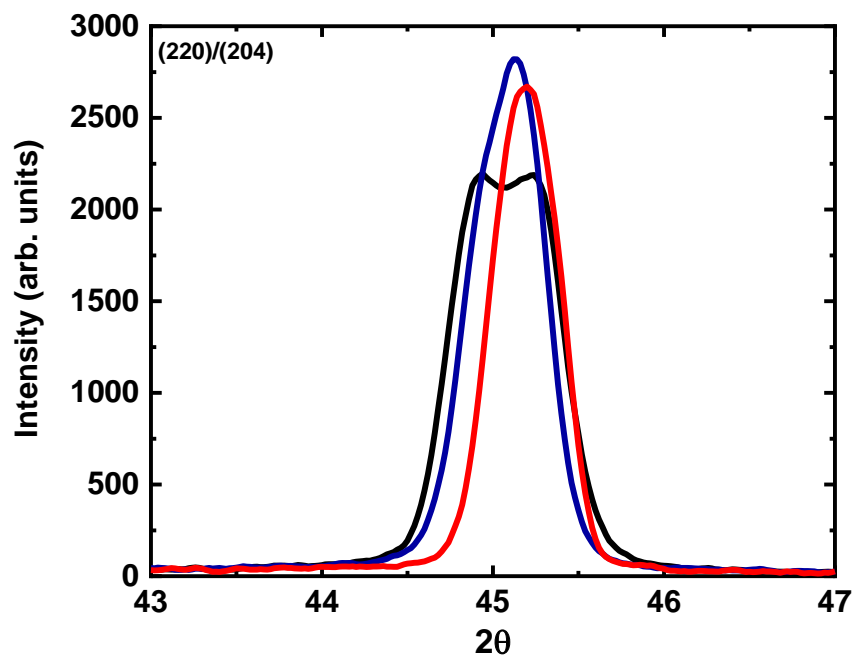
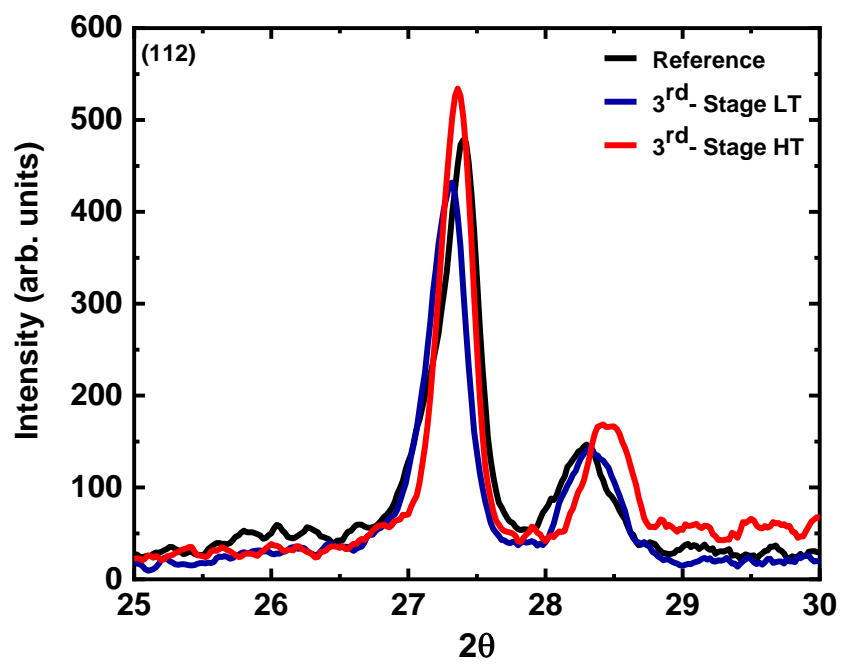


Figure 33. Scanning Electron Microscopy micrographs (surface and cross-section) of CIGS films: reference (top), 3rd-stage LT (center) and 3rd-stage HT (bottom) recrystallized in CuCl₂ environment.

The increase in grain size was observed clearly as small grains transform into a large one. A slight change in microstructure was observed in the case of 425°C, while drastic transformation was seen at 450°C as grain growth was significant, with grains in the order of a micrometer. Also, SEM for the second-stage high temperature (Figure 32) showed a similar grain size transformation as the one observed in the case of third-stage high temperature. This indicates that recrystallization seemed to be enhanced at higher temperature. XRD measurements were performed on reference and recrystallized samples to understand the crystallinity of the films. The parameters extracted from the XRD are shown in Table 9. The XRD peaks showed the different preferential orientations for both films, as shown in Figure 34. The (112) peak intensity was higher in 450°C samples whereas it was lower in the case of 425°C. The intensity of the (220)/(204) and (312) peaks was high in both cases. The FWHM decreases in every peak, indicating the increase in the crystallinity after the treatment. Also, the crystallite size calculated by Scherrer's formula suggests the increase in the grain size, as shown in Table 9. The two peaks that can be noticed for the reference sample were convoluted for the third-stage low temperature, indicating a transformation in composition or redistribution of the Ga all over the films. The film composition was not changing, as determined by the XRF measurement.



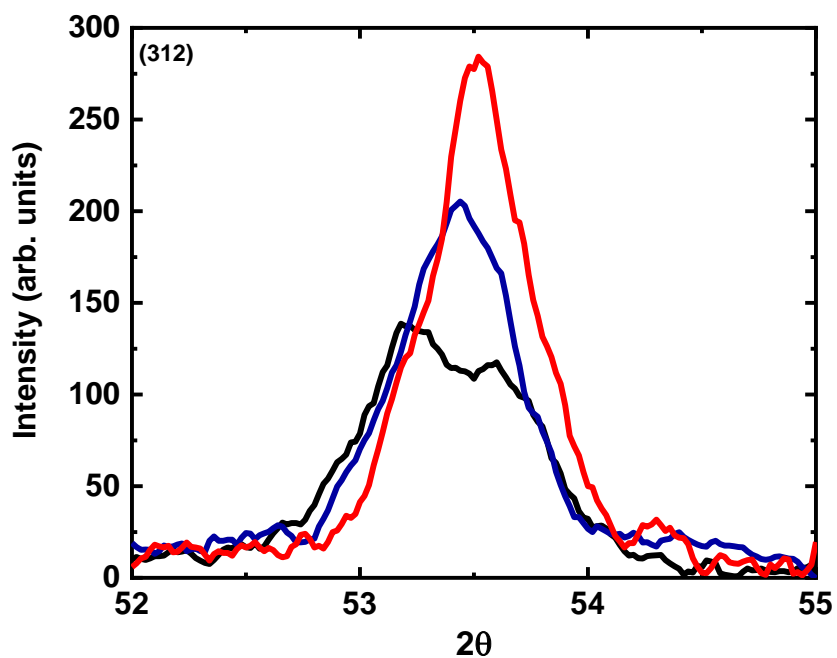
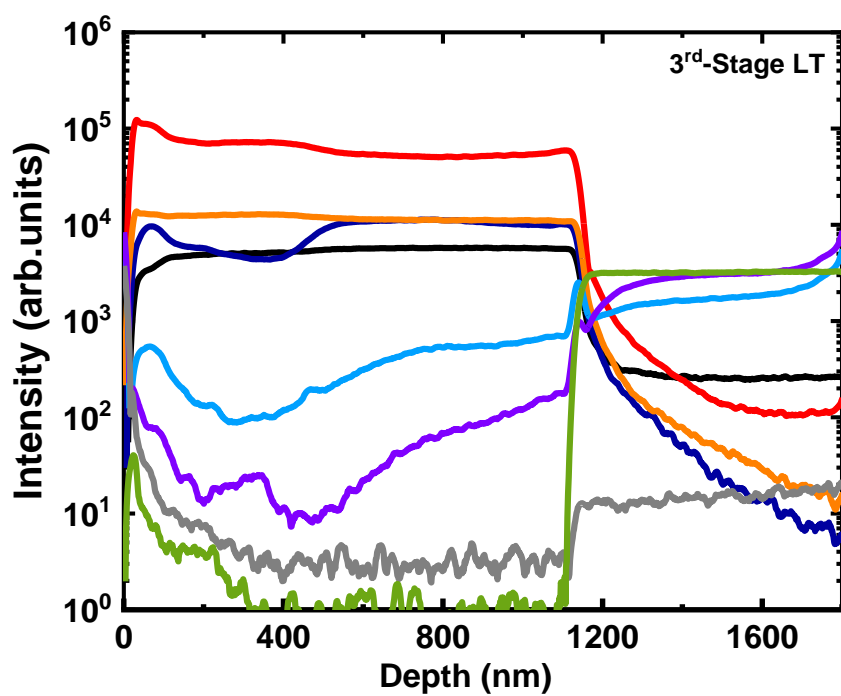
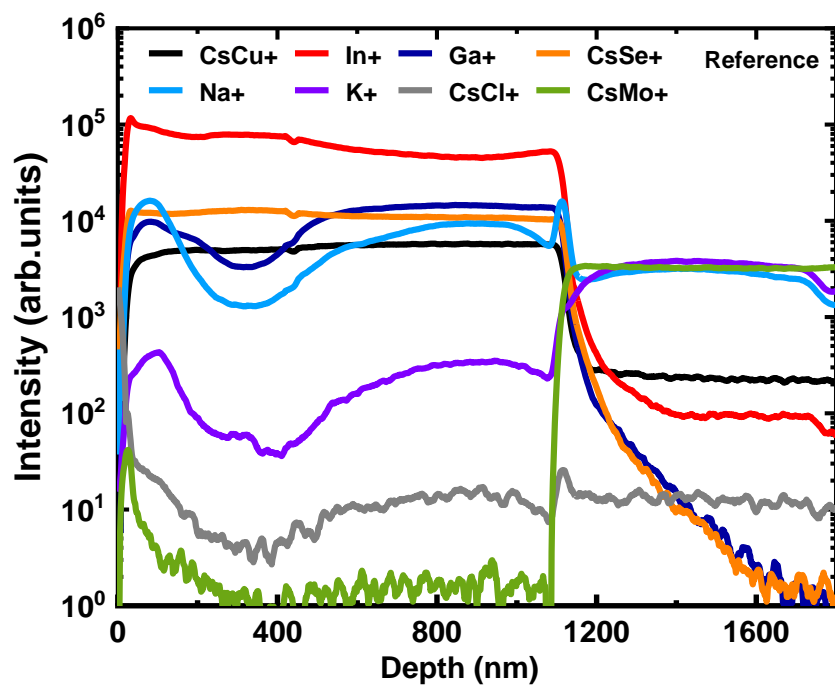


Figure 34. X-ray Diffraction plots of three key CIGS peaks (112), (204) and (312) for the reference (black), 3rd-stage LT (blue) and 3rd-stage HT (red) CIGS films recrystallized in CuCl₂ environment.

TABLE 9. X-ray Diffraction and X-ray Fluorescence results of the reference, 3rd-stage LT and 3rd-stage HT CIGS samples.

Parameters	Reference			3 rd -Stage LT			3 rd -Stage HT		
	(112)	(204)	(312)	(112)	(204)	(312)	(112)	(204)	(312)
Angles (deg)	27.4	44.8/45.3	53.3	27.3	44.8/45.2	53.4	27.4	45.1	53.5
FWHM (deg)	0.32	0.30/0.56	0.82	0.29	0.24/0.45	0.55	0.25	0.40	0.53
Intensity (counts)	472	2239/2230	137	424	1795/2770	202	537	2624	286
Crystallite Size (nm)	26.7	29.9/16.0	11.3	29.4	37.4/20.0	16.9	34.1	22.4	17.5
Cu/III	0.89			0.88			0.89		
Ga/III	0.34			0.33			0.34		



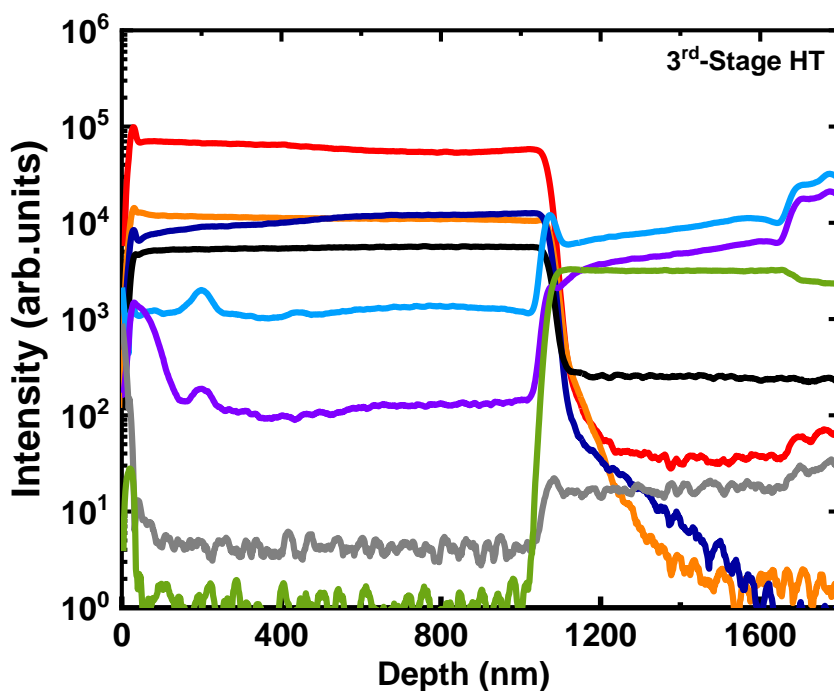


Figure 35. Secondary Ions Mass Spectroscopy depth profile (positive ions) of the main elements for the reference (top), 3rd-stage LT (center) and 3rd-stage HT (bottom) CuCl₂-treated CIGS films.

SIMS measurements were performed to clarify the compositional profile further. Figure 35 shows the depth profile of positive ions of the main elements. Similarly, to the second-stage temperature modification process, the Cu, In, and Se profiles remain the same even after the recrystallization. A drastic change in the Ga profile was observed. The Ga profile normally has a deep Ga notch (seen in the reference), which diminishes significantly at low temperature and finally disappears and becomes flat at high temperature after the treatment. Also, a change in the Na profile was observed with an almost flat profile with decreased intensity in the CIGS region at high temperatures after the treatment. The K profile did not show any noticeable changes.

5.3 SOLAR CELLS DEVICE RESULTS

Solar cells were completed with reference and recrystallized CIGS films to evaluate the effect of vapor treatment on the device performance. The current density-voltage (J-V) and external quantum efficiency (EQE) plots for the CIGS solar cells fabricated using second-stage temperature control are shown in Figure 36. The corresponding photovoltaic characteristics and diode parameters of the representative cell are listed in Table 10. The diode parameters were extracted using dark I-V with a single-diode model. A change in all parameters can be observed after recrystallization. The short-circuit current density increases, open-circuit voltage decreases, and fill factor remains nearly the same after the second-stage low temperature process. The overall device performance remains the same. Also, the diode parameters such as reverse saturated current density, series and shunt resistance remain constant after recrystallization. Similarly, in the case of the second-stage high temperature process, the open-circuit voltage and short-circuit current density were the same as for the reference, whereas the fill factor increases. This increased overall device performance, with efficiency increasing from 9.6% to 11%. The diode quality factor decreases, and reverse saturation current density decreases. Also, shunt resistance was slightly higher, and series resistance was lower as compared to the reference. The bandgap of the second-stage sample was higher than the reference due to the change in the Ga profile after the recrystallization, which was consistent with the SIMS. The second-stage had nearly a flat Ga profile.

TABLE 10. Photovoltaic characteristics and Diode parameters of the representative cells shown in Figure 36.

Sample	V_{oc} (V)	J_{sc} (mA/cm ²)	FF (%)	η (%)	J_0 (mA/cm ²)	A	R_{SH} (Ω .cm ²)	R_S (Ω .cm ²)	E_g (eV)
Reference	0.55	32.0	54.8	9.6	5.4E-8	1.8	1.5E+4	2.0	1.09
2 nd -Stage LT	0.49	35.6	55.5	9.7	5.1E-8	1.7	1.8E+4	1.9	1.08
2 nd -Stage HT	0.54	32.3	63.3	11.0	2.0E-8	1.6	5.2E+4	1.3	1.13

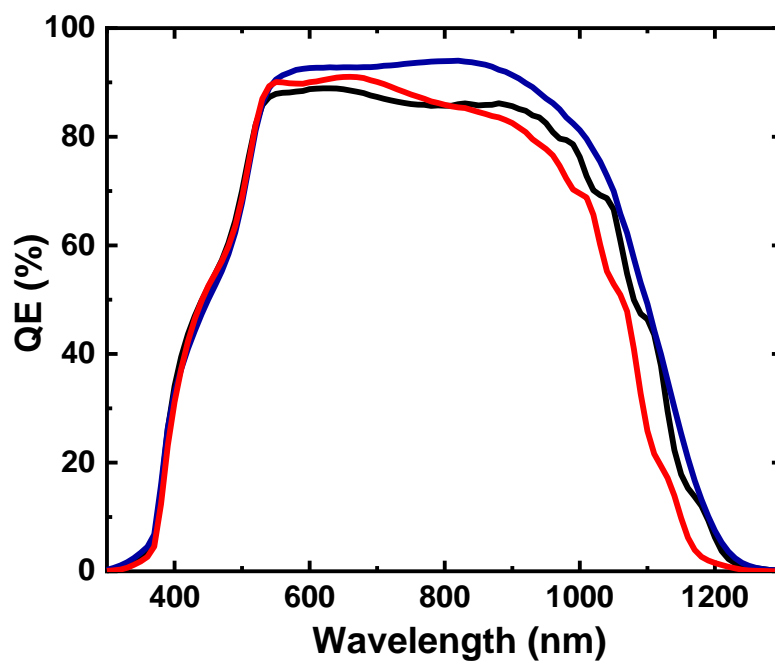
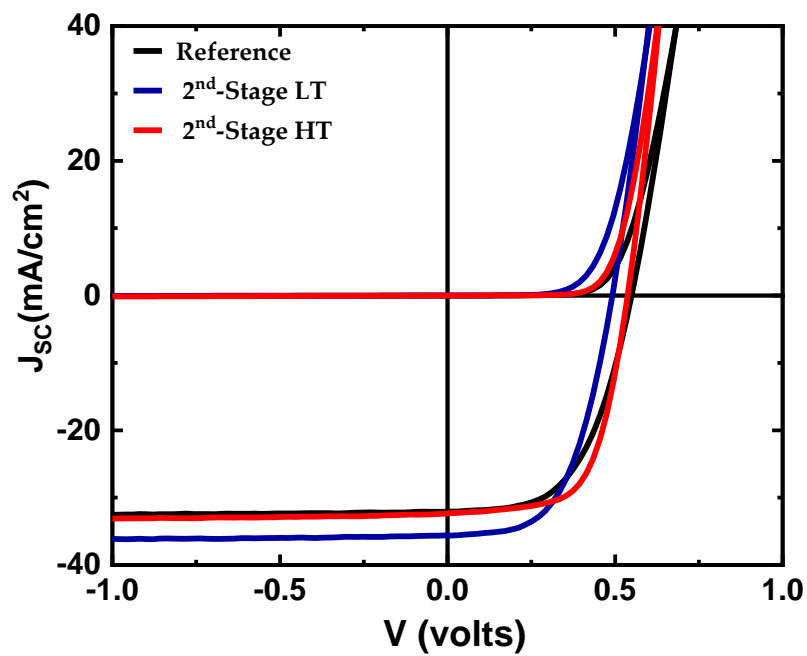


Figure 36. Representative J-V (top) and QE (bottom) curves for reference (black), 2nd-stage LT (blue) and 2nd-stage HT (red) devices.

Similarly, the J-V and QE plots for the CIGS solar cell devices fabricated using the third-stage temperature dependence are shown in Figure 37. The photovoltaic characteristics and corresponding diode parameters are shown in Table 11. An improvement of parameters such as fill factor and diode quality factor was observed. For the third-stage low temperature process, the open-circuit voltage and short-circuit current density remain the same, whereas the fill factor increases from 54.8% to 61%. The overall performance of the device improved. The decrease in short-circuit current density relates to a higher bandgap, according to the QE. This was consistent with the flat Ga profile seen by the SIMS. The open-circuit voltage decreases for the third-stage high temperature process, while the short-circuit current density and fill factor increases. The higher fill factor occurs due to slightly better shunt resistance, series resistance, and diode quality factor. However, the performance of the device remains constant. Regardless of the much larger grains, the lower Na content probably resulted in the lower open-circuit voltage for the third-stage high temperature process compared to reference samples. Voltage-dependent current collection was also observed. This suggests that the shorter diffusion length was possibly related to the modified Ga profile.

TABLE 11. Photovoltaic characteristics and Diode parameters of the representative cells shown in Figure 37.

Sample	V_{oc} (V)	J_{sc} (mA/cm ²)	FF (%)	η (%)	J_0 (mA/cm ²)	A	R_{sh} (Ω .cm ²)	R_s (Ω .cm ²)	E_g (eV)
Reference	0.55	32.0	54.8	9.6	5.4E-8	1.8	1.5E+4	2.0	1.09
3 rd -Stage LT	0.54	31.9	61.0	10.5	2.2E-8	1.6	4.8E+4	1.6	1.13
3 rd -Stage HT	0.51	28.8	61.0	9.0	5.1E-8	1.7	1.6E+4	1.7	1.18

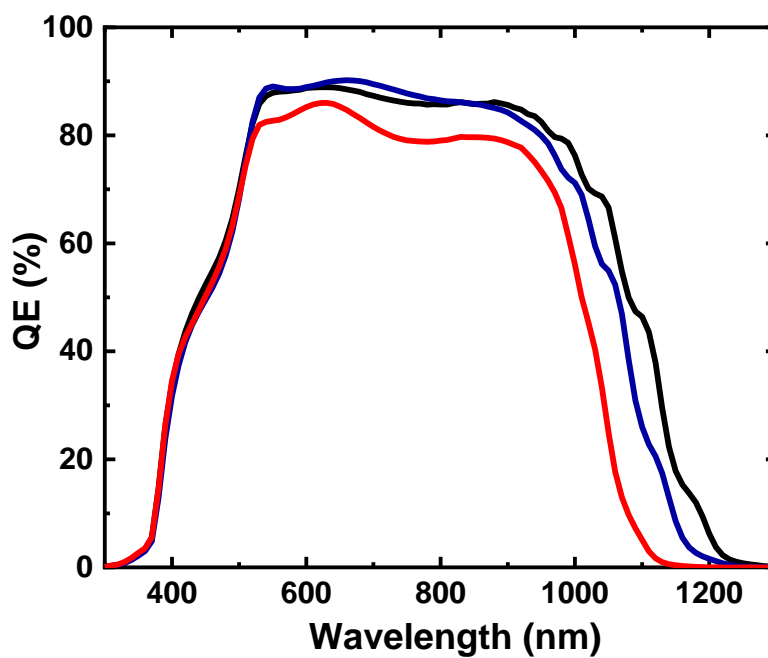
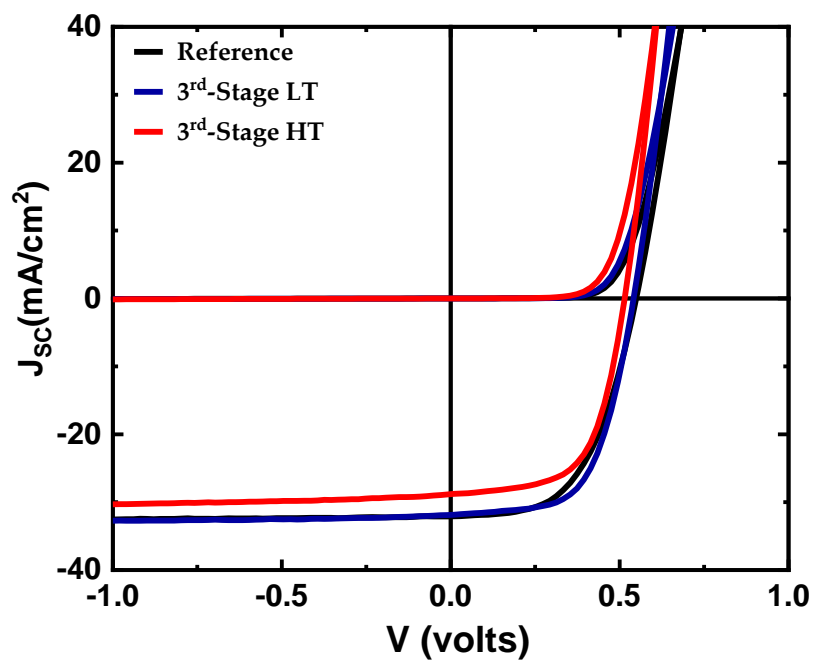


Figure 37. Representative J-V (top) and QE (bottom) curves for reference (black), 3rd-stage LT (blue) and 3rd-stage HT (red) devices.

5.4 SUMMARY

To promote the economic viability of CIGS solar cells in the multistage co-evaporation process while maintaining the high-quality absorber layer is a challenging task. To address this issue, a dynamic recrystallization process using a metal halide as a fluxing agent was used in this study. This technique significantly improves the materials process, and its effect on the nonmetallic system was explored. Here, CIGS thin films and devices were fabricated using a modified three-stage process. A copper chloride vapor treatment was introduced in between the second and third-stage to enhance the film properties using high deposition rates and low temperature during the process. The main parameter changed during the process was the substrate temperature in the second or third-stage and results were presented as the function of the second or third-stage temperature dependence. A radical modification in surface and cross-section morphology was observed by SEM as grain dimension drastically increased after the recrystallization. At high temperature, the films have the more prominent grain with size close or equal to the entire thickness, with enhancement in uniformity and grain size. The XRD measurements were used to investigate the crystallographic structure. In most cases, the peaks intensity increases, and FWHM decreases after the treatment, suggesting an increase in the grain size, which agrees with SEM results. SIMS verified the variation of some element depth profiles, especially Ga and Na. The Ga notch disappears for third-stage high temperature and becomes nearly flat, whereas the overall Na profile decreases as compared to the reference. However, the overall composition of the film did not change. The performance of the device was not as good as expected and did not reach high efficiency. The changes in Ga and Na seemed to decrease the device performance. Due to the competing effect of these changes, not all parameters of solar cells improved, producing an increase of device efficiency by 15% at best. Post-deposition treatments by alkali halides can solve the problem to some extent [21]. The reduction of the Ga can potentially be resolved by depositing pre-emptively a different Ga profile taking into account the redistribution. These two major changes would probably produce better devices at low temperatures and high-rates by this modified deposition process.

CHAPTER 6

IN-SITU RECRYSTALLIZATION OF CIGS THIN FILMS-II

CIGS thin film technology could become more competitive with the application of suitable halide treatment. The application of metal halides in CIGS is not straightforward due to the delicate compositional profile required to create high efficiency, as discussed in previous chapters. High substrate temperatures are common to facilitate large grain size and an optimal Ga profile [136, 137]. A low substrate temperature would decrease the production cost, but considerable drawbacks include smaller grain size and poor Ga grading [138, 139]. As a result, low temperature three-stage deposition processes have much lower device performance compared to the standard CIGS deposition process. CIGS could become more competitive economically with suitable metal halide treatment. While improving the grain size with metal halides has been shown in previous chapters, device quality has generally been poor. Most of the metal halides attempted were based on either In or Ga. While this prevented device shunting caused by the addition of copper [140], these processes resulted in non-ideal Ga profiles. Introducing the metal halides during the deposition process gives more latitude in modifying the film composition. Because of their high vapor pressure, In and Ga halides were replaced with an Ag halide. As a reminder, Ag is from group I_B, similarly to Cu. An Ag halide was used because of the larger grain size observed in ACIGS [141, 142]. Using AgBr for a CIGS recrystallization has one other distinct advantage. Because the initial film lacks Ag, it can be used as a tracing agent with dynamic SIMS to see if the halide localizes in a specific region. To test the potential of recrystallization, CIGS thin films were therefore prepared and annealed in the presence of AgBr as the fluxing agent.

6.1 EXPERIMENTAL DETAILS

A three-stage CIGS deposition was done on the molybdenum-coated soda-lime glass substrate at low temperatures. The first-stage CIGS growth was done with In, Ga, and Se flux and had a substrate temperature of 350°C, and the second-stage process was performed at 400°C with Cu and Se. Finally, In, Ga and Se deposition was done in the third-stage at a temperature of 450°C. There was no temperature flux grading of Ga during either the first or third-stage, as the possible changes

in the Ga profile were anticipated. The recrystallization occurred between the second and third-stage with a specific dose (40 mg) of AgBr flash evaporated in less than 2 minutes. Because most metal halide treatments previously resulted in detrimental device performance, two different runs were performed on the onset. For the first run, a source temperature was selected where the vapor pressure of AgBr would be relatively low. The second run increased the source temperature allowing for a faster flux rate and, hopefully, more AgBr vapor reaching the sample. For this, the AgBr source temperature used during the process were 540°C, considered the low-rate flux and 600°C, considered the high-rate flux.

During the flashing time, the substrate temperature was changed from 400°C to 450°C. To prevent group I enhancement within the film, AgBr was introduced after the second-stage. The endpoint was defined by the change in the emissivity of the sample, as the surface changes from Cu-rich to Cu-poor. After that, an extra 2 minutes of deposition was permitted before closing the shutter. In general, no post-deposition treatment was performed. A subset of samples went for post-deposition treatment with KF-Se or CsF-Se. The devices were completed with a basic structure of SLG/Mo/CIGS/CdS/i-ZnO/ITO/Grads with half of the samples, whereas the other half were used for characterization. The process was designed to get the accurate composition in the three-stage process so that the final composition should be Cu-poor and allows rapid recrystallization. The in-situ process was chosen over the ex-situ process, as the in-situ recrystallization process lessens the contamination cause by air exposure of the metal halides. The deposition rate was at the maximum offered by the deposition system. The low deposition temperature during the process, as compared to the traditional process, will lessen the thermal expansion stresses, decrease the tool cost, and speed up the process by lowering the heat up and cooling down procedure. The samples were characterized by scanning electron microscopy (SEM), energy-dispersive x-ray spectroscopy (EDS), x-ray diffraction (XRD), glancing incidence x-ray diffraction (GIXRD), x-ray fluorescence (XRF), secondary ion mass spectroscopy (SIMS), and transmission electron microscopy (TEM). The photovoltaic characteristics of the devices were evaluated by current density-voltage (J-V) measurements under AM 1.5G with a light intensity of 100 mW/cm² at 25°C and by external quantum efficiency (EQE) measurements.

6.2 RECRYSTALLIZATION BY SILVER BROMIDE TREATMENT

An extensive range of metal halides in previous chapters based on Cu and In has been analyzed. These were combined with Br and Cl, with or without the additional Se. When applied for treatment, all these compounds yield a considerable grain growth at a temperature below 500°C. The treatments usually result in a change in composition, which occurred in group III element loss. Group III halides have comparatively higher vapor pressures than the group I halides, and group III element elimination is likely. In this section, the recrystallization process was carried out between the second and third-stages of the three-stage process to address the group III element loss. Therefore, the time duration of the third-stage is controlled to result in a group III rich film. The process allows us to take advantage of the higher recrystallization rate for Cu-rich films. Also, the Cu-rich surface, typically with a copper selenide, reduces group III element loss. Here, in this part, the transport phenomena of AgBr has been explored. Ag is well known to improve CIGS films, if used in moderate quantities [143]. Br was found to be more reactive than Cl with Cu. Also, indium tribromides have been described to have higher vapor pressure than trichlorides [119, 144]. Here, in this chapter, the results demonstrating a three-stage, low-rate and high-rate, low temperature deposition process for CIGS, including a recrystallization step after the second-stage in the presence of AgBr has been studied.

6.2.1 LOW-RATE IN-SITU TREATMENT

The overall film microstructure was determined from the SEM cross-section, as shown in Figure 38. A change in grains size was observed but was not significant. The grains size appeared to be less than 0.5 μm . The multiple grains appear throughout the depth of the films in most areas. The grain growth is not uniform, less compact, and less distinct. It is concluded that the low-rate flux of AgBr was not able to produce a better grain size.

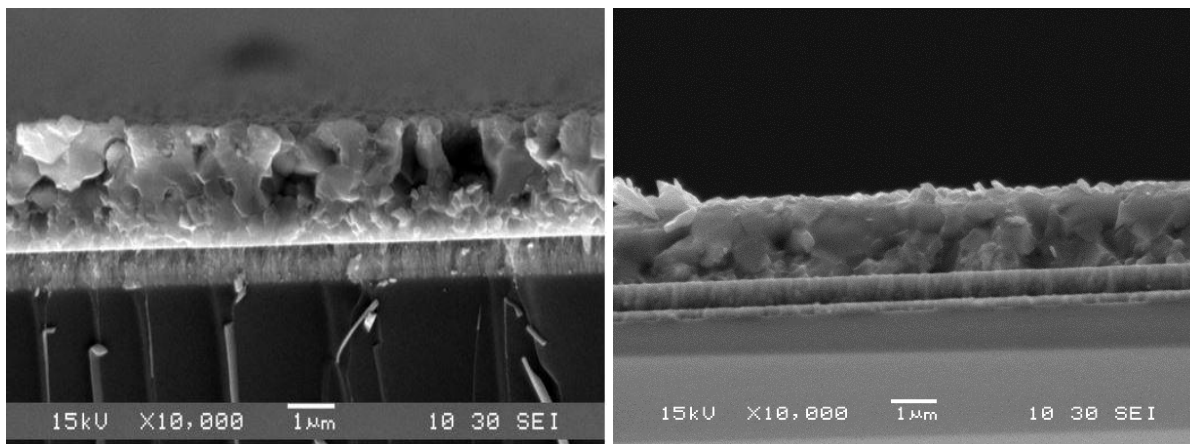


Figure 38. Scanning Electron Microscopy micrographs (cross-section) of CIGS films: reference (left) and low-rate AgBr-treated (right) samples.

To better understand the composition, the films were investigated by SIMS depth profile. The results are shown in Figure 39 in terms of the positive ions profile. The profile generally shows the different regions within the sample, with the Mo layer that underlines the film from 1100 to 2000 second sputter time, the CIGS portion from zero to 1100, and the soda-lime glass substrate is at the right-most region of the profile. The profile of the reference and low-rate AgBr samples follow a similar profile except for some changes. The main elements Cu, In, and Se profile remains constant in both cases. The Br was not found in any sample except directly below the surface. The reference sample showed a deep Ga notch, which primarily occurred in a three-stage process. The Na follows the Ga profile. After the recrystallization, the Ga notch slightly decreased, whereas the Na profile seemed to decrease compared to as-deposited samples. No significant changes were found in the case of K profile. The Ag signal is weak but present in the film. This matches with the fact that it is below the detection limits in the XRF measurements. The fact that the Ag signal is consistent throughout the film implies that Ag integrates itself into CIGS.

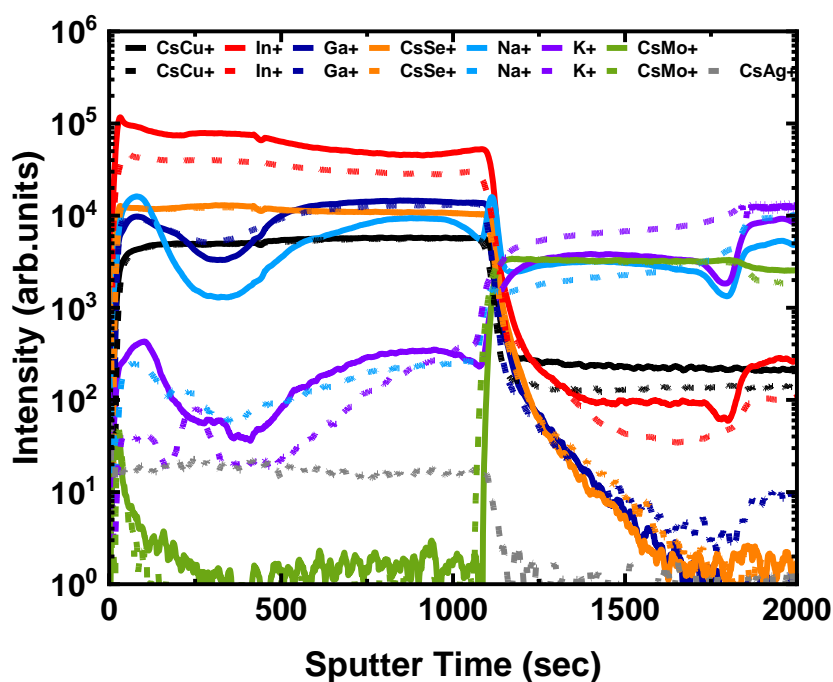
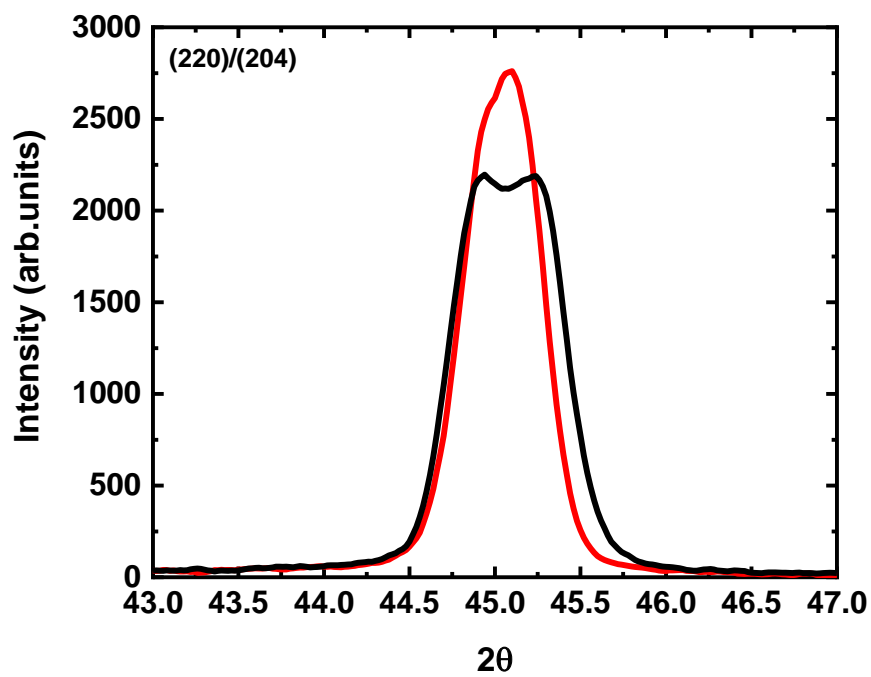
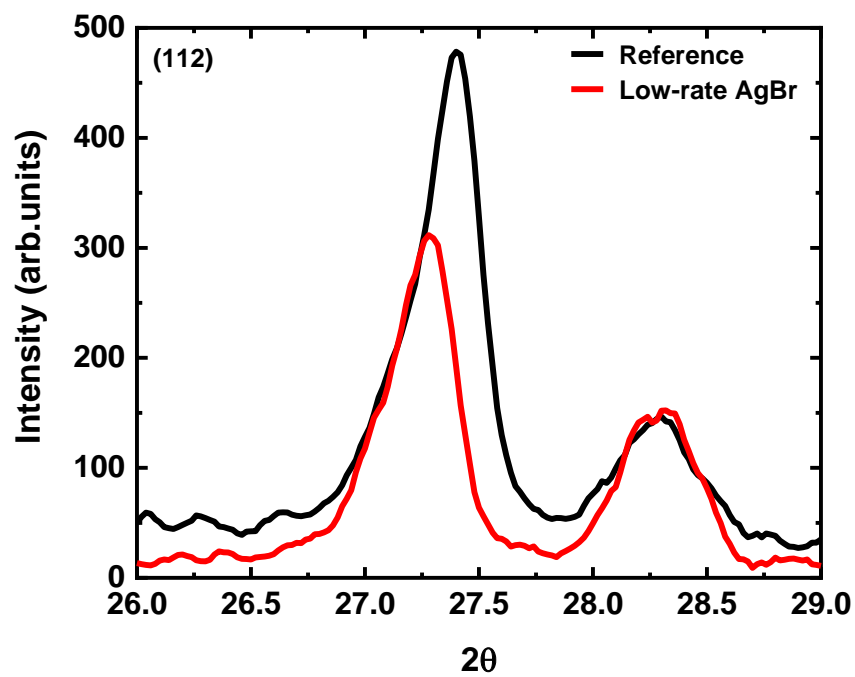


Figure 39. Secondary Ions Mass Spectroscopy depth profiles (positive ions) of the main elements for the reference (solid) and low-rate AgBr-treated (dash) CIGS samples.

The XRD measurements plots are shown in Figure 40 for three significant peaks (112), (220)/(204), and (312) demonstrated the preferential orientation compared to the standard powder pattern intensities, which preferred (112) plane diffraction. The corresponding parameters are shown in Table 12. The standard peak intensities for these peaks are 100% for the (112), <1% for the (103), 41% and 51% for the overlapping (220)/(204) peaks, and 25% for the (312) peak. The main feature of the XRD is the merging of the double peak at $\sim 45^\circ$. While the AgBr appears to have a similar peak doubling, that treatment appears to have mitigated it. The doubling most potentially was due to a deep Ga notch as observed in the SIMS measurements. The peak intensity increases, and FWHM decreases for peaks (220)/(204) and (312) after recrystallization. The peaks (220)/(204) shifts slightly to the lower angle, whereas (112) remain unchanged. The reference film showed the splitting of the peaks corresponding to the film's high and low Ga portion.



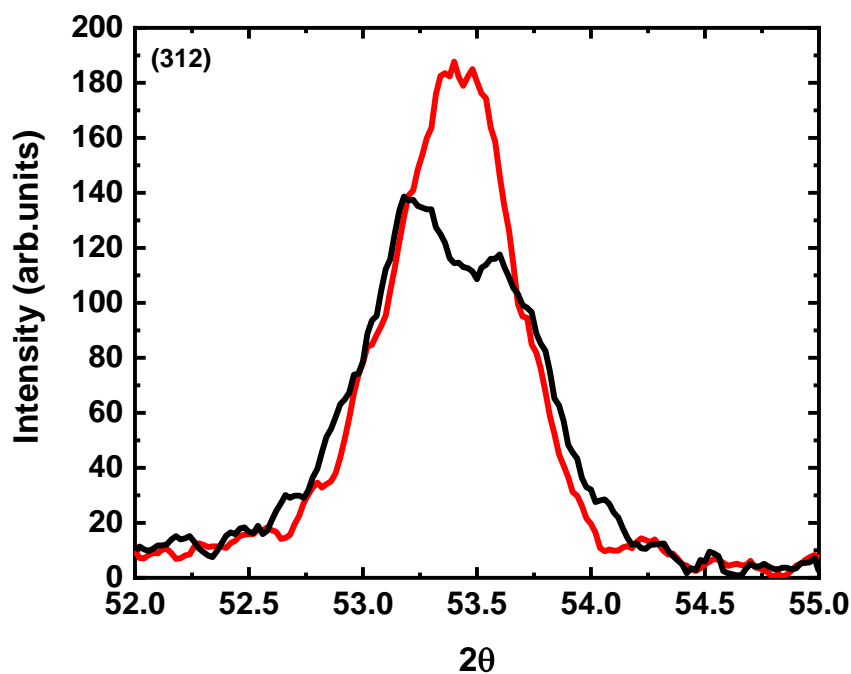


Figure 40. X-ray Diffraction plots of three key CIGS peaks (112), (204) and (312) for the reference (black) and low-rate AgBr (red) recrystallized CIGS samples.

TABLE 12. X-ray Diffraction and X-ray Fluorescence results of the reference and low-rate AgBr recrystallized CIGS samples.

Parameters	Reference				Low-rate AgBr-treated			
	112	103	220/204	(312)	112	103	220/204	(312)
Angle (deg)	27.4	28.3	44.8/45.2	53.3	27.3	28.3	44.9/45.1	53.4
Intensity (counts)	472	146	2239/2230	137	307	155	2524/2754	188
FWHM (deg)	0.30	0.41	0.31/0.45	0.82	0.32	0.36	0.22/0.44	0.61
Cu/III	0.78				0.80			
Ga/III	0.30				0.27			

6.2.2. HIGH-RATE IN-SITU TREATMENT

Since AgBr integrates well into the film and appears to facilitate Ga interdiffusion, the AgBr source temperature was increased. While the low-rate samples only had a marginal impact on the film, the high-rate AgBr showed significant changes, as demonstrated in Figure 41. The grains are uniform, denser, and more apparent. Many of these grains run the thickness through the entire film. Since sample breaking can create artifacts in cross-sectional SEM images, TEM was also performed via samples prepared with a focused ion beam, as shown in Figure 42. The grains cover the film depth where optical absorption, junction depletion depth, and minority carrier diffusion would occur. This can enhance carrier collection at greater depth in the CIGS. Nano-EDS analysis was then performed in the transmission electron microscope on a recrystallized sample, as shown in Figure 43. The Cu, In, Se and Na were uniformly distributed.

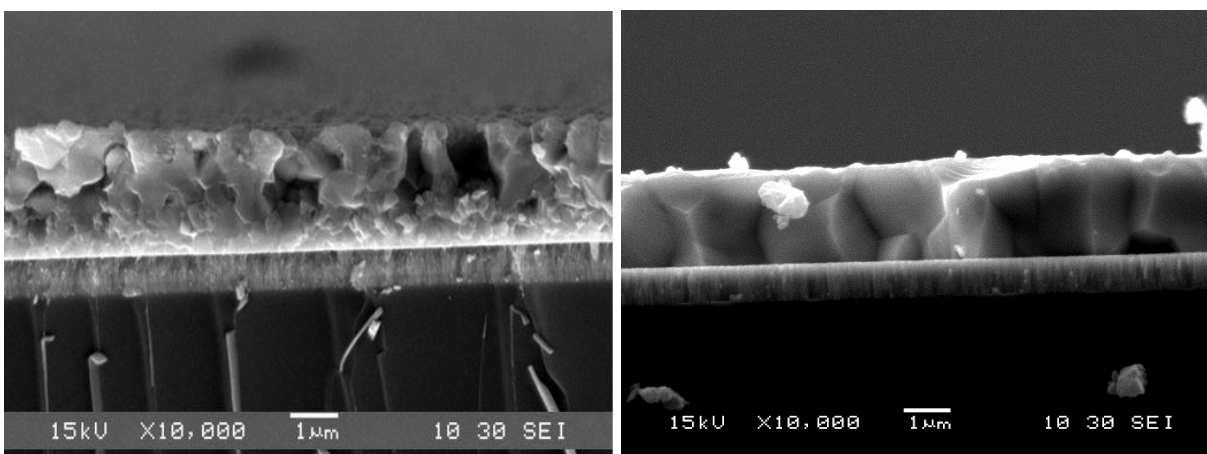


Figure 41. Scanning Electron Microscopy micrographs (cross-section) of CIGS films: reference (left) and high-rate AgBr-treated (right) samples.

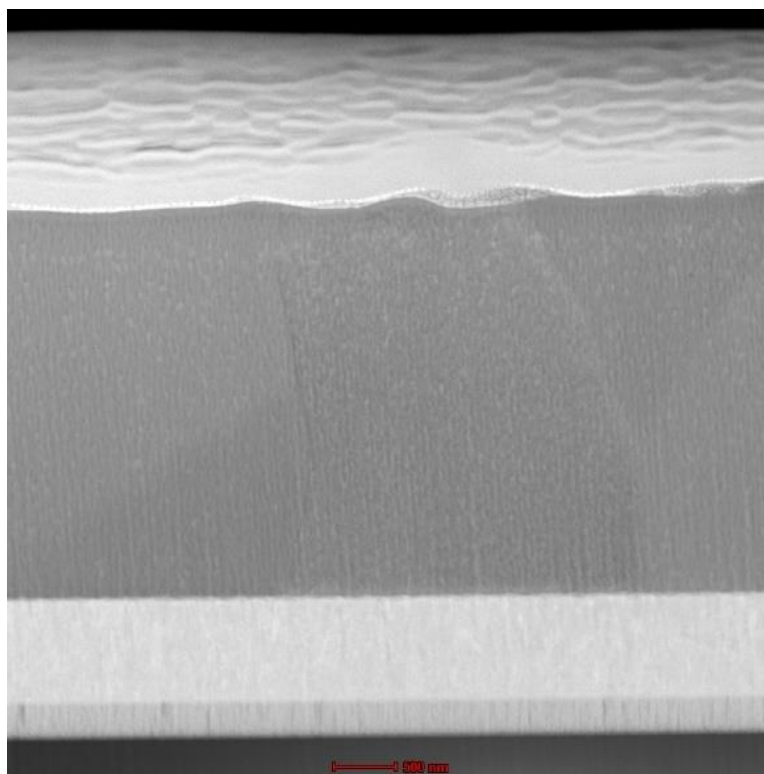
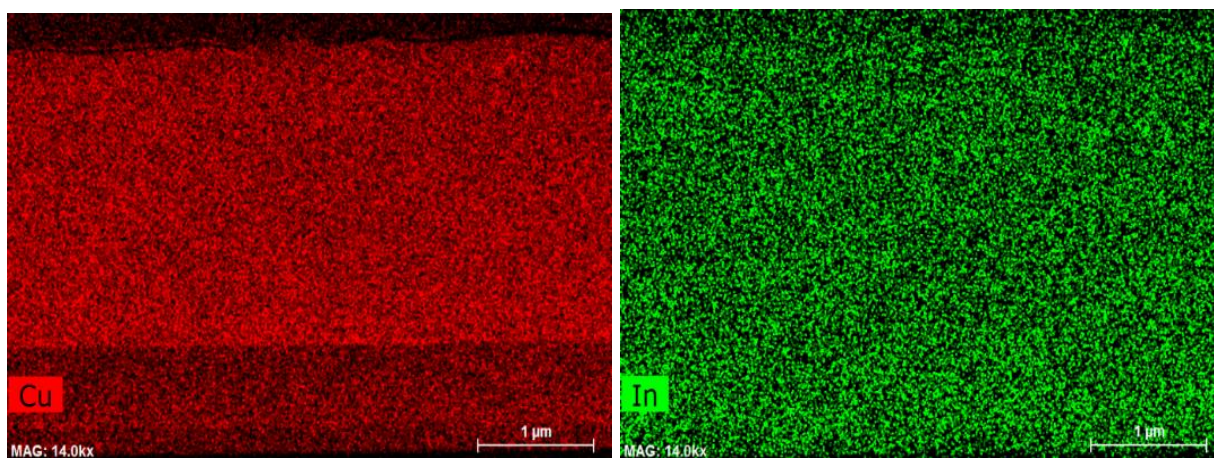


Figure 42. Transmission Electron Microscopy (TEM) (cross-section) of high-rate AgBr-treated CIGS sample.



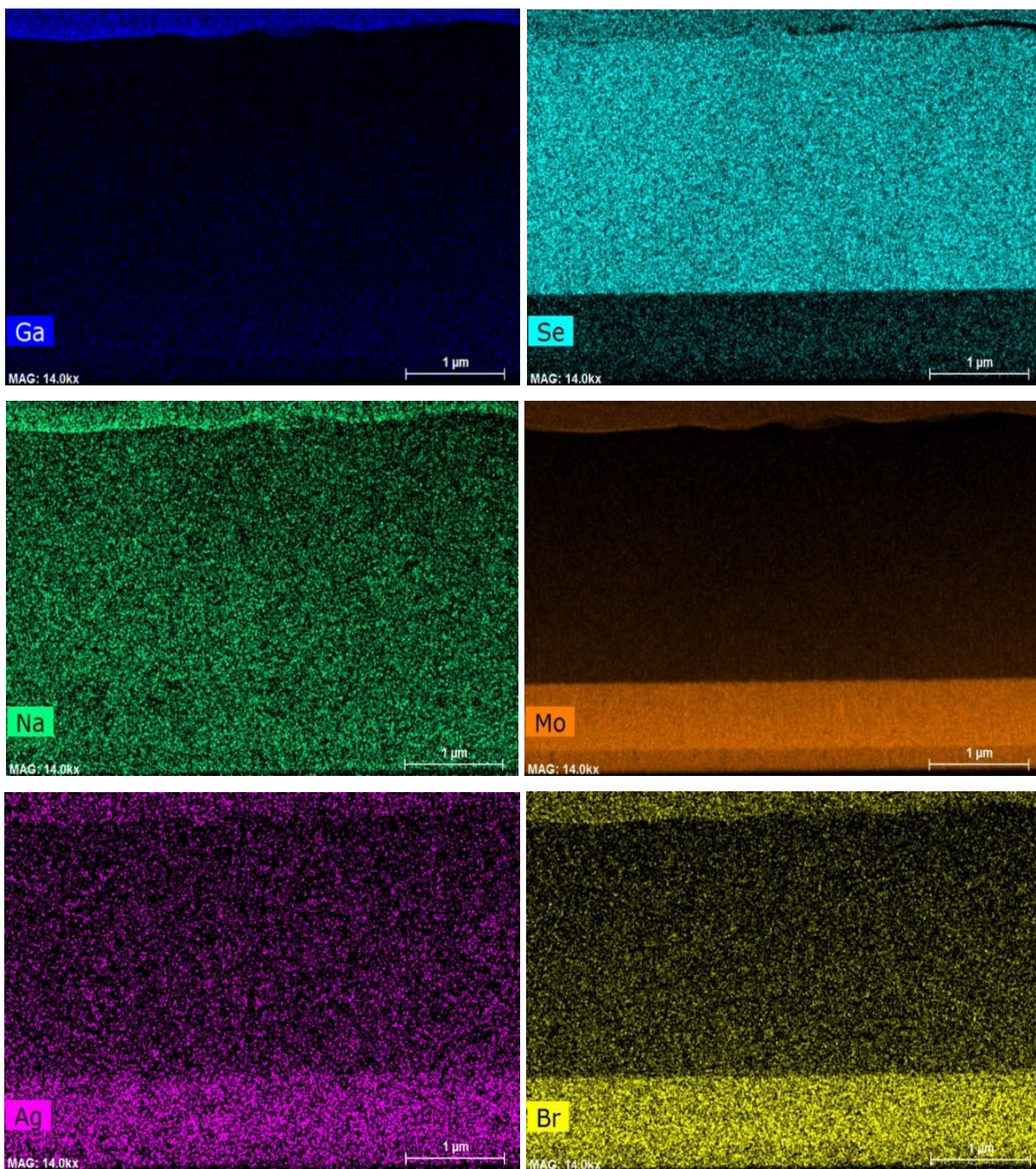


Figure 43. Elemental distribution of high-rate AgBr recrystallized CIGS sample measured by EDS in STEM.

The dynamic SIMS was performed to see the extent of Ga interdiffusion (Figure 44). After the treatment, the Ga notch was non-existent. Instead, only a gentle grading remains. Compared to the low-rate, the intensity of the Ag ions is a scale of magnitude larger. The Ag was uniformly distributed throughout the film, indicating a high-rate of Ag transport which was also consistent with EDS results. The Br did not seem to distribute into the film but supports the grain growth. As the SIMS indicated, there was a significant change in the Ga profiles compared to the reference. No change in the main elements (Cu, In, and Se) was observed, similarly to the low-rate AgBr. Before examining device performance, one final species needs to be examined more closely, the alkaline species. All the samples were grown on an alkaline-rich SLG substrate, but the alkaline profiles could vary significantly because of changes in grain boundary density and increased deposition time.

There was a small increase in the intensity of these alkali elements at the film depth where the recrystallization was conducted. The unique feature in the alkaline profiles was the peak observed in the Na in the high-rate sample. During the recrystallization step, nothing was being deposited on the film surface so that Na can accumulate there. Compared to the reference, Na composition was low because of two different factors: the low intragrain solubility of Na and a reduction in the number of grain boundaries. Because of the lower number of grain boundaries, there were fewer possible Na paths to diffuse through the film. Since the solubility of Na is much higher in the grain boundaries than the grain, the amount of Na decreased even further.

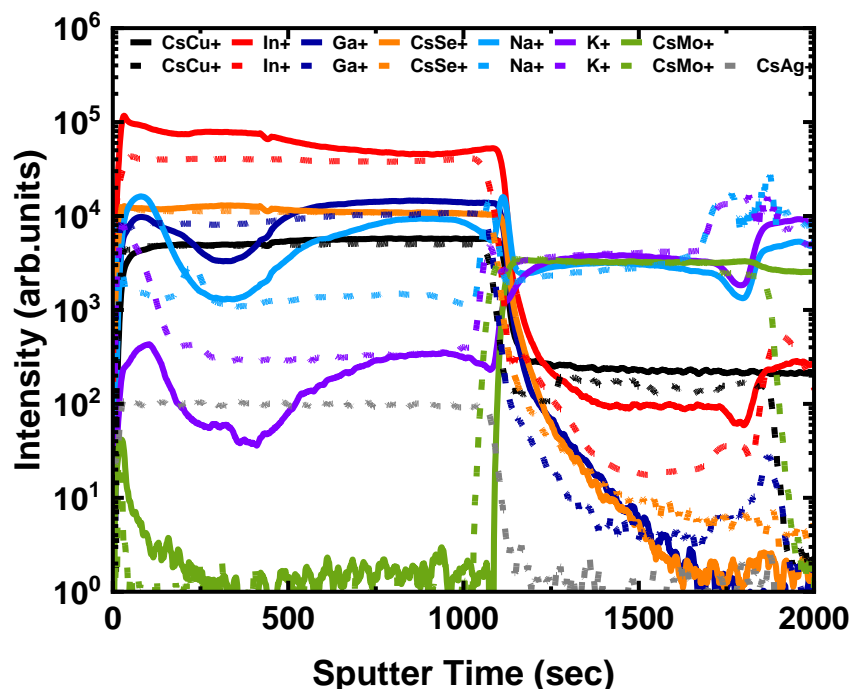
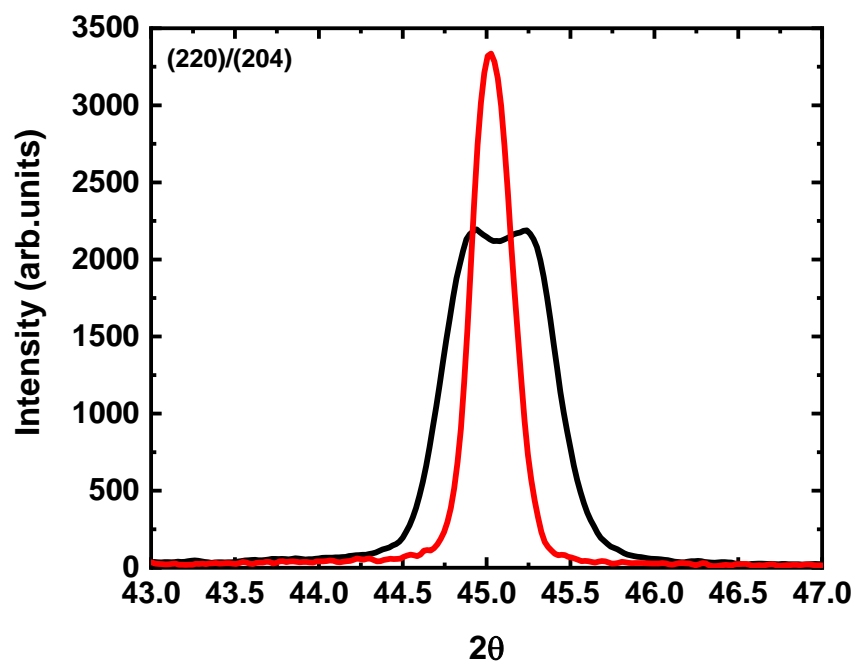
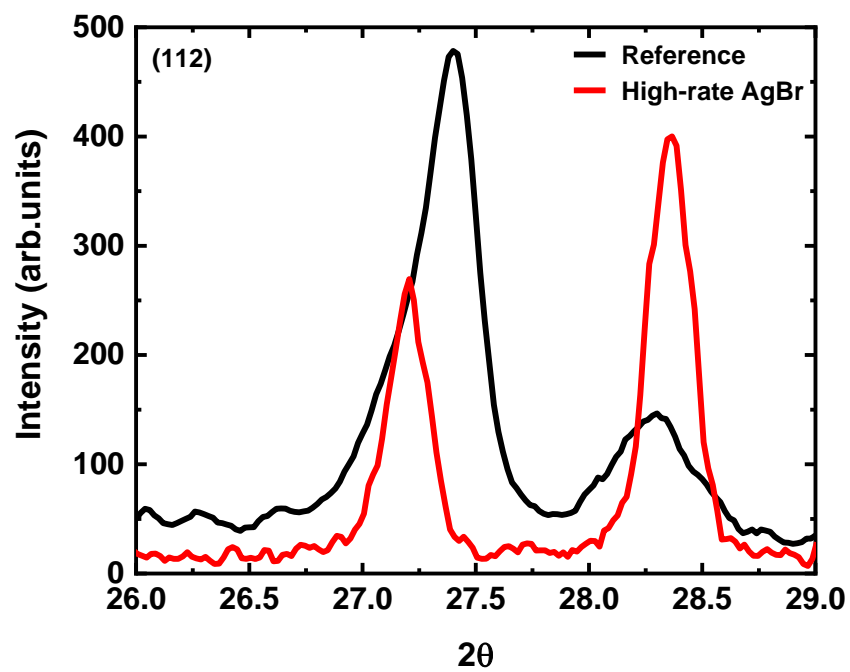


Figure 44. Secondary Ions Mass Spectroscopy depth profiles (positive ions) of the main elements for the reference (solid) and high-rate AgBr-treated (dash) CIGS samples.

While both the SEM and TEM showed a high crystallinity and uniformity, XRD was performed to see the primary film orientation and how the AgBr impacted the Ga interdiffusion. Looking at the XRD (Figure 45 and Table 13), there was a significant increase in height in almost all peaks. The peaks were also significantly narrower, with FWHM decreasing by at least 50% in all cases. This implies both a potential increase in grain size and a further shallowing of the Ga notch. The peaks sharpen and become more clearly a single Ga composition with a high-rate. However, the critical feature in the XRD pattern was the prevalence of the (103) peak. In most powder CIGS powder diffraction references, the relative intensity of the (103) peak is ~1%. While it is not uncommon to see a higher relative intensity of this peak in thin film diffraction patterns, it is always lower than the (112) peak. In previous thin film texture studies, high orientation in the (204) causes enhancement of the (103) peak [145]. Because of this, it can be inferred that the film was highly (204) oriented.



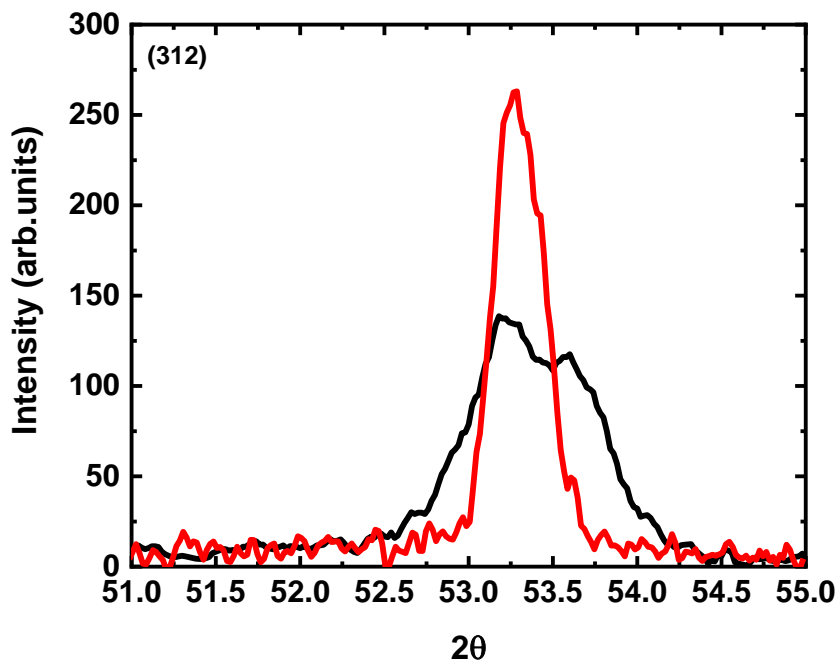
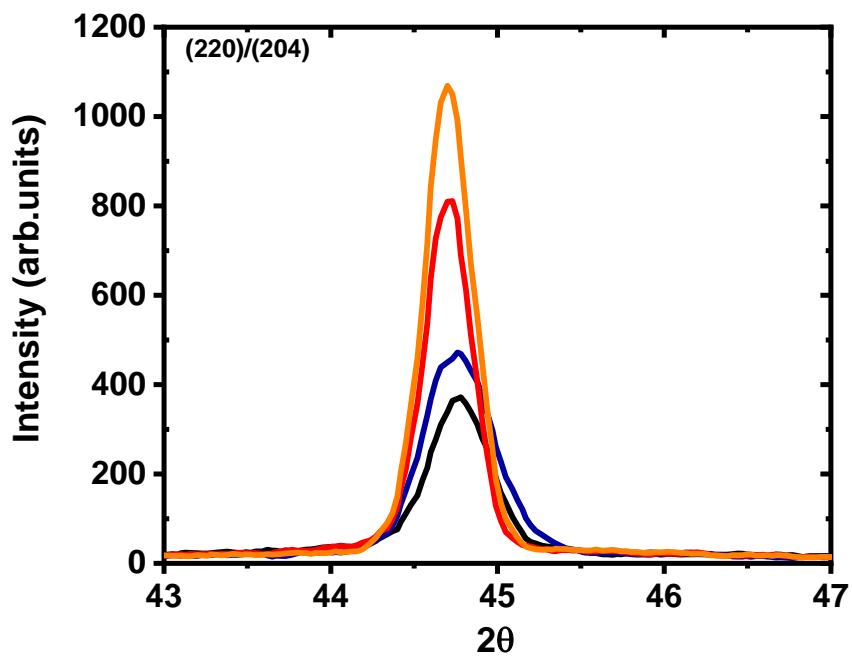
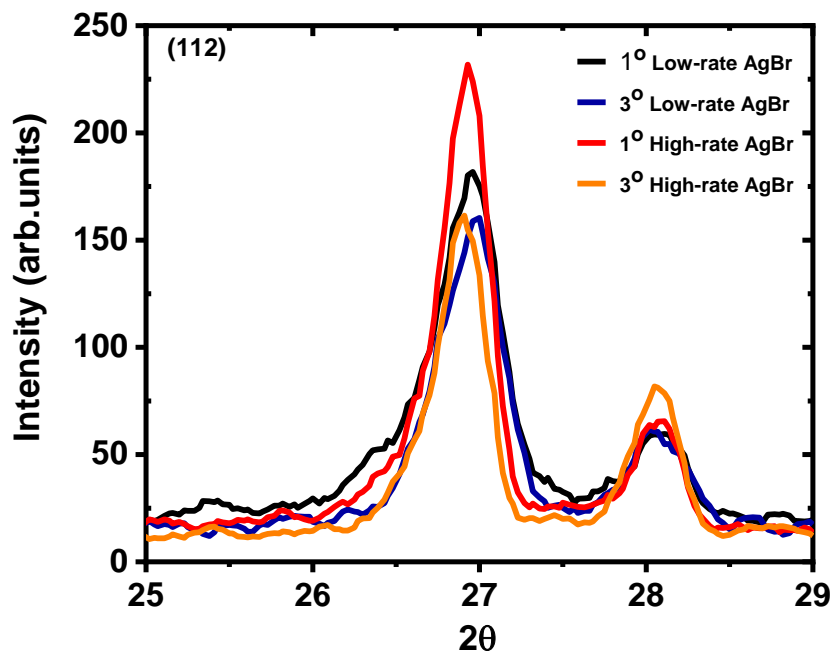


Figure 45. X-ray Diffraction plots of three key CIGS peaks (112), (204) and (312) for the reference (black) and high-rate AgBr-treated (red) recrystallized CIGS samples.

TABLE 13. X-ray Diffraction and X-ray Fluorescence results of the reference and high-rate AgBr recrystallized CIGS samples.

Parameters	Reference				High-rate AgBr-treated			
	112	103	220/204	(312)	112	103	220/204	(312)
Angle (deg)	27.4	28.3	44.8/45.2	53.3	27.2	28.4	45.0	53.2
Intensity (counts)	472	146	2239/2230	137	263	399	3271	264
FWHM (deg)	0.30	0.41	0.31/0.45	0.82	0.20	0.20	0.23	0.28
Cu/III	0.78				0.82			
Ga/III	0.30				0.25			



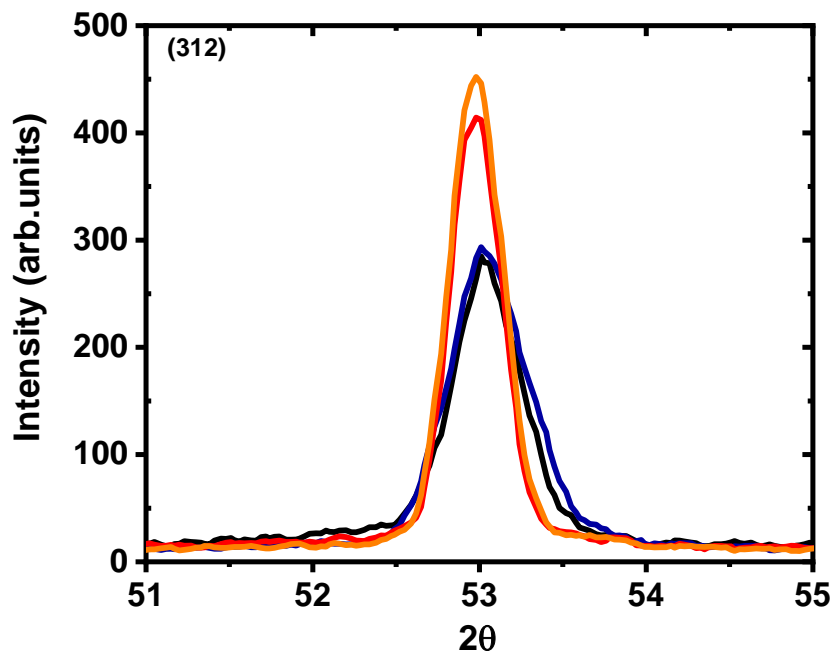


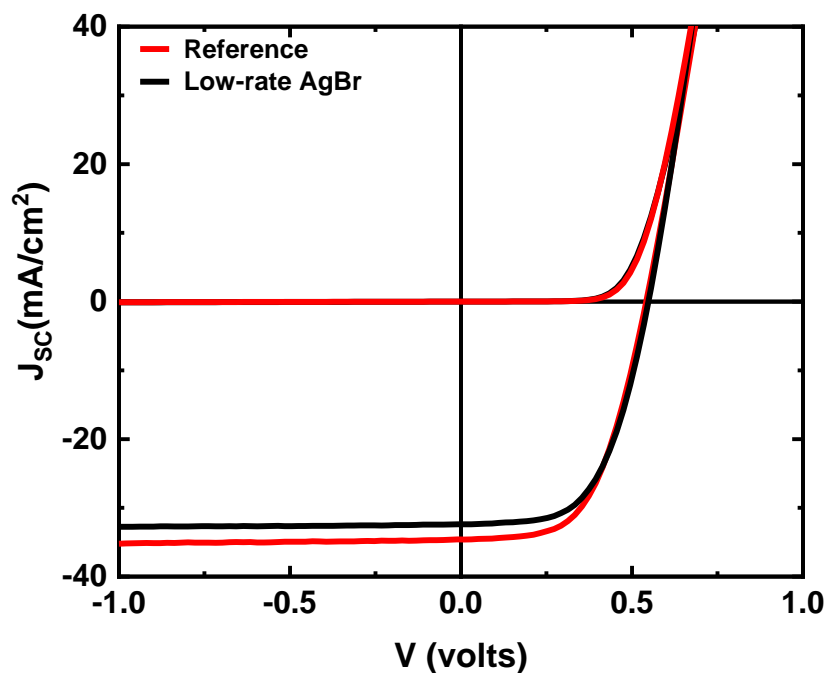
Figure 46. Grazing Incidence X-ray Diffraction of three key CIGS peaks (112), (204) and (312) at 1° and 3° for the low-rate and high-rate AgBr-treated samples.

The grazing incidence data showed a similar pattern to standard theta-two-theta scans. A difference in peaks between 1° and 3° was found. Since the (103) peak was so high, GIXRD was performed on these samples, as shown in Figure 46. Using GIXRD, the relative location of this orientation could be found. The GIXRD indicated that the (112) peak was present closer to the surface. As the angle of incidence increases, the (112) peak intensity decreases, and the (103) peak intensity increases. The (220)/(204) and (312) peaks in high-rate samples were more intense than other peaks.

6.3 SOLAR CELLS DEVICE RESULTS

While AgBr undoubtedly has a beneficial impact on the structure of CIGS thin films, the alkaline species, and the examining Ga profile, from a device perspective, are concerning. The J-V and QE for the reference and low-rate sample are shown in Figure 47, and corresponding photovoltaic parameters are summarized in Table 14.

Overall, there was only a minor improvement in device performance with the low-rate AgBr. Since the notch in Ga was mitigated by the AgBr treatment, a potential cut-off in the absorption edge in the QE would be expected, but it appears the treatment has only had a moderate impact on absorption at broader wavelengths. While the change was not significant, these results showed that AgBr does not inherently negatively impact device performance. The open-circuit voltage and fill factor remain almost the same. There was a slight increase in short-circuit current density.



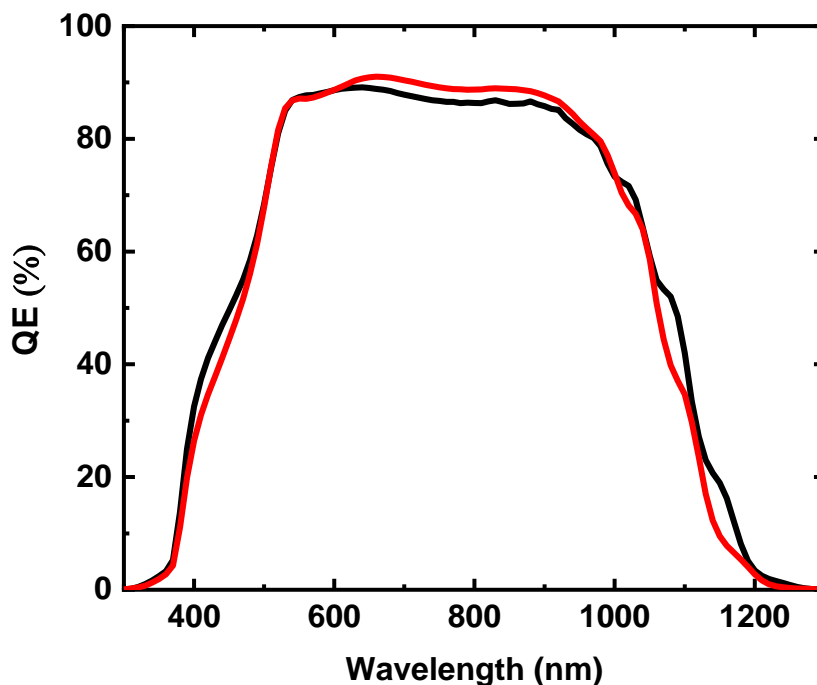


Figure 47. Representative J-V (top) and QE (bottom) curves for reference (black) and low-rate AgBr-treated (red) devices.

In contrast to low-rate AgBr sample, the high-rate AgBr sample significantly improves device performance in all key device parameters shown in Figure 48 and photovoltaic parameters summarized in Table 14. The open-circuit voltage and fill factor increase, whereas the short-circuit current density remains almost the same as compared to low-rate. The reference and low-rate AgBr devices have high series resistance that tends to decrease the fill factor. Also, the loss of Ga gradient spreads Ga throughout the film and increases the energy gap. While the QE in the low-rate sample did not demonstrate significant variance in the optical bandgap, the high-rate has a distinct cut-off at a lower wavelength. This again showed the impact of AgBr on Ga interdiffusion. The highly specular surface of the sample causes additional reflective losses that an anti-reflective coating would mitigate.

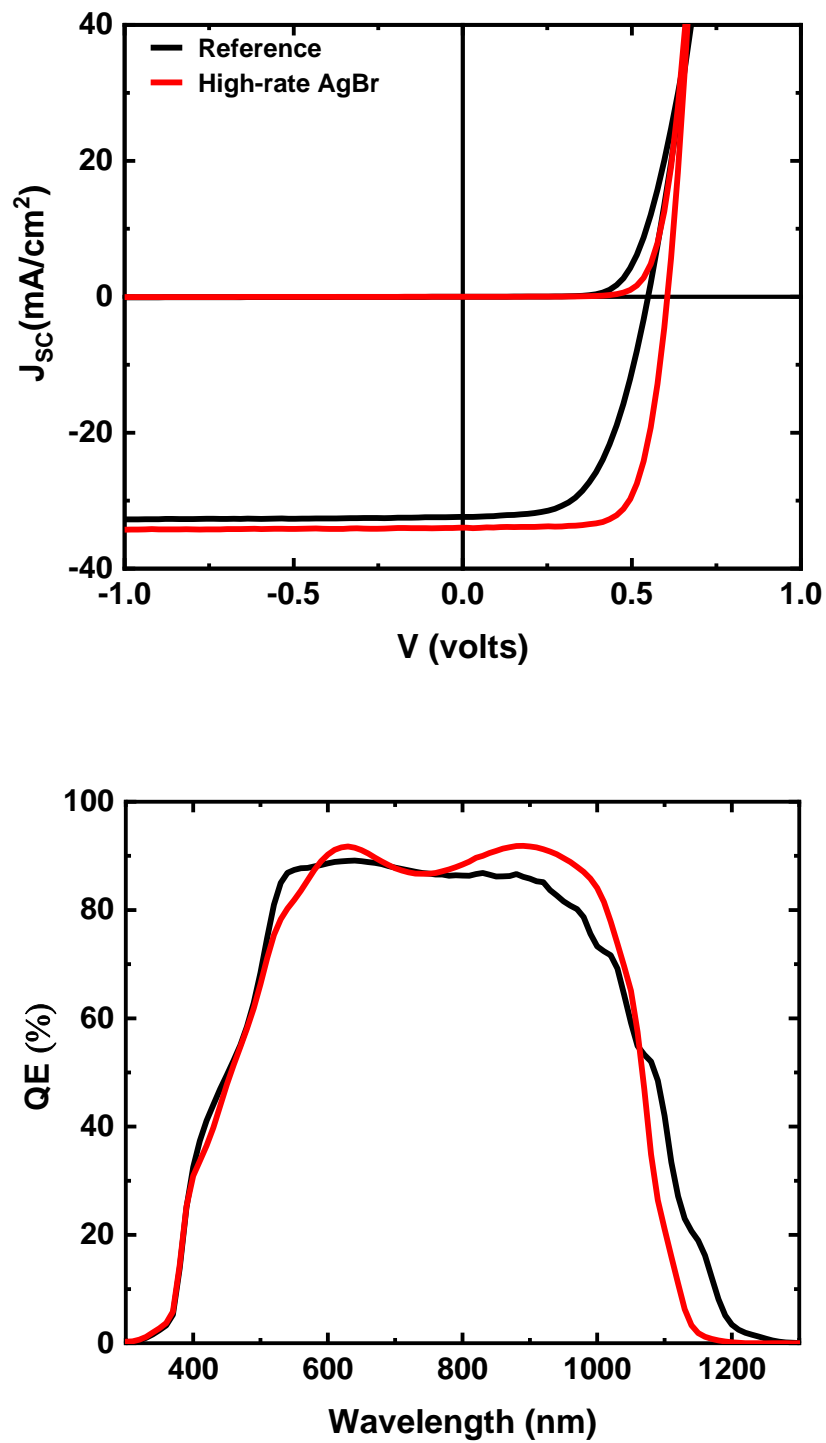


Figure 48. Representative J-V (top) and QE (bottom) curves for reference (black) and high-rate AgBr-treated (red) devices.

TABLE 14. Photovoltaic characteristics of the reference, low-rate AgBr, high-rate AgBr recrystallized and alkali-treated samples.

Samples	V_{oc} (V)	J_{sc} (mA/cm ²)	FF (%)	η (%)
Reference	0.55	32.4	57.5	10.2
Low-rate AgBr	0.54	34.6	56.4	10.5
High-rate AgBr	0.60	34.1	72.2	14.8
High-rate AgBr + CsF-Se	0.61	32.7	74.7	15.0
High-rate AgBr + KF-Se	0.67	33.2	73.2	16.3

Because of the significant increase in performance of the AgBr-treated sample, some samples also underwent a KF-Se and CsF-Se post-deposition treatment. With these treatments, the efficiency was pushed even higher. Figure 49 shows the current density vs. voltage and quantum efficiency measurements. The open-circuit voltage and fill factor increase by the CsF-Se treatment, which slightly increases the device performance. With KF-Se treatment, there was a further enhancement of device parameter in terms of open-circuit voltage and fill factor, whereas there was a slight reduction in short-circuit current density. Overall, the performance of the device was increased in comparison to high-rate AgBr treated samples, yielding efficiency as high as 16.3% without anti-reflective coating. The lower quantum efficiency resulted in a slight loss of photocurrent. The sample has a high fill factor and high efficiency even with the loss of Ga gradient in the film. A single-diode model also analyzed the devices. The ideality factor for the reference and low-rate AgBr was around 2 suggesting a high recombination in the space charge region leading to lower open-circuit voltage.

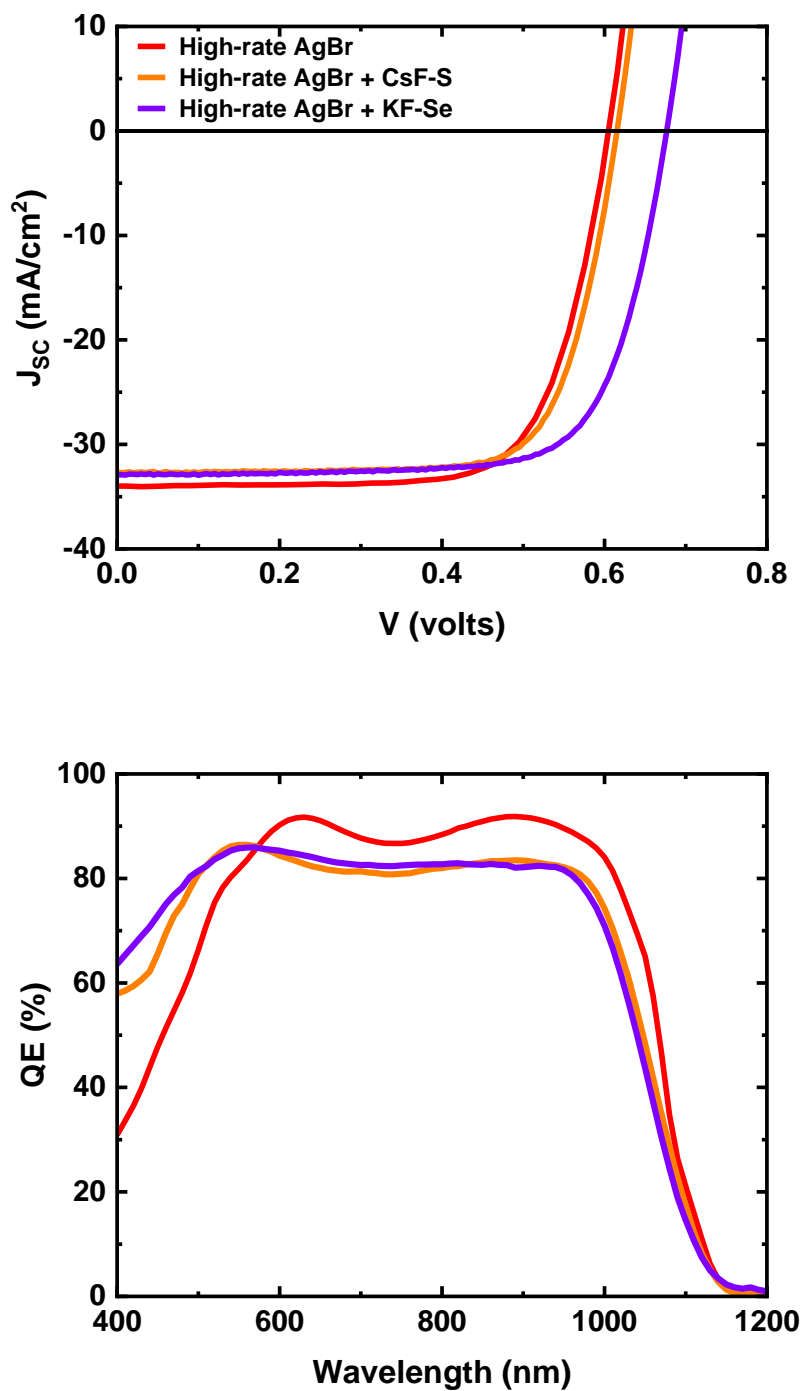


Figure 49. Representative J-V (top) and QE (bottom) curves for three CIGS devices with high-rate AgBr-treated and no post-deposition treatment (red), CsF-S treatment (orange) and KF-Se treatment (purple).

6.4 SUMMARY

A three-stage co-evaporation process usually produces high performance CIGS devices. The process is slow, typically taking more than one hour in deposition, and requires a very high temperature. Low temperature deposition yields degraded device performance with smaller grain size and poor Ga grading. This results in a high capital expense for process tools as the throughput is low. The outcomes in the previous chapters showed large grain size and change in composition but did not demonstrate better results in terms of device performance. In this chapter, AgBr vapor treatment was performed on CIGS semiconductor thin film using a three-stage thermal co-evaporation process deposited at low temperature and high-rate. The CIGS devices were fabricated on molybdenum-coated soda-lime glass with a structure SLG/Mo/CIGS/CdS/i-ZnO/ITO/Grids. The recrystallization process was done between the second and third-stages by flashing 40 mg of AgBr in 2 minutes. The flux rate was varied by changing the substrate temperature from 540°C to 600°C. The low-rate did not produce significant grain size, whereas drastic improvement in the grain growth was observed for high-rate AgBr, which was verified by TEM. With recrystallization, the peaks sharpen, FWHM decreases and becomes more clearly a single Ga composition compared to the reference, as seen by XRD. Also, from GIXRD results, it seemed that the peak (220)/(204) and (312) were more intense and related to the deeper layers of the film. From SIMS, it seemed that the Ga gradient disappears after high-rate AgBr treatment and a slight shift in the XRD peaks to a lower angle occurs, consistent with the Ga loss from the film. The Ag was uniformly distributed within the film, suggesting a high-rate of Ag transport. In terms of device performance, the low-rate AgBr has little effect on the device performance. The high-rate AgBr significantly reduced the series resistance, increased the fill factor and open-circuit voltage yielding solar cells with efficiency greater than 16.3% after post-deposition treatment with KF-Se. Optimizing alternative processes, with an effort to regain the Ga gradient, should result in still higher device performance, particularly with an anti-reflective coating. The result is a process that should reduce the time in a costly deposition tool by a factor of four or more and lessen the subsequent investment cost considerably.

CHAPTER 7

CONCLUSIONS

The potential to perform post-deposition treatments on polycrystalline solar cells to improve their optoelectronic and physical properties is crucial for developing PV technologies, as demonstrated by CdTe solar cells. The properties of CIGS semiconductor thin films and devices based on the ex-situ and in-situ post-deposition recrystallization by metal halides have been studied in this dissertation. Metal-based halides recrystallization of the CIGS absorber layer was performed with a process focused on high-rate and low-cost deposition with a 100°C decrease in CIGS deposition temperature and 10 times increase in the deposition rate, compared to standard references. The process is similar to the one used for CdTe recrystallization but done by replacing the group CdTe/CuCl₂ with CIGS/metal-halides treatment. The surface and cross-section morphology modification by InBr₃ and InCl₃ ex-situ post-deposition vapor treatment was observed as small grains transformed into grains of micrometer size. The films showed (220)/(204) preferential orientation as peak intensity increases and FWHM decreases after the treatment, implying the growth in the film crystallinity, which was coherent with the scanning electron microscope images. The development of a shoulder in the (220)/(204) XRD peak in a Se-annealed sample in case of high temperature InBr₃ recrystallization showed the development of two distinct phases. The hall effect measurements exhibited an improvement of the conductivity for the recrystallized films due to increased carrier concentration and mobility. The distinct characteristic in the XRD measurements was peak shifting and shoulder modification after the InCl₃ post-annealing treatment, hinting at an alteration in Ga and Na content, which agrees well with SIMS depth profiles. The rise in Na is beneficial for device performance, but unrestrained Ga profile changes yield poor device results. The variation of Ga within the film was not optimal, and post-deposition treatment induces Ga depletion at the surface, making the overall film In-rich. With the adjustment of Ga and Na profiles, high efficiency devices could be fabricated. Better control of the deposition process, more accurate timing calculation, and optimum amount of flux are required to obtain an ideal composition and elemental profile.

The in-situ recrystallization of CIGS films by CuCl_2 and AgBr vapor treatment yield much better results in terms of morphological, structural and device performance, as compared to ex-situ process. Grain sizes were larger, more compact, distinct, and uniform at higher temperatures than at lower temperatures. The increase in peak integrated intensity and decrease in FWHM indicates an increase in film crystallinity, and the peak shift seemed to suggest a redistribution of Ga throughout the film rather than a change of film composition. The depth of the Ga notch decreases considerably and nearly disappears in the case of high temperature process, with the introduction of CuCl_2 , indicating the interdiffusion of Ga due to the treatment, consistent with XRD calculation. The overall decrease in Na intensity after recrystallization suggests that the increase of grain size changes the grain boundary density and ultimately reduces the possible path for Na to diffuse through the films. The modification of Ga and Na due to low temperature and high deposition rates yields an overall increase of device performance by 15%. In AgBr -treated samples, the substantial increase in height in almost all peaks and considerably narrow FWHM decreasing by at least 50% in all cases, implies both a potential increase in grain size and a further diminishing of the Ga notch. The development of the (103) peak confirms the film was preferentially (204) oriented. Similarly, the flat Ga profile and decrease in the Na profile observed in AgBr -treated samples were probably due to the low intragrain solubility of Na. The high-rate AgBr demonstrated a substantial improvement in device performance compared to low-rate, producing the device efficiency up to 14.8%, further increasing to 16.3% with a post-deposition treatment with KF-Se . The loss of Ga gradient can be retrieved with the optimization of the CIGS deposition and post-deposition treatment process, which ultimately would produce better devices. The decrease of the alkali profile can be overcome with post-deposition treatment by Na and K. The variation in Ga can be controlled by pre-emptively depositing a layer with a higher Ga concentration at the front. The modified deposition process should produce devices with higher efficiency even at low temperatures with higher deposition rates. Further modification and analysis in terms of individual layer and variation in temperature, dose, and fluxes are required to understand the underlying mechanism to fabricate the solar cell devices with higher efficiency with dramatically reduction in corresponding capital cost.

REFERENCES

- [1] Y. Jia, G. Alva, and G. Fang, "Development and applications of photovoltaic–thermal systems: A review," *Renewable and Sustainable Energy Reviews*, vol. 102, pp. 249-265, 2019.
- [2] T. Kato, "Cu (In, Ga)(Se, S) 2 solar cell research in Solar Frontier: Progress and current status," *Japanese Journal of Applied Physics*, vol. 56, no. 4S, p. 04CA02, 2017.
- [3] V. Fthenakis, "Sustainability of photovoltaics: The case for thin-film solar cells," *Renewable and Sustainable Energy Reviews*, vol. 13, no. 9, pp. 2746-2750, 2009.
- [4] H. E. Murdock *et al.*, "Renewables 2019 Global Status Report," 2019.
- [5] A. Polman, M. Knight, E. C. Garnett, B. Ehrler, and W. C. Sinke, "Photovoltaic materials: Present efficiencies and future challenges," *Science*, vol. 352, no. 6283, p. aad4424, 2016.
- [6] M. Alaaeddin, S. Sapuan, M. Zuhri, E. Zainudin, and F. M. Al-Oqla, "Photovoltaic applications: Status and manufacturing prospects," *Renewable and Sustainable Energy Reviews*, vol. 102, pp. 318-332, 2019.
- [7] C. S. Lai, Y. Jia, L. L. Lai, Z. Xu, M. D. McCulloch, and K. P. Wong, "A comprehensive review on large-scale photovoltaic system with applications of electrical energy storage," *Renewable and Sustainable Energy Reviews*, vol. 78, pp. 439-451, 2017.
- [8] F. Meillaud *et al.*, "Recent advances and remaining challenges in thin-film silicon photovoltaic technology," *Materials Today*, vol. 18, no. 7, pp. 378-384, 2015.
- [9] T. D. Lee and A. U. Ebong, "A review of thin film solar cell technologies and challenges," *Renewable and Sustainable Energy Reviews*, vol. 70, pp. 1286-1297, 2017.
- [10] M. Yamaguchi, K. H. Lee, K. Araki, N. Kojima, H. Yamada, and Y. Katsumata, "Analysis for efficiency potential of high-efficiency and next-generation solar cells," *Progress in Photovoltaics: Research and Applications*, vol. 26, no. 8, pp. 543-552, 2018.
- [11] M. A. Green, "Commercial progress and challenges for photovoltaics," *Nature Energy*, vol. 1, no. 1, pp. 1-4, 2016.
- [12] H. Gullu, M. Isik, and N. Gasanly, "Structural and optical properties of thermally evaporated Cu-Ga-S (CGS) thin films," *Physica B: Condensed Matter*, vol. 547, pp. 92-96, 2018.

- [13] H. Salehi and E. Gordanian, "Ab initio study of structural, electronic and optical properties of ternary chalcopyrite semiconductors," *Materials Science in Semiconductor Processing*, vol. 47, pp. 51-56, 2016.
- [14] M.-M. Chen, H.-G. Xue, and S.-P. Guo, "Multinary metal chalcogenides with tetrahedral structures for second-order nonlinear optical, photocatalytic, and photovoltaic applications," *Coordination Chemistry Reviews*, vol. 368, pp. 115-133, 2018.
- [15] B. M. Basol, "I-III-VI₂ compound semiconductors for solar cell applications," *Journal of vacuum science and technology. A. Vacuum, surfaces, and films*, vol. 10, no. 4, pp. 2006-2012, 1992.
- [16] M. Nakamura, K. Yamaguchi, Y. Kimoto, Y. Yasaki, T. Kato, and H. Sugimoto, "Cd-free Cu (In, Ga)(Se, S) 2 thin-film solar cell with record efficiency of 23.35%," *IEEE Journal of Photovoltaics*, vol. 9, no. 6, pp. 1863-1867, 2019.
- [17] S. Siebentritt, M. Igalson, C. Persson, and S. Lany, "The electronic structure of chalcopyrites—bands, point defects and grain boundaries," *Progress in Photovoltaics: Research and Applications*, vol. 18, no. 6, pp. 390-410, 2010.
- [18] T. Glatzel, D. F. Marrón, T. Schedel-Niedrig, S. Sadewasser, and M. C. Lux-Steiner, "CuGaSe₂ solar cell cross section studied by Kelvin probe force microscopy in ultrahigh vacuum," *Applied physics letters*, vol. 81, no. 11, pp. 2017-2019, 2002.
- [19] T. K. Todorov, D. M. Bishop, and Y. S. Lee, "Materials perspectives for next-generation low-cost tandem solar cells," *Solar Energy Materials and Solar Cells*, vol. 180, pp. 350-357, 2018.
- [20] M. Green, E. Dunlop, J. Hohl-Ebinger, M. Yoshita, N. Kopidakis, and X. Hao, "Solar cell efficiency tables (version 57)," *Progress in photovoltaics: research and applications*, vol. 29, no. 1, pp. 3-15, 2021.
- [21] T. Feurer *et al.*, "Progress in thin film CIGS photovoltaics—Research and development, manufacturing, and applications," *Progress in Photovoltaics: Research and Applications*, vol. 25, no. 7, pp. 645-667, 2017.
- [22] T. Zhang *et al.*, "High efficiency solution-processed thin-film Cu (In, Ga)(Se, S) 2 solar cells," *Energy & Environmental Science*, vol. 9, no. 12, pp. 3674-3681, 2016.
- [23] J. Jaffe and A. Zunger, "Theory of the band-gap anomaly in AB₂C₂ chalcopyrite semiconductors," *Physical Review B*, vol. 29, no. 4, p. 1882, 1984.

- [24] S. Ishizuka, "CuGaSe₂ thin film solar cells: challenges for developing highly efficient wide-gap chalcopyrite photovoltaics," *physica status solidi (a)*, vol. 216, no. 15, p. 1800873, 2019.
- [25] D. R. Sapkota *et al.*, "Optimization of the CuInSe₂ Absorber for the Bottom Cell of a Polycrystalline Thin Film Tandem Solar Cell," *Bulletin of the American Physical Society*, vol. 65, 2020.
- [26] D. R. Sapkota *et al.*, "Spectroscopic Ellipsometry Investigation of CuInSe₂ as a Narrow Bandgap Component of Thin Film Tandem Solar Cells," in *2018 IEEE 7th World Conference on Photovoltaic Energy Conversion (WCPEC)(A Joint Conference of 45th IEEE PVSC, 28th PVSEC & 34th EU PVSEC)*, 2018: IEEE, pp. 1943-1948.
- [27] W. Shockley and H. J. Queisser, "Detailed Balance Limit of Efficiency of p-n Junction Solar Cells," *Journal of Applied Physics*, vol. 32, no. 3, pp. 510-519, 1961, doi: <http://dx.doi.org/10.1063/1.1736034>.
- [28] S. Ishizuka, A. Yamada, P. J. Fons, H. Shibata, and S. Niki, "Structural tuning of wide-gap chalcopyrite CuGaSe₂ thin films and highly efficient solar cells: differences from narrow-gap Cu (In, Ga) Se₂," *Progress in Photovoltaics: Research and Applications*, vol. 22, no. 7, pp. 821-829, 2014.
- [29] P. Paul, K. Aryal, S. Marsillac, S. Ringel, and A. Arehart, "Impact of the Ga/In ratio on defects in Cu (In, Ga) Se₂," in *2016 IEEE 43rd Photovoltaic Specialists Conference (PVSC)*, 2016: IEEE, pp. 2246-2249.
- [30] J. Hedstrom *et al.*, "ZnO/CdS/Cu (In, Ga) Se₂/thin film solar cells with improved performance," in *Conference Record of the Twenty Third IEEE Photovoltaic Specialists Conference-1993 (Cat. No. 93CH3283-9)*, 1993: IEEE, pp. 364-371.
- [31] M. B. Ård, K. Granath, and L. Stolt, "Growth of Cu (In, Ga) Se₂ thin films by coevaporation using alkaline precursors," *Thin Solid Films*, vol. 361, pp. 9-16, 2000.
- [32] S. Ishizuka *et al.*, "Na-induced variations in the structural, optical, and electrical properties of Cu (In, Ga) Se₂ thin films," *Journal of Applied Physics*, vol. 106, no. 3, p. 034908, 2009.
- [33] D. Rudmann *et al.*, "Efficiency enhancement of Cu (In, Ga) Se₂ solar cells due to post-deposition Na incorporation," *Applied Physics Letters*, vol. 84, no. 7, pp. 1129-1131, 2004.

- [34] D. Braunger, D. Hariskos, G. Bilger, U. Rau, and H. Schock, "Influence of sodium on the growth of polycrystalline Cu (In, Ga) Se₂ thin films," *Thin Solid Films*, vol. 361, pp. 161-166, 2000.
- [35] P. M. Salomé *et al.*, "Cu (In, Ga) Se₂ Solar Cells With Varying Na Content Prepared on Nominally Alkali-Free Glass Substrates," *IEEE Journal of Photovoltaics*, vol. 3, no. 2, pp. 852-858, 2013.
- [36] O. Cojocar-Mirédin, T. Schwarz, P.-P. Choi, M. Herbig, R. Wuerz, and D. Raabe, "Atom probe tomography studies on the Cu (In, Ga) Se₂ grain boundaries," *Journal of visualized experiments: JoVE*, no. 74, 2013.
- [37] E. Cadel, N. Barreau, J. Kessler, and P. Pareige, "Atom probe study of sodium distribution in polycrystalline Cu (In, Ga) Se₂ thin film," *Acta Materialia*, vol. 58, no. 7, pp. 2634-2637, 2010.
- [38] S.-H. Wei, S. Zhang, and A. Zunger, "Effects of Na on the electrical and structural properties of CuInSe₂," *Journal of Applied Physics*, vol. 85, no. 10, pp. 7214-7218, 1999.
- [39] D. J. Schroeder and A. A. Rockett, "Electronic effects of sodium in epitaxial CuIn_{1-x}Ga_xSe₂," *Journal of Applied Physics*, vol. 82, no. 10, pp. 4982-4985, 1997.
- [40] R. Scheer and H.-W. Schock, *Chalcogenide photovoltaics: physics, technologies, and thin film devices*. John Wiley & Sons, 2011.
- [41] A. Reinders, P. Verlinden, W. Van Sark, and A. Freundlich, *Photovoltaic solar energy: from fundamentals to applications*. John Wiley & Sons, 2017.
- [42] H. Wang *et al.*, "Effect of substrate temperature on the structural and electrical properties of CIGS films based on the one-stage co-evaporation process," *Semiconductor Science and Technology*, vol. 25, no. 5, p. 055007, 2010.
- [43] P. Reinhard *et al.*, "Features of KF and NaF Postdeposition Treatments of Cu (In, Ga) Se₂ Absorbers for High Efficiency Thin Film Solar Cells," *Chemistry of Materials*, vol. 27, no. 16, pp. 5755-5764, 2015.
- [44] C. Ferekides, U. Balasubramanian, R. Mamazza, V. Viswanathan, H. Zhao, and D. Morel, "CdTe thin film solar cells: device and technology issues," *Solar energy*, vol. 77, no. 6, pp. 823-830, 2004.

- [45] B. McCandless, L. Moulton, and R. Birkmire, "Recrystallization and sulfur diffusion in CdCl₂-treated CdTe/CdS thin films," *Progress in photovoltaics: Research and Applications*, vol. 5, no. 4, pp. 249-260, 1997.
- [46] Y. Tanaka, N. Akema, T. Morishita, D. Okumura, and K. Kushiya, "Improvement of Voc upward of 600mV/cell with CIGS-based absorber prepared by selenization/sulfurization," in *Conference Proceedings, 17th EC Photovoltaic Solar Energy Conference, Munich*, 2001, pp. 989-994.
- [47] L. Zhang *et al.*, "The effects of annealing temperature on CIGS solar cells by sputtering from quaternary target with Se-free post annealing," *Applied Surface Science*, vol. 413, pp. 175-180, 2017.
- [48] J. Liu, D. Zhuang, H. Luan, M. Cao, M. Xie, and X. Li, "Preparation of Cu (In, Ga) Se₂ thin film by sputtering from Cu (In, Ga) Se₂ quaternary target," *Progress in Natural Science: Materials International*, vol. 23, no. 2, pp. 133-138, 2013.
- [49] P. Jackson, R. Wuerz, D. Hariskos, E. Lotter, W. Witte, and M. Powalla, "Effects of heavy alkali elements in Cu (In, Ga) Se₂ solar cells with efficiencies up to 22.6%," *physica status solidi (RRL)–Rapid Research Letters*, vol. 10, no. 8, pp. 583-586, 2016.
- [50] G. Rajan *et al.*, "Impact of Post-Deposition Recrystallization by Alkali Fluorides on Cu (In, Ga) Se₂Thin-Film Materials and Solar Cells," *Thin Solid Films*, vol. 690, p. 137526, 2019.
- [51] H. Rodriguez-Alvarez *et al.*, "Recrystallization of Cu (In, Ga) Se₂ thin films studied by X-ray diffraction," *Acta materialia*, vol. 61, no. 12, pp. 4347-4353, 2013.
- [52] D. Poudel *et al.*, "Analysis of Post-Deposition Recrystallization Processing via Indium Bromide of Cu (In, Ga) Se₂ Thin Films," *Materials*, vol. 14, no. 13, p. 3596, 2021.
- [53] B. Belfore *et al.*, "Recrystallization of Cu (In, Ga) Se₂ Semiconductor Thin Films via InCl₃ Treatment," *Thin Solid Films*, p. 138897, 2021.
- [54] B. Belfore, D. Poudel, T. Ashrafee, S. Karki, G. Rajan, and S. Marsillac, "Morphological Study of Indium Chloride Post Deposition Treated CuInSe₂ Thin Films," in *2021 IEEE 48th Photovoltaic Specialists Conference (PVSC)*, 2021: IEEE, pp. 2312-2315.
- [55] D. Poudel *et al.*, "Effect of Indium Bromide Treatments Post-Deposition Recrystallization Temperature on Cu (In, Ga) Se₂ Thin Films," in *2021 IEEE 48th Photovoltaic Specialists Conference (PVSC)*, 2021: IEEE, pp. 0429-0432.

- [56] B. Belfore *et al.*, "Study of Indium Chloride Vapor Treatment on Cu (In, Ga) Se₂ Semiconductor Thin Films," in *2021 IEEE 48th Photovoltaic Specialists Conference (PVSC)*, 2021: IEEE, pp. 2320-2323.
- [57] D. Poudel *et al.*, "In Situ Recrystallization of Co-Evaporated Cu (In, Ga) Se₂ Thin Films by Copper Chloride Vapor Treatment towards Solar Cell Applications," *Energies*, vol. 14, no. 13, p. 3938, 2021.
- [58] B. Belfore *et al.*, "Vapor Treatment and In-situ Recrystallization by Copper Chloride on Cu (In, Ga) Se₂ Thin Film," in *2021 IEEE 48th Photovoltaic Specialists Conference (PVSC)*, 2021: IEEE, pp. 2316-2319.
- [59] D. Poudel *et al.*, "Studying the Recrystallization of Cu (InGa) Se₂ Semiconductor Thin Films by Silver Bromide In-situ Treatment," in *2021 IEEE 48th Photovoltaic Specialists Conference (PVSC)*, 2021: IEEE, pp. 2307-2311.
- [60] S. M. Sze, *Semiconductor devices: physics and technology*. John Wiley & sons, 2008.
- [61] R. S. Muller, T. I. Kamins, M. Chan, and P. K. Ko, "Device electronics for integrated circuits," 1986.
- [62] A. Luque and S. Hegedus, *Handbook of photovoltaic science and engineering*. John Wiley & Sons, 2011.
- [63] C. J. Chen, *Physics of solar energy*. John Wiley & Sons, 2011.
- [64] P. Pistor, "Formation and electronic properties of In₂S₃/Cu (In, Ga) Se₂ junctions and related thin film solar cells," 2009.
- [65] C. Honsberg and S. J. Bowden, "PV education," Available: <https://www.pveducation.org>, 2014.
- [66] S. S. Hegedus and W. N. Shafarman, "Thin-film solar cells: device measurements and analysis," *Progress in Photovoltaics: Research and Applications*, vol. 12, no. 2-3, pp. 155-176, 2004.
- [67] P. Reinhard *et al.*, "Review of progress toward 20% efficiency flexible CIGS solar cells and manufacturing issues of solar modules," in *2012 IEEE 38th Photovoltaic Specialists Conference (PVSC) PART 2*, 2012: IEEE, pp. 1-9.
- [68] K. Chopra, P. Paulson, and V. Dutta, "Thin-film solar cells: an overview," *Progress in Photovoltaics: Research and applications*, vol. 12, no. 2-3, pp. 69-92, 2004.

- [69] J. Granata, J. Sites, S. Asher, and R. Matson, "Quantitative incorporation of sodium in CuInSe₂ and Cu (In, Ga) Se₂ photovoltaic devices," in *Conference Record of the Twenty Sixth IEEE Photovoltaic Specialists Conference-1997*, 1997: IEEE, pp. 387-390.
- [70] D. Rudmann, D. Brémaud, H. Zogg, and A. Tiwari, "Na incorporation into Cu (In, Ga) Se₂ for high-efficiency flexible solar cells on polymer foils," *Journal of Applied Physics*, vol. 97, no. 8, p. 084903, 2005.
- [71] F. Kessler and D. Rudmann, "Technological aspects of flexible CIGS solar cells and modules," *Solar Energy*, vol. 77, no. 6, pp. 685-695, 2004.
- [72] K. Otte, L. Makhova, A. Braun, and I. Konovalov, "Flexible Cu (In, Ga) Se₂ thin-film solar cells for space application," *Thin Solid Films*, vol. 511, pp. 613-622, 2006.
- [73] K. H. Ong *et al.*, "Review on substrate and molybdenum back contact in CIGS thin film solar cell," *International Journal of Photoenergy*, vol. 2018, 2018.
- [74] H. Khatri and S. Marsillac, "The effect of deposition parameters on radiofrequency sputtered molybdenum thin films," *Journal of Physics: Condensed Matter*, vol. 20, no. 5, p. 055206, 2008.
- [75] T. Wada, N. Kohara, S. Nishiwaki, and T. Negami, "Characterization of the Cu (In, Ga) Se₂/Mo interface in CIGS solar cells," *Thin Solid Films*, vol. 387, no. 1-2, pp. 118-122, 2001.
- [76] K.-J. Hsiao, J.-D. Liu, H.-H. Hsieh, and T.-S. Jiang, "Electrical impact of MoSe₂ on CIGS thin-film solar cells," *Physical Chemistry Chemical Physics*, vol. 15, no. 41, pp. 18174-18178, 2013.
- [77] K. Orgassa, H. W. Schock, and J. Werner, "Alternative back contact materials for thin film Cu (In, Ga) Se₂ solar cells," *Thin Solid Films*, vol. 431, pp. 387-391, 2003.
- [78] J. H. Scofield, A. Duda, D. Albin, B. Ballard, and P. Predecki, "Sputtered molybdenum bilayer back contact for copper indium diselenide-based polycrystalline thin-film solar cells," *Thin solid films*, vol. 260, no. 1, pp. 26-31, 1995.
- [79] P. Salomé, J. Malaquias, P. Fernandes, and A. Da Cunha, "Mo bilayer for thin film photovoltaics revisited," *Journal of Physics D: Applied Physics*, vol. 43, no. 34, p. 345501, 2010.

- [80] J. S. Park, Z. Dong, S. Kim, and J. H. Perepezko, "CuInSe₂ phase formation during Cu₂Se/In₂Se₃ interdiffusion reaction," *Journal of Applied Physics*, vol. 87, no. 8, pp. 3683-3690, 2000.
- [81] B. J. Stanbery, "Copper indium selenides and related materials for photovoltaic devices," *Critical reviews in solid state and materials sciences*, vol. 27, no. 2, pp. 73-117, 2002.
- [82] S. Zhang, S.-H. Wei, A. Zunger, and H. Katayama-Yoshida, "Defect physics of the CuInSe₂ chalcopyrite semiconductor," *Physical Review B*, vol. 57, no. 16, p. 9642, 1998.
- [83] S. Chen, X. Gong, A. Walsh, and S.-H. Wei, "Electronic structure and stability of quaternary chalcogenide semiconductors derived from cation cross-substitution of II-VI and I-III-VI₂ compounds," *Physical Review B*, vol. 79, no. 16, p. 165211, 2009.
- [84] S. Siebentritt, "Alternative buffers for chalcopyrite solar cells," *Solar energy*, vol. 77, no. 6, pp. 767-775, 2004.
- [85] T. Nakada and A. Kunioka, "Direct evidence of Cd diffusion into Cu (In, Ga) Se₂ thin films during chemical-bath deposition process of CdS films," *Applied Physics Letters*, vol. 74, no. 17, pp. 2444-2446, 1999.
- [86] S. Lee *et al.*, "Effect of annealing treatment on CdS/CIGS thin film solar cells depending on different CdS deposition temperatures," *Solar Energy Materials and Solar Cells*, vol. 141, pp. 299-308, 2015.
- [87] R. Ortega-Borges and D. Lincot, "Mechanism of Chemical Bath Deposition of Cadmium Sulfide Thin Films in the Ammonia-Thiourea System: In Situ Kinetic Study and Modelization," *Journal of the Electrochemical Society*, vol. 140, no. 12, p. 3464, 1993.
- [88] D. Hariskos, S. Spiering, and M. Powalla, "Buffer layers in Cu (In, Ga) Se₂ solar cells and modules," *Thin Solid Films*, vol. 480, pp. 99-109, 2005.
- [89] W. Witte, S. Spiering, and D. Hariskos, "Substitution of the CdS buffer layer in CIGS thin-film solar cells: Status of current research and record cell efficiencies," *Vakuum in Forschung und Praxis*, vol. 26, no. 1, pp. 23-27, 2014.
- [90] N. Naghavi *et al.*, "Buffer layers and transparent conducting oxides for chalcopyrite Cu (In, Ga)(S, Se)₂ based thin film photovoltaics: present status and current developments," *Progress in Photovoltaics: Research and Applications*, vol. 18, no. 6, pp. 411-433, 2010.
- [91] E. Fortunato, D. Ginley, H. Hosono, and D. C. Paine, "Transparent conducting oxides for photovoltaics," *MRS bulletin*, vol. 32, no. 3, pp. 242-247, 2007.

- [92] S. Calnan and A. Tiwari, "High mobility transparent conducting oxides for thin film solar cells," *Thin solid films*, vol. 518, no. 7, pp. 1839-1849, 2010.
- [93] T. Minami, "Transparent conducting oxide semiconductors for transparent electrodes," *Semiconductor science and technology*, vol. 20, no. 4, p. S35, 2005.
- [94] J. Herrero and C. Guillen, "Improved ITO thin films for photovoltaic applications with a thin ZnO layer by sputtering," *Thin Solid Films*, vol. 451, pp. 630-633, 2004.
- [95] H. Liu, V. Avrutin, N. Izyumskaya, Ü. Özgür, and H. Morkoç, "Transparent conducting oxides for electrode applications in light emitting and absorbing devices," *Superlattices and Microstructures*, vol. 48, no. 5, pp. 458-484, 2010.
- [96] R. Noufi *et al.*, "Method of fabricating high-efficiency Cu (In, Ga)(SeS) 2 thin films for solar cells," ed: Google Patents, 1995.
- [97] L. Chen, S. Soltanmohammad, J. Lee, B. E. McCandless, and W. N. Shafarman, "Secondary phase formation in (Ag, Cu)(In, Ga) Se₂ thin films grown by three-stage co-evaporation," *Solar Energy Materials and Solar Cells*, vol. 166, pp. 18-26, 2017.
- [98] D. K. Schroder, *Semiconductor material and device characterization*. John Wiley & Sons, 2015.
- [99] K. Durose *et al.*, "Physical characterization of thin-film solar cells," *Progress in Photovoltaics: Research and Applications*, vol. 12, no. 2-3, pp. 177-217, 2004.
- [100] J. C. Vickerman and I. S. Gilmore, *Surface analysis: the principal techniques*. John Wiley & Sons, 2011.
- [101] D. Rudmann *et al.*, "Sodium incorporation strategies for CIGS growth at different temperatures," *Thin Solid Films*, vol. 480, pp. 55-60, 2005.
- [102] A. Laemmle, R. Wuerz, and M. Powalla, "Efficiency enhancement of Cu (In, Ga) Se₂ thin-film solar cells by a post-deposition treatment with potassium fluoride," *physica status solidi (RRL)–Rapid Research Letters*, vol. 7, no. 9, pp. 631-634, 2013.
- [103] C. P. Muzzillo, "Review of grain interior, grain boundary, and interface effects of K in CIGS solar cells: Mechanisms for performance enhancement," *Solar Energy Materials and Solar Cells*, vol. 172, pp. 18-24, 12// 2017.
- [104] E. Avancini *et al.*, "Effects of rubidium fluoride and potassium fluoride postdeposition treatments on Cu (In, Ga) Se₂ thin films and solar cell performance," *Chemistry of Materials*, vol. 29, no. 22, pp. 9695-9704, 2017.

- [105] S. Karki *et al.*, "Analysis of recombination mechanisms in RbF-treated CIGS solar cells," *IEEE Journal of Photovoltaics*, vol. 9, no. 1, pp. 313-318, 2018.
- [106] L. Zuo *et al.*, "Polymer-modified halide perovskite films for efficient and stable planar heterojunction solar cells," *Science advances*, vol. 3, no. 8, p. e1700106, 2017.
- [107] E. Wallin, T. Jarmar, U. Malm, M. Edoff, and L. Stolt, "Influence of the average Se-to-metal overpressure during co-evaporation of Cu (In_xGa_{1-x}) Se₂," *Thin Solid Films*, vol. 519, no. 21, pp. 7237-7240, 2011.
- [108] F. Kang, J. Ao, G. Sun, Q. He, and Y. Sun, "Properties of CuIn_xGa_{1-x}Se₂ thin films grown from electrodeposited precursors with different levels of selenium content," *Current Applied Physics*, vol. 10, no. 3, pp. 886-888, 2010.
- [109] K.-H. Liao, C.-Y. Su, Y.-T. Ding, and H.-S. Koo, "Microstructural characterization of CIGS formation using different selenization processes," *Applied surface science*, vol. 270, pp. 139-144, 2013.
- [110] K. H. Kim, K. H. Yoon, J. H. Yun, and B. T. Ahn, "Effects of Se flux on the microstructure of Cu (In, Ga) Se₂ thin film deposited by a three-stage co-evaporation process," *Electrochemical and Solid State Letters*, vol. 9, no. 8, p. A382, 2006.
- [111] D. Poudel *et al.*, "Degradation mechanism due to water ingress effect on the top contact of Cu (In, Ga) Se₂ solar cells," *Energies*, vol. 13, no. 17, p. 4545, 2020.
- [112] S. Karki *et al.*, "Degradation mechanism in Cu (In, Ga) Se₂ material and solar cells due to moisture and heat treatment of the absorber layer," *IEEE Journal of Photovoltaics*, vol. 9, no. 4, pp. 1138-1143, 2019.
- [113] O. Ayala *et al.*, "Theoretical Analysis of Experimental Data of Sodium Diffusion in Oxidized Molybdenum Thin Films," *Energies*, vol. 14, no. 9, p. 2479, 2021.
- [114] W. N. Shafarman, R. Klenk, and B. E. McCandless, "Device and material characterization of Cu (InGa) Se₂ solar cells with increasing band gap," *Journal of Applied Physics*, vol. 79, no. 9, pp. 7324-7328, 1996.
- [115] B. Belfore, O. Ayala, T. Ashrafee, G. Rajan, S. Karki, and S. Marsillac, "Modeling diffusion of impurities in molybdenum thin films as a function of substrate temperature," *IEEE Journal of Photovoltaics*, vol. 9, no. 1, pp. 339-343, 2018.

- [116] D. Rudmann, G. Bilger, M. Kaelin, F.-J. Haug, H. Zogg, and A. Tiwari, "Effects of NaF coevaporation on structural properties of Cu (In, Ga) Se₂ thin films," *Thin Solid Films*, vol. 431, pp. 37-40, 2003.
- [117] A. Chirilă *et al.*, "Potassium-induced surface modification of Cu (In, Ga) Se₂ thin films for high-efficiency solar cells," *Nature materials*, vol. 12, no. 12, pp. 1107-1111, 2013.
- [118] M. Powalla, S. Paetel, E. Ahlswede, R. Wuerz, C. D. Wessendorf, and T. Magorian Friedlmeier, "Thin-film solar cells exceeding 22% solar cell efficiency: An overview on CdTe-, Cu (In, Ga) Se₂-, and perovskite-based materials," *Applied Physics Reviews*, vol. 5, no. 4, p. 041602, 2018.
- [119] B. Brunetti, C. Palchetti, and V. Piacente, "Sublimation enthalpy of indium tri-bromide," *Journal of materials science letters*, vol. 16, no. 16, pp. 1395-1397, 1997.
- [120] B. Brunetti, V. Piacente, and P. Scardala, "A Study on the Sublimation of Gallium Tribromide," *Journal of Chemical & Engineering Data*, vol. 54, no. 8, pp. 2273-2276, 2009.
- [121] Y. Sun *et al.*, "Review on alkali element doping in Cu (In, Ga) Se₂ thin films and solar cells," *Engineering*, vol. 3, no. 4, pp. 452-459, 2017.
- [122] M. Saifullah *et al.*, "Effect of Cu content on the photovoltaic properties of wide bandgap CIGS thin-film solar cells prepared by single-stage process," *Current Applied Physics*, vol. 16, no. 11, pp. 1517-1522, 2016.
- [123] S. Karki *et al.*, "Impact of water ingress on molybdenum thin films and its effect on Cu (In, Ga) Se₂ Solar Cells," *IEEE Journal of Photovoltaics*, vol. 10, no. 2, pp. 696-702, 2019.
- [124] W. C. Lim, J. Lee, and Y. Lee, "Characterization of Cu (InGa) Se₂ (CIGS) thin films in solar cell devices by secondary ion mass spectrometry," *Journal of Surface Analysis*, vol. 17, no. 3, pp. 324-327, 2011.
- [125] M. Raghuwanshi, E. Cadel, S. Duguay, L. Arzel, N. Barreau, and P. Pareige, "Influence of Na on grain boundary and properties of Cu (In, Ga) Se₂ solar cells," *Progress in Photovoltaics: Research and Applications*, vol. 25, no. 5, pp. 367-375, 2017.
- [126] K. Ramanathan *et al.*, "Properties of 19.2% efficiency ZnO/CdS/CuInGaSe₂ thin-film solar cells," *Progress in Photovoltaics: research and applications*, vol. 11, no. 4, pp. 225-230, 2003.

- [127] I. Repins *et al.*, "19.9%-efficient ZnO/CdS/CuInGaSe₂ solar cell with 81.2% fill factor," *Progress in Photovoltaics: Research and applications*, vol. 16, no. 3, pp. 235-239, 2008.
- [128] J. Chen *et al.*, "Effect of substrate temperature and post-annealing on the properties of CIGS thin films deposited using e-beam evaporation," *Journal of Physics D: Applied Physics*, vol. 49, no. 49, p. 495601, 2016.
- [129] J. D. Wilson, R. W. Birkmire, and W. N. Shafarman, "In-situ annealing of Cu (In, Ga) Se₂ films grown by elemental co-evaporation," in *2008 33rd IEEE Photovoltaic Specialists Conference*, 2008: IEEE, pp. 1-5.
- [130] W. N. Shafarman and J. Zhu, "Effect of substrate temperature and deposition profile on evaporated Cu (InGa) Se₂ films and devices," *Thin Solid Films*, vol. 361, pp. 473-477, 2000.
- [131] L. Zhang, Q. He, W.-L. Jiang, F.-F. Liu, C.-J. Li, and Y. Sun, "Effects of substrate temperature on the structural and electrical properties of Cu (In, Ga) Se₂ thin films," *Solar Energy Materials and Solar Cells*, vol. 93, no. 1, pp. 114-118, 2009.
- [132] S. Nishiwaki, T. Satoh, Y. Hashimoto, T. Negami, and T. Wada, "Preparation of Cu (In, Ga) Se₂ thin films at low substrate temperatures," *Journal of Materials Research*, vol. 16, no. 2, pp. 394-399, 2001.
- [133] Z. Yu *et al.*, "Significant effect of substrate temperature on the phase structure, optical and electrical properties of RF sputtered CIGS films," *Applied Surface Science*, vol. 264, pp. 197-201, 2013.
- [134] M. Nouri, Z. B. Ayadi, K. Khirouni, S. Alaya, K. Djessas, and S. Yapi, "Effect of substrate temperature and source grain size on the structural and electrical properties of CSVT grown Cu (In_{1-x}Ga_x) Se₂ thin films," *Materials Science and Engineering: C*, vol. 27, no. 5-8, pp. 1002-1006, 2007.
- [135] D. Poudel *et al.*, "Assessment of Cu (In, Ga) Se₂ Solar Cells Degradation due to Water Ingress Effect on the CdS Buffer Layer," 2021.
- [136] S. Schleussner, U. Zimmermann, T. Wätjen, K. Leifer, and M. Edoff, "Effect of gallium grading in Cu (In, Ga) Se₂ solar-cell absorbers produced by multi-stage coevaporation," *Solar Energy Materials and Solar Cells*, vol. 95, no. 2, pp. 721-726, 2011.

- [137] H. Mönig *et al.*, "Gallium gradients in chalcopyrite thin films: Depth profile analyses of films grown at different temperatures," *Journal of Applied Physics*, vol. 110, no. 9, p. 093509, 2011.
- [138] V. Achard *et al.*, "Study of gallium front grading at low deposition temperature on polyimide substrates and impacts on the solar cell properties," *IEEE Journal of Photovoltaics*, vol. 8, no. 6, pp. 1852-1857, 2018.
- [139] K. Zhang *et al.*, "Fabricating highly efficient Cu (In, Ga) Se₂ solar cells at low glass-substrate temperature by active gallium grading control," *Solar energy materials and solar cells*, vol. 120, pp. 253-258, 2014.
- [140] A. Virtuani, E. Lotter, M. Powalla, U. Rau, J. H. Werner, and M. Acciarri, "Influence of Cu content on electronic transport and shunting behavior of Cu (In, Ga) Se₂ solar cells," *Journal of Applied Physics*, vol. 99, no. 1, p. 014906, 2006.
- [141] L. Chen, J. Lee, and W. N. Shafarman, "The Comparison of (Ag, Cu)(In, Ga) Se₂ and Cu (In, Ga) Se₂ Thin Films Deposited by Three-Stage Coevaporation," *IEEE Journal of Photovoltaics*, vol. 4, no. 1, pp. 447-451, 2013.
- [142] L. Chen, J. Lee, B. E. McCandless, S. S. Soltanmohammad, and W. N. Shafarman, "Characterization of group I-rich growth during (Ag, Cu)(In, Ga) Se₂ three-stage co-evaporation," in *2014 IEEE 40th Photovoltaic Specialist Conference (PVSC)*, 2014: IEEE, pp. 0332-0336.
- [143] W. Shafarman, C. Thompson, J. Boyle, G. Hanket, P. Erslev, and J. D. Cohen, "Device characterization of (AgCu)(InGa) Se₂ solar cells," in *2010 35th IEEE Photovoltaic Specialists Conference*, 2010: IEEE, pp. 000325-000329.
- [144] B. Brunetti, V. Piacente, and P. Scardala, "A torsion study on the sublimation process of InCl₃," *Journal of Chemical & Engineering Data*, vol. 43, no. 1, pp. 101-104, 1998.
- [145] M. A. Contreras, B. Egaas, D. King, A. Swartzlander, and T. Dullweber, "Texture manipulation of CuInSe₂ thin films," *Thin Solid Films*, vol. 361, pp. 167-171, 2000.

APPENDIX

Permission for Chapter 4 (section 4.1 and 4.2) and Chapter 5 based on the reference 52 and 57, granted by MDPI publication.

Copyrights

Copyright and Licensing

For all articles published in MDPI journals, copyright is retained by the authors. Articles are licensed under an open access Creative Commons CC BY 4.0 license, meaning that anyone may download and read the paper for free. In addition, the article may be reused and quoted provided that the original published version is cited. These conditions allow for maximum use and exposure of the work, while ensuring that the authors receive proper credit.

In exceptional circumstances articles may be licensed differently. If you have specific condition (such as one linked to funding) that does not allow this license, please mention this to the editorial office of the journal at submission. Exceptions will be granted at the discretion of the publisher.

6/2/2022

Rightslink® by Copyright Clearance Center

CCC
RightsLink®



Home



Help ▾



Live Chat



Sign in



Create Account



Effect of Indium Bromide Treatments Post-Deposition Recrystallization Temperature on Cu(In,Ga)Se₂ Thin Films

Conference Proceedings: 2021 IEEE 48th Photovoltaic Specialists Conference (PVSC)

Author: Deewakar Poudel

Publisher: IEEE

Date: 20 June 2021

Copyright © 2021, IEEE

Thesis / Dissertation Reuse

The IEEE does not require individuals working on a thesis to obtain a formal reuse license, however, you may print out this statement to be used as a permission grant:

Requirements to be followed when using any portion (e.g., figure, graph, table, or textual material) of an IEEE copyrighted paper in a thesis:

- 1) In the case of textual material (e.g., using short quotes or referring to the work within these papers) users must give full credit to the original source (author, paper, publication) followed by the IEEE copyright line © 2011 IEEE.
- 2) In the case of illustrations or tabular material, we require that the copyright line © [Year of original publication] IEEE appear prominently with each reprinted figure and/or table.
- 3) If a substantial portion of the original paper is to be used, and if you are not the senior author, also obtain the senior author's approval.

Requirements to be followed when using an entire IEEE copyrighted paper in a thesis:

- 1) The following IEEE copyright/ credit notice should be placed prominently in the references: © [year of original publication] IEEE. Reprinted, with permission, from [author names, paper title, IEEE publication title, and month/year of publication]
- 2) Only the accepted version of an IEEE copyrighted paper can be used when posting the paper or your thesis online.
- 3) In placing the thesis on the author's university website, please display the following message in a prominent place on the website: In reference to IEEE copyrighted material which is used with permission in this thesis, the IEEE does not endorse any of [university/educational entity's name goes here]'s products or services. Internal or personal use of this material is permitted. If interested in reprinting/republishing IEEE copyrighted material for advertising or promotional purposes or for creating new collective works for resale or redistribution, please go to http://www.ieee.org/publications_standards/publications/rights/rights_link.html to learn how to obtain a License from RightsLink.

If applicable, University Microfilms and/or ProQuest Library, or the Archives of Canada may supply single copies of the dissertation.

BACK

CLOSE WINDOW

© 2022 Copyright - All Rights Reserved | Copyright Clearance Center, Inc. | [Privacy statement](#) | [Terms and Conditions](#)
Comments? We would like to hear from you. E-mail us at customer-care@copyright.com

6/2/2022

Rightslink® by Copyright Clearance Center



- Home
- Help ▾
- Live Chat
- Sign in
- Create Account



Recrystallization of Cu(In,Ga)Se₂ Semiconductor Thin Films via InCl₃ Treatment

Author: Benjamin Belfore, Deewakar Poudel, Shankar Karki, Sina Soltanmohammad, Elizabeth Palmiotti, Thomas Lepetit, Angus Rockett, Sylvain Marsillac

Publication: Thin Solid Films

Publisher: Elsevier

Date: 1 October 2021

© 2021 Elsevier B.V. All rights reserved.

Journal Author Rights

Please note that, as the author of this Elsevier article, you retain the right to include it in a thesis or dissertation, provided it is not published commercially. Permission is not required, but please ensure that you reference the journal as the original source. For more information on this and on your other retained rights, please visit: <https://www.elsevier.com/about/our-business/policies/copyright#Author-rights>

BACK

CLOSE WINDOW

© 2022 Copyright - All Rights Reserved | Copyright Clearance Center, Inc. | Privacy statement | Terms and Conditions
Comments? We would like to hear from you. E-mail us at customer-care@copyright.com

6/2/2022

Rightslink® by Copyright Clearance Center

CCC
RightsLink®



Morphological Study of Indium Chloride Post Deposition Treated CuInSe₂ Thin Films

Conference Proceedings: 2021 IEEE 48th Photovoltaic Specialists Conference (PVSC)

Author: Benjamin Belfore

Publisher: IEEE

Date: 20 June 2021

Copyright © 2021, IEEE

Thesis / Dissertation Reuse

The IEEE does not require individuals working on a thesis to obtain a formal reuse license, however, you may print out this statement to be used as a permission grant:

Requirements to be followed when using any portion (e.g., figure, graph, table, or textual material) of an IEEE copyrighted paper in a thesis:

- 1) In the case of textual material (e.g., using short quotes or referring to the work within these papers) users must give full credit to the original source (author, paper, publication) followed by the IEEE copyright line © 2011 IEEE.
- 2) In the case of illustrations or tabular material, we require that the copyright line © [Year of original publication] IEEE appear prominently with each reprinted figure and/or table.
- 3) If a substantial portion of the original paper is to be used, and if you are not the senior author, also obtain the senior author's approval.

Requirements to be followed when using an entire IEEE copyrighted paper in a thesis:

- 1) The following IEEE copyright/ credit notice should be placed prominently in the references: © [year of original publication] IEEE. Reprinted, with permission, from [author names, paper title, IEEE publication title, and month/year of publication]
- 2) Only the accepted version of an IEEE copyrighted paper can be used when posting the paper or your thesis online.
- 3) In placing the thesis on the author's university website, please display the following message in a prominent place on the website: In reference to IEEE copyrighted material which is used with permission in this thesis, the IEEE does not endorse any of [university/educational entity's name goes here]'s products or services. Internal or personal use of this material is permitted. If interested in reprinting/republishing IEEE copyrighted material for advertising or promotional purposes or for creating new collective works for resale or redistribution, please go to http://www.ieee.org/publications_standards/publications/rights/rights_link.html to learn how to obtain a License from RightsLink.

If applicable, University Microfilms and/or ProQuest Library, or the Archives of Canada may supply single copies of the dissertation.

BACK

CLOSE WINDOW

© 2022 Copyright - All Rights Reserved | Copyright Clearance Center, Inc. | [Privacy statement](#) | [Terms and Conditions](#)
Comments? We would like to hear from you. E-mail us at customer@copyright.com

6/2/2022

Rightslink® by Copyright Clearance Center



[Home](#)
[Help](#)
[Live Chat](#)
[Sign in](#)
[Create Account](#)



Studying the Recrystallization of Cu(InGa)Se₂ Semiconductor Thin Films by Silver Bromide In-situ Treatment

Conference Proceedings: 2021 IEEE 48th Photovoltaic Specialists Conference (PVSC)

Author: Deewakar Poudel

Publisher: IEEE

Date: 20 June 2021

Copyright © 2021, IEEE

Thesis / Dissertation Reuse

The IEEE does not require individuals working on a thesis to obtain a formal reuse license, however, you may print out this statement to be used as a permission grant:

Requirements to be followed when using any portion (e.g., figure, graph, table, or textual material) of an IEEE copyrighted paper in a thesis:

- 1) In the case of textual material (e.g., using short quotes or referring to the work within these papers) users must give full credit to the original source (author, paper, publication) followed by the IEEE copyright line © 2011 IEEE.
- 2) In the case of illustrations or tabular material, we require that the copyright line © [Year of original publication] IEEE appear prominently with each reprinted figure and/or table.
- 3) If a substantial portion of the original paper is to be used, and if you are not the senior author, also obtain the senior author's approval.

Requirements to be followed when using an entire IEEE copyrighted paper in a thesis:

- 1) The following IEEE copyright/ credit notice should be placed prominently in the references: © [year of original publication] IEEE. Reprinted, with permission, from [author names, paper title, IEEE publication title, and month/year of publication]
- 2) Only the accepted version of an IEEE copyrighted paper can be used when posting the paper or your thesis online.
- 3) In placing the thesis on the author's university website, please display the following message in a prominent place on the website: In reference to IEEE copyrighted material which is used with permission in this thesis, the IEEE does not endorse any of [university/educational entity's name goes here]'s products or services. Internal or personal use of this material is permitted. If interested in reprinting/republishing IEEE copyrighted material for advertising or promotional purposes or for creating new collective works for resale or redistribution, please go to http://www.ieee.org/publications_standards/publications/rights/rights_link.html to learn how to obtain a License from RightsLink.

If applicable, University Microfilms and/or ProQuest Library, or the Archives of Canada may supply single copies of the dissertation.

[BACK](#)

[CLOSE WINDOW](#)

© 2022 Copyright - All Rights Reserved | Copyright Clearance Center, Inc. | [Privacy statement](#) | [Terms and Conditions](#)
 Comments? We would like to hear from you. E-mail us at customer@copyright.com

VITA

Deewakar Poudel

Department of Electrical and Computer Engineering

Old Dominion University

Norfolk, VA 23529

EDUCATION

Ph.D. in Electrical Engineering, Old Dominion University, Norfolk, VA, USA, 2022

M.Sc. in Physics, Tribhuvan University, Nepal, 2015

PROFESSIONAL EXPERIENCE

Graduate Teaching Assistant, Electrical and Computer Engineering, Old Dominion University, 2017 – 2022

Graduate Research Assistant, Electrical and Computer Engineering, Old Dominion University, 2017 – 2022

SELECTED PUBLICATIONS

- D. Poudel *et al.*, "Analysis of Post-Deposition Recrystallization Processing via Indium Bromide of Cu (In, Ga) Se₂ Thin Films," *Materials*, vol. 14, no. 13, p. 3596, 2021.
- D. Poudel *et al.*, "In Situ Recrystallization of Co-Evaporated Cu (In, Ga) Se₂ Thin Films by Copper Chloride Vapor Treatment towards Solar Cell Applications," *Energies*, vol. 14, no. 13, p. 3938, 2021.
- D. Poudel *et al.*, "Studying the Recrystallization of Cu (In, Ga) Se₂ Semiconductor Thin Films by Silver Bromide In-situ Treatment," in *2021 IEEE 48th Photovoltaic Specialists Conference (PVSC)*, 2021: IEEE, pp. 2307-2311